Picosecond Switching Measurements

Of A Josephson Tunnel Junction

By

Douglas R. Dykaar

Department Of Electrical Engineering

Advisor: T.Y. Hsiang

Ph.D. Thesis

Submitted in partial fulfillment

of the

requirements for the degree

DOCTOR OF PHILOSOPHY

May 1987

Table Of Contents

Curriculum Vitae

Douglas Raymond Dykaar was born on July 19, 1957 in New York City's Mount Sinai Hospital. At the time his parents resided in the Bronx, although this was mercifully exchanged for the borough of Queens after only two months and finally Nassau county.

He attended Brown University from 1975 until 1979 and received the Sc.B. degree in Engineering. In the fall of 1979 he entered the Ph.D. program in Electrical Engineering at the University of Rochester, receiving the M.S. degree in 1981.

During his first year of study, Mr. Dykaar was a Fellow of the Department of Electrical Engineering. Since that time he has been a Research Assistant at both the Department of Electrical Engineering and the Laboratory for Laser Energetics, as well as one year (1985) as an IBM Predoctoral Fellow.

Mr. Dykaar's research in Electrical Engineering was performed under the guidance of Professor Thomas Y. Hsiang.

Mr. Dykaar is a member of the IEEE, PCA and APS.

Acknowledgment

It is a great relief to be able to acknowledge the tremendous help and patience of my advisor Professor Thomas Y. Hsiang, as well as Professor Gerard A. Mourou. I am also indebted to Charles V. Stancampiano, who guided me through the treacherous and frightening transition from undergraduate to graduate student and finally to Graduate Student. In addition, some of the later work reported here was done with the help of Roman Sobolewski, whose ability to burn the midnight oil with complete abandon made possible the survival of many long experiments which were followed by the new day's dawn.

Any student who has worked at the Laboratory for Laser Energetics ("Laser Lab") has come to know the critical mass of intelligence represented by the other members of the ultrafast group. A special thanks goes to all those members of the ultrafast lane (both past and present) for their help and cooperation (despite my poor French language skills).

I am also thankful for the help I received from the Electrical Engineering department faculty and staff, as well as the financial support I received from the Department of Electrical Engineering, the Laboratory for Laser Energetics and IBM.

Finally, I am thankful that my parents made this possible, in that they made me possible to be where I now find myself.

Abstract

The advent of short pulse lasers has made possible the study of many new high-speed phenomena. This work is a study of superconducting Josephson tunnel junctions, which are excited by laser-generated current pulses.

These experiments make use of both pico- and subpicosecond lasers in conjunction with silicon, gallium arsenide and indium phosphide photoconductive switches. The combination of laser pulse and photoconductive switch is used to create current pulses with fast rise time, adjustable amplitude, and in some cases, adjustable width.

The current pulses are then used as excitations for Josephson tunnel junctions, recognized as being among the fastest devices known. Tunnel junctions were fabricated at the University of Rochester, as well as at the National Bureau of Standards in Boulder, Colorado.

To measure the time domain response of these devices directly, a cryogenic electro-optic sampler was implemented with an unprecedented time resolution. An electrical transient propagated on a transmission line, with a rise time of 360 fs - a record to this date - has been measured. In addition, a new detection scheme was implemented which allowed measurements approaching the shot-noise limit.

These advances in technology by the author were the key to being able to study the dynamics of Josephson junction behavior. Once this system was perfected, it was then possible to study the junction dynamics on a picosecond time scale.

The response of these junctions has been studied both directly in the time domain, and indirectly by studying the changes in the junction I-V curve caused by the high-speed excitation.

For the first time, measurements were made on a single Josephson junction which cannot be explained using a simple quasi-static model. That is, a summation of bias and applied pulse current did not yield the critical value. More surprising perhaps, than the discovery of an upper limit on junction performance, was the successful modeling of these measurements using the standard CRSJ model.

In addition, chaos has been directly observed in the I-V characteristics of these devices due to the periodic kicks that these current pulses represent. This is the first direct observation of chaos in a periodically kicked Josephson junction. As with the time domain study, this phenomenon was also simulated remarkably well using simple dynamical models to represent the junction. Insights into both the origins, as well as the fully developed chaotic behavior were gained from the simulations. These simulations matched the experimentally measured values of the switching threshold to a surprising degree.

The results of these experiments led the author to the development of the concept of a critical pulse charge, rather than a critical current, as the measure of the junction switching threshold. This concept is fundamentally different from the previous measure of the junction switching threshold. The concept was further refined by the author to include the concept of a critical rise time. For excitations of a given width and amplitude, those with a faster onset than this critical rise time, will result in chaotic behavior. These new concepts in junction characterization were the direct result of these experiments.

The techniques developed by the author for these studies have also been utilized in other experiments, such as signal propagation studies on superconducting and normal transmission lines, and characterization of other two terminal devices, such as the resonant tunneling diode and superconducting bridge.

1 Preamble

This thesis is as much a history of the development of ultrafast cryogenics as it is a study of superconducting phenomena. The organization reflects this theme: after some introductory and background chapters, the results are presented in essentially chronological order.

A brief historical outline is presented in Chap. 2, followed by Josephson junction theory in Chap. 3. This chapter not only presents the basic operating characteristics of Josephson junctions, but the junction analogs, which are critical to modeling these devices as well as the key to understanding their behavior.

Chapter 4 presents the first experimental results of a Josephson junction, driven by a laser-generated current pulse. These early results are modeled using a flux-flow theory presented at the end of the chapter.

Next, in Chap. 5, fast electro-optic sampling is summarized, including a description of the high-speed laser used, the detection electronics and the basic cryogenic techniques necessary for the experiments which follow.

These experiments are presented in Chap. 6. They include the design and construction of both the transmission line structures as well as the probes used in the experiments. Two sets of experimental results are presented: those in which the signal source remained outside the dewar at room temperature, and the fully integrated structure Finally, the results of the first observation of chaos in a periodically kicked rotator are presented.

In Chap. 7 simulations of the experimental results are presented. These include Junction simulations for both the transient case and I-V curves (chaos). The results of these studies are compared with the experimental results of Chap. 6.

Chapter 8 presents ongoing studies and includes some peripherally related work done by the author as well as ongoing experimental work and suggestions for future study. These include simulations of the signal propagation studies, as well as simulations of the transmission line impedance at energy gap frequencies. Also presented are experiments in infra-red electro-optic sampling and time domain studies of a novel transistor developed at MIT's Lincoln Laboratory, the Permeable Base Transistor.

This study concludes with an overall summary of the work and a final thought on the immediate future of the field.

2 Historical Notes: Superconducting Electronics to Fast Lasers

Although the liquefaction of helium was achieved in 1907, it was not until recently that the real potential of superconductivity has been realized [1],[2]. A somewhat narrow view of the event time line is shown in Fig. 2.1. The events are restricted to those which pertain to the development of the high-speed Josephson junction as it is known today, along with the development of the high speed characterization techniques which made time domain study of the Josephson junction possible.

Those high speed techniques are all based on the laser, which was not developed until the 1960s [3]. The first lasers were not high speed devices at all, being driven by flashlamps as they were. The truly high speed lasers were the dye lasers, developed in the 1970s at Bell Labs. These ring lasers had optical pulse widths on the order of 100 fs, and were among the fastest laboratory events. As a tool for research, however, they left much to be desired. This pulse was *optical* after all and the phenomena of interest were *electronic*.

The bridge between the electrical and optical domains was made in 1982, when an electro-optic Pockels cell was used to modulate a fast laser with a high speed electrical signal used as the modulation signal [4]. The first results obtained with the system were on the order of a few picoseconds (ps), but as better modulators were built, the system response dropped, and by 1984, the risetimes being measured were on the order of 500 femtoseconds (fs) [5]. Once this resolution was achieved, this technique was applied to such diverse problems as transistor characterization and superconducting physics [6]. The best electronic sampling oscilloscopes are limited to tens of picoseconds, even today.

1955

1957 ——— Author is born, BCS and Cooper Papers

1960 ——— Shapiro, Giaver Tunneling Papers

1962 ——— Josephson Paper

1965

1967 ——— IBM Josephson Project Begins

1970

1975 ——— Author Graduates High School

1979 ——— Author Matriculates at Rochester
1980 ——— Ring Laser, Superconducting Sampler Constructed

1982 ——— Electro-optic Sampler Constructed
1983 ——— IBM Josephson Project Ends

1985 ——— Author Constructs First Electro-optic Cryo-sampler
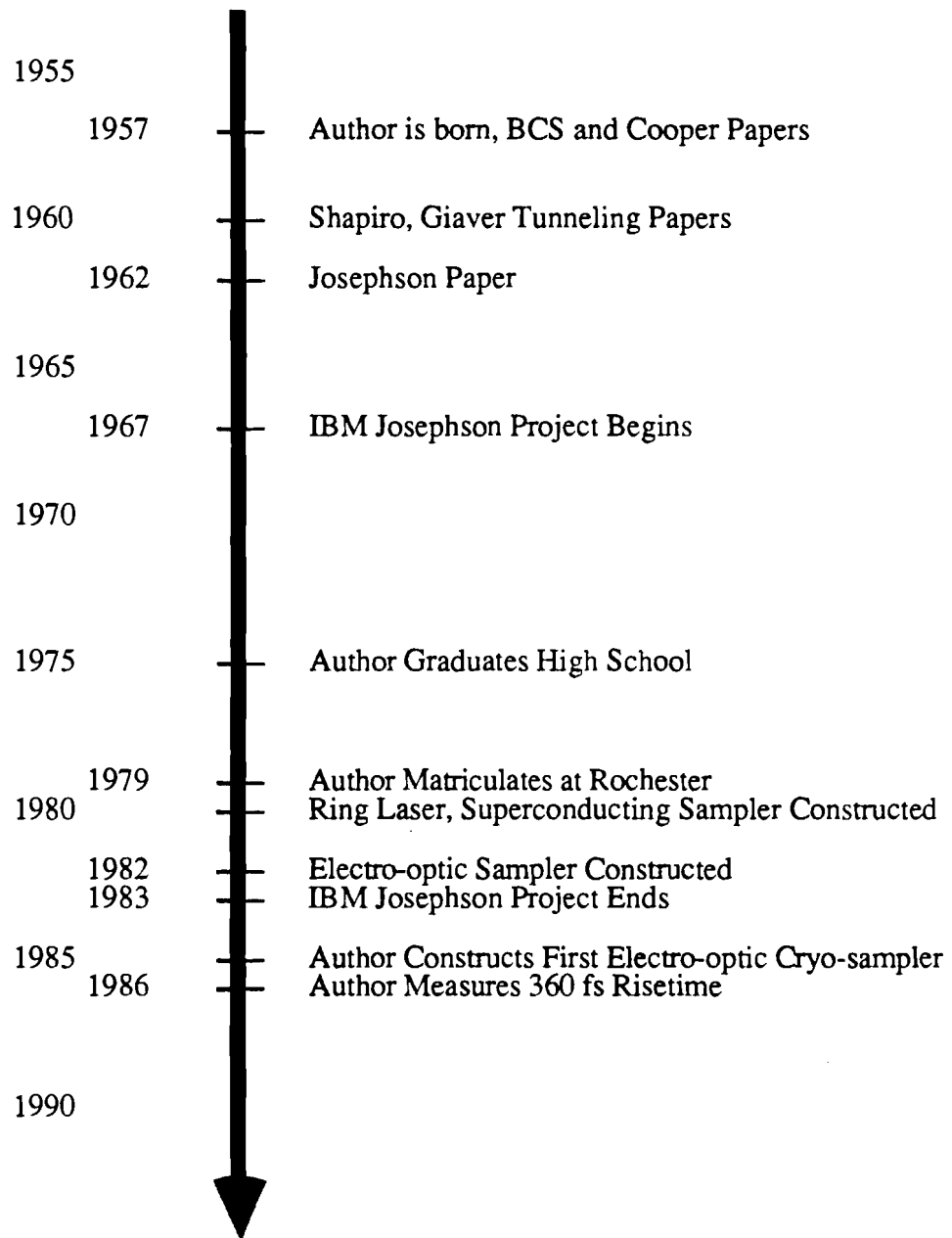1986 ——— Author Measures 360 fs Risetime

1990

Figure 2.1 Event time line

Given the steady advances being made in the optical domain, it is unlikely that speeds in the electronic domain will catch up in the near future. Although great strides are being made in new electronic devices, the fastest optical pulse is now only 8 fs [7].

Given the huge advantage in speed in the optical domain, it appears likely that research in ultrafast phenomena will continue to require the use of the optical domain for the foreseeable future.

This chapter first presents a short introduction to tunneling theory, which is necessary to understand the behavior of tunnel junctions. Next, a brief "tour" of the Josephson junction is given. Finally, two useful analogs for Josephson junctions are presented: the pendulum and washboard. In thinking about junction responses for various excitations, these models are extremely useful and will be referred to frequently.

3A Tunneling Theory [8]

In classical physics, if a particle with some energy, E, approaches a potential barrier of "height" V_0, then the particle is reflected for $E < V_0$, and transmitted for $E > V_0$. However, in quantum physics, the same particle with $E < V_0$, has a finite probability of existing on the far side of the barrier.

Now consider a barrier which is a small gap between two metals. Here, the particle is an electron, particle energy is imparted via an applied voltage, and transmitted electrons constitute a current. Fig. 3A.1 shows a tunneling diagram for the Normal metal - Insulator - Normal metal (NIN) case at T = 0. In the case of electrons, we also require for tunneling that the electron tunnels to an unoccupied state. As shown in the figure, only electrons in metal 1, which are above the occupied states in 1etal 2, are available for tunneling.

By using Fermi's Golden Rule [9], one can express the current through the 1er as:

$$\cdot \frac{2\pi}{\hbar} |M|^2 \int_{-\infty}^{\infty} N_1(E) N_2(E + eV) \left[f(E) - f(E + eV) \right] dE \qquad (3A.1)$$
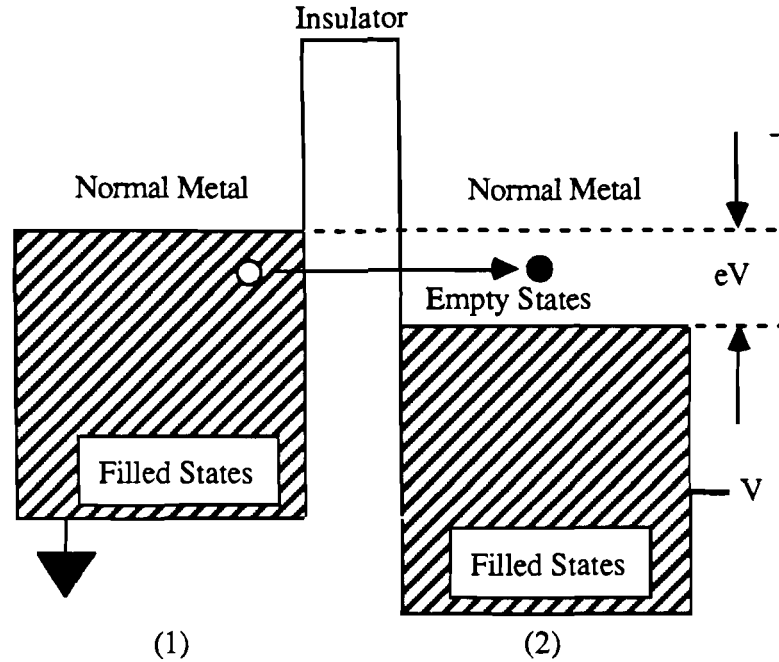
Figure 3A.1 Normal-Insulator-Normal (NIN) Tunneling Schematic (T = 0).

where $|M|^2$ is the tunneling matrix element, i.e. the probability of a particular

tunneling event taking place, $N_i(E)$ is the density of states at zero temperature

(constant), and so the integrand is the difference in the distributions of occupation. For

the Fermi distributions at zero temperature, this is just equal to one divided by the

applied voltage, eV. In that case Eq. (3A.1) becomes:

$$I_{nn} = \frac{2\pi}{\hbar} |M|^2 N_1(0) N_2(0) eV = G_{nn} V \tag{3A.2}$$

This is just Ohm's law. The term $|M|^2$ was shown by Harrison [10] to depend

exponentially on the barrier thickness, as is expected from quantum tunneling theory.

Next, let us return to Eq. (3A.1), but now consider the case of two

superconductors separated by a barrier (SIS). For a superconductor, as shown by

BCS [11], the density of states can be represented as in Fig. 3A.2, i.e.

$$N_s(E) \approx N_n(0) \frac{E}{\sqrt{E^2 - \Delta^2}} \qquad (3A.3)$$

where $N_n(0)$ is the density of states for a normal metal at zero temperature, and

Δ is the energy gap parameter. The gap, Δ , is material dependent, and represents half

of the energy (see Fig. 3A.2) required to break a pair. Using this , one can construct a

tunneling diagram as in Fig. 3A.1 for the SIS case. For generality, consider the case

of two different superconductors, S_1 and S_2 , so that $\Delta_1 \neq \Delta_2$. As shown in Fig.

3A.3a, for no applied voltage there can be no tunneling, since there are no unoccupied

states available to tunnel to. When the applied voltage reaches a value of $\Delta_1 - \Delta_2$ as

shown in Fig. 3A.3b there will be a sharp increase in the current as shown in Fig.

3A.4. This is due to the thermally excited states in S_1 having an asymptotically large

number of states to tunnel to. However, as the applied voltage increases, the thermally

excited states in S_1 will have fewer and fewer available states, which results in the

decrease in the current shown in Fig. 3A.4.

When the applied voltage reaches $\Delta_1 + \Delta_2$, the occupied sub-gap states will be

able to tunnel as shown in Fig. 3A.3c, and the current will again rise sharply as

shown in Fig. 3A.4.

Finally, consider the tunneling current in the low temperature and low voltage

regime. Here the Fermi distribution of Eq. 3A.1 can be simplified:
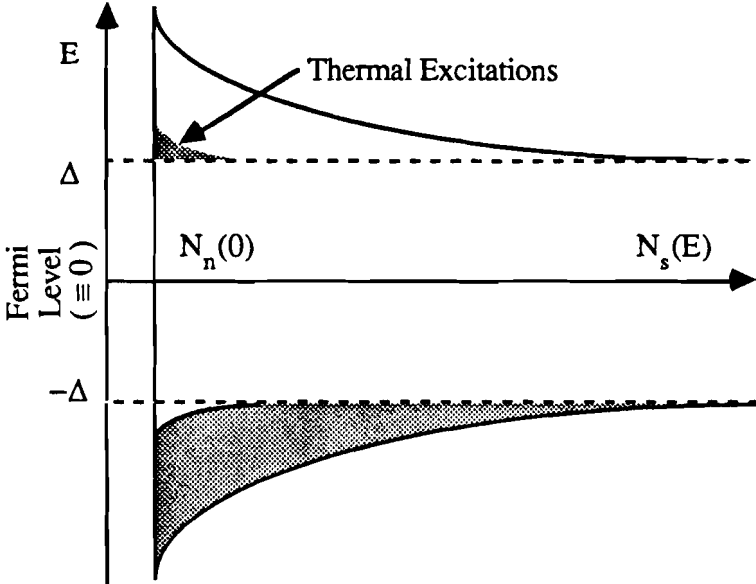
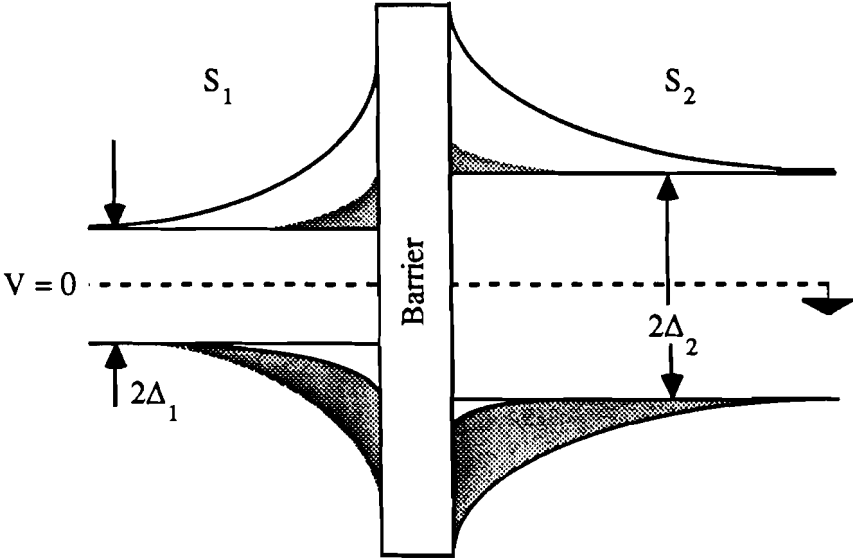Figure 3A.2 Superconducting density of states.

Figure 3A.3a Superconductor-Insulator-Superconductor (SIS) Tunneling Schematic.
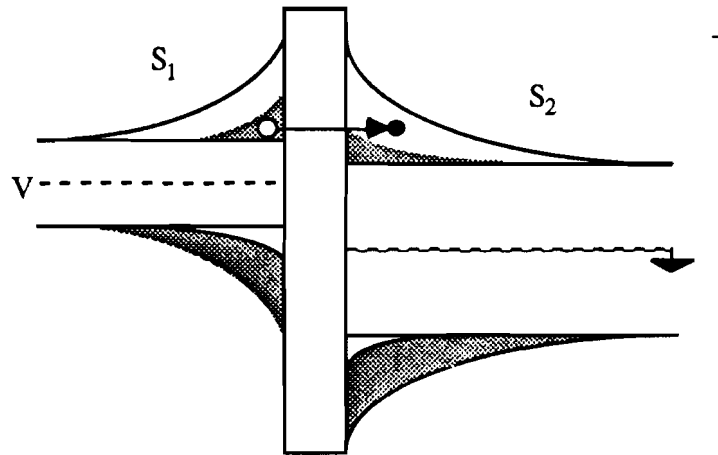
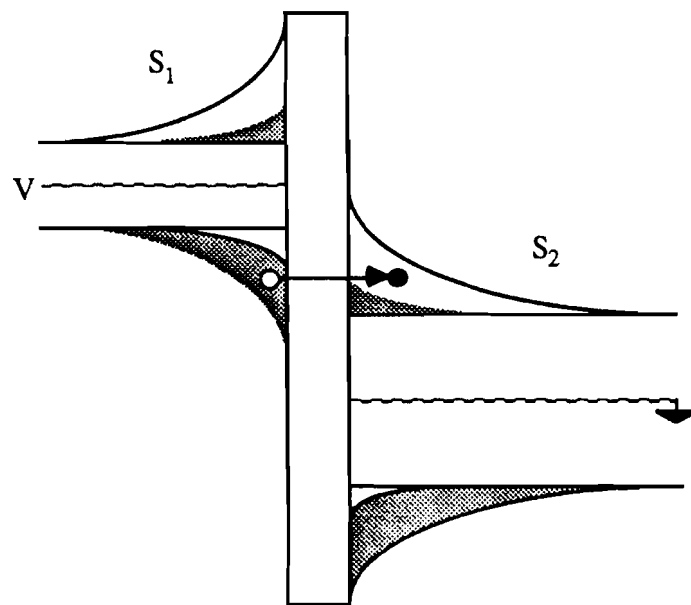Figure 3A.3b SIS Tunneling Schematic continued.

Figure 3A.3c SIS Tunneling Schematic continued.

$$f(E) = \left\{ 1 + \exp\left[\frac{E}{kT}\right] \right\}^{-1} \tag{3A.4}$$

for $E = eV < \Delta$ and $eV \gg kT$, then $f(E) \approx \exp\left[\frac{-E}{kT}\right]$ $\tag{3A.5}$
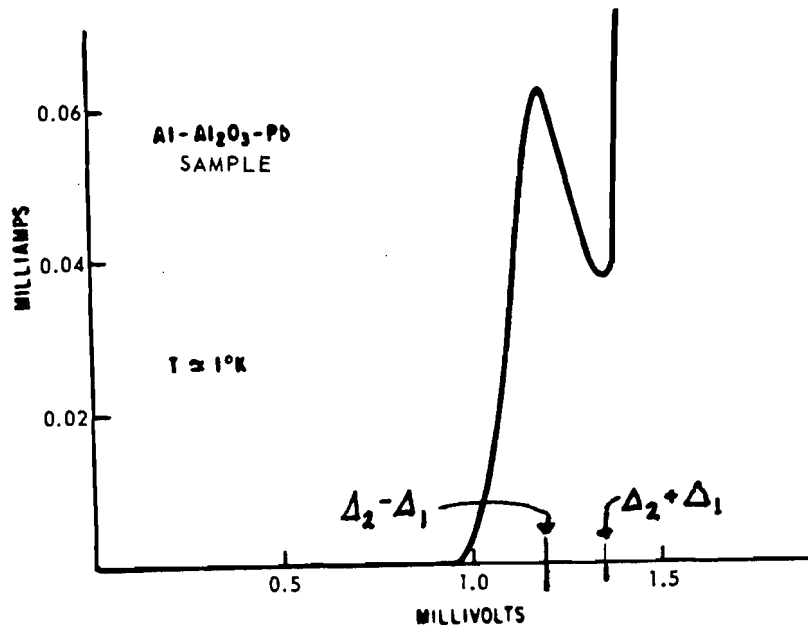
Figure 3A.4 Tunneling I-V characteristic, after Giaever [12].

Substituting Eq. (3A.5) in to Eq. (3A.1) one obtains:

$$I \approx \frac{2\pi}{\hbar} \left|M\right|^2 \int_{-\infty}^{\infty} N_1(E)\, N_2(E + eV) \exp\left[\frac{-E}{kT}\right] \left\{ 1 - \exp\left[\frac{eV}{kT}\right] \right\} dE \tag{3A.6}$$

The last term in the integral can be taken outside, since it has no E dependence, and so:

$$I \propto \exp\left[\frac{eV}{kT}\right] \tag{3A.7}$$

for $\Delta > eV \gg kT$. This can be used as a measure of junction quality.

3B Tunnel Junction Theory

The basic element of superconducting electronics is the Josephson junction. While there are several types currently capable of being fabricated, it is the tunnel junction which is usually chosen for digital applications because of the similarity between the fabrication of conventional semiconductor, and Josephson tunnel junction circuitry [13].

A Josephson tunnel junction can be made by evaporating a stripe of metal onto an insulating substrate, oxidizing it, and then evaporating another layer of metal across the first. Two possible geometries are shown in Fig. 3B.1.

(a) "Z" Stripe Junction   (b) In Line Junction
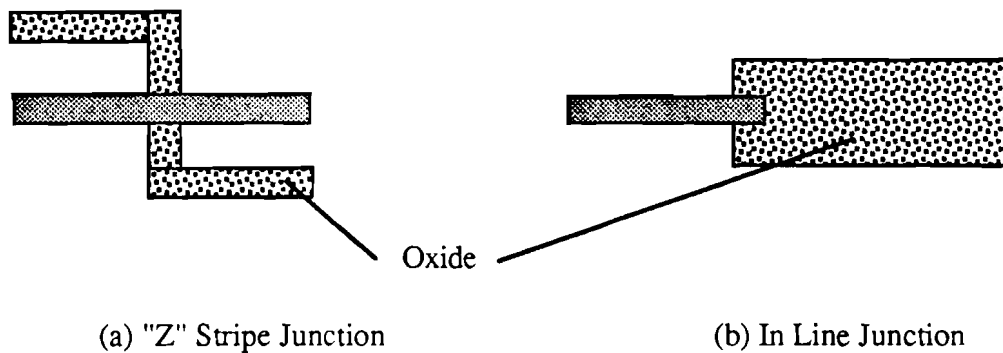
Figure 3B.1 Tunnel Junction Geometries

If the metals can be made superconducting and the oxide is thin enough (nanometers), and without holes, then the junction will (below the superconducting transition temperature and without applied magnetic field) exhibit a dc current-voltage characteristic as shown in Fig. 3B.2.

The curve can be divided into two distinct regimes: zero- and finite voltage. In the zero voltage regime the current is carried solely by electron pair tunneling which is described by the Josephson relations:

$$I = I_c \sin\phi \qquad \text{(3B.1a)}$$

$$\dot{\phi} = \frac{2e}{\hbar} V \qquad \text{(3B.1b)}$$

where ϕ is the wave function phase difference between the two superconductors, I_c is

the maximum zero voltage current (or critical current), and e and $\hbar$ are the usual

physical constants.

In the finite voltage regime the Josephson relations are still valid, but in addition
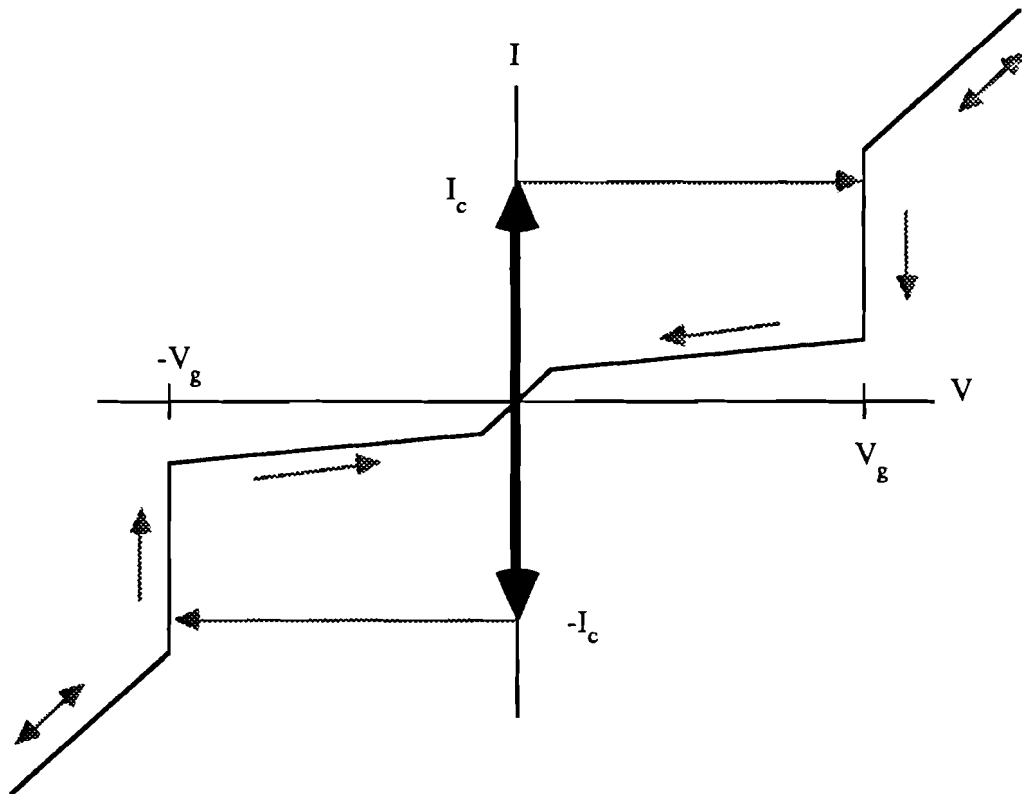

Figure 3B.2 Hysteretic tunnel junction I-V characteristic

the junction exhibits quantum-mechanical tunneling. This is manifested by a very high

resistance for values of voltage less than the energy gap voltage, V_g. The resulting

current due to this quasiparticle tunneling can be calculated.

In order for the junction of Fig. 3B.2 to function as a latch, it must be

current-biased at some current $I_b < I_c$. Then if the current is pulsed to a value $I_p > I_c$,

the junction will generally switch to the finite voltage state. Due to the hysteretic nature

of the junction , the voltage will persist even after the current pulse decays. Resetting

the latch requires reduction of the total current to zero.

An alternative method for switching a tunnel junction is the control line

technique shown in Fig. 3B.3. In this arrangement , a current-carrying control line

passes in the vicinity of a junction. The control current, I_{con}, induces a magnetic field

in the junction, B^0, which is related to the phase difference, ϕ, across the junction by :

$$\nabla\phi = \frac{2ed'}{\hbar} (\hat{n} \times B^0)$$ (3B.2)

where $\hat{n}$ is the unit normal directed from one electrode to the other and d' is the

effective oxide thickness.

For a rectangular junction with uniform current density, the dependence of the
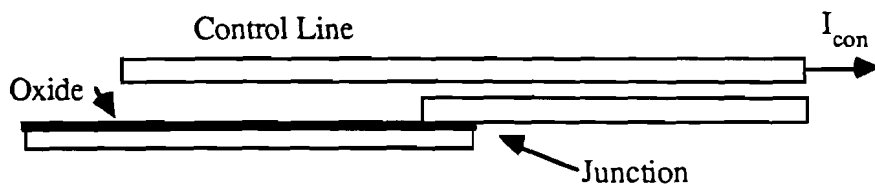

Figure 3B.3 Control line geometry

critical current, I_c, on the induced flux, Φ, in the junction is:

$$I_c(\Phi) = I_c(0) \, \text{sinc}(\pi\Phi/\Phi_0) \qquad\qquad (3B.3)$$

where $\Phi_0 = \pi\hbar/e = 2.07 \times 10^{-15}$ Wb is the flux quantum. This dependence is shown in Fig. 3B.4.
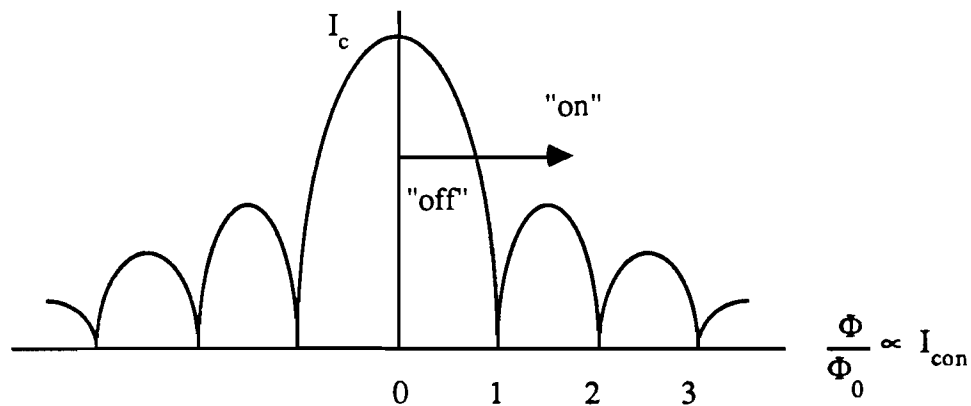
Figure 3B.4 Dependence of maximum zero-voltage current as function of applied flux.

In practice, this means that if a junction is biased at some current, I_b, less than the critical current , I_c, in the zero voltage state, then the application of a control current can reduce the critical current such that I_b is now greater than $I_c(\Phi)$. This results in the junction switching and latching in the finite voltage state. the switching path is shown by the arrow in Fig. 3B.4. Here too, resetting of the junction is accomplished by making the bias current zero. This method offers high fanout capability, and has been used extensively in digital applications. However, the inductance associated with the magnetic coupling limits the ultimate switching speed.

In addition to applied magnetic fields, RF fields can be applied to a junction as shown schematically in Fig. 3B.5. Here the junction is modeled as an ideal junction

Figure 3B.5 Equivalent circuit for applied rf.

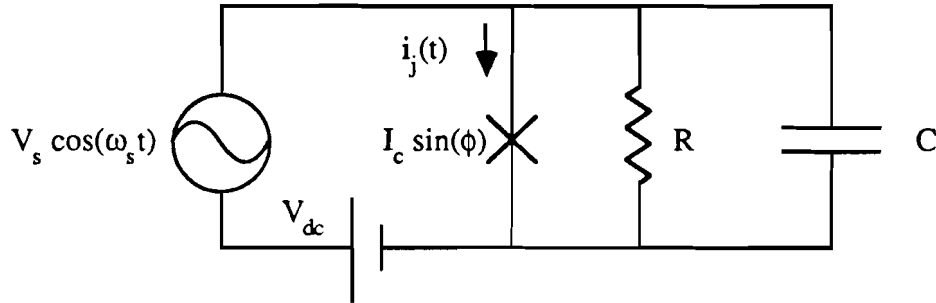obeying Eqs. (3B.1a) and (3B.1b), plus a shunt resistance, R, and capacitance, C. For this circuit , the junction current, $i_j(t)$ can be expressed as :

$$i_j(t) = I_c \sum_{n=-\infty}^{\infty} (-1)^n J_n \left[\frac{2eV_s}{\hbar \omega_s} \right] \sin \left[(\omega_j - n\omega_s)t + \phi_0 \right]$$

(3B.4)

where $\omega_j = \dfrac{2eV_{dc}}{\hbar}$ and ϕ_0 is a constant.   (3B.5)

Equation (3B.5) is called the Josephson frequency - voltage relation and the quantity $\dfrac{2e}{\hbar}$ is approximately 484 MHz/μV. When $\omega_j = n\omega_s$ or $V_{dc} = \dfrac{n\hbar\omega_s}{2e}$ there will be current spikes in the junction dc I-V curve given by the dc part of Eq. (3B.4). However, since real junctions are current biased (due to experimental constraints), the curve actually shows a step like structure along the voltage direction. The appearance of these Shapiro steps [14] under RF excitation and the modulation of I_c by an applied magnetic field are clear indications of the presence of the Josephson effects.

3C Circuit and Pendulum Models

The standard CRSJ (Capacitively and Resistively Shunted Junction) equivalent circuit for a real Josephson junction driven by a constant current, I, is shown in Fig. 3.C.1.
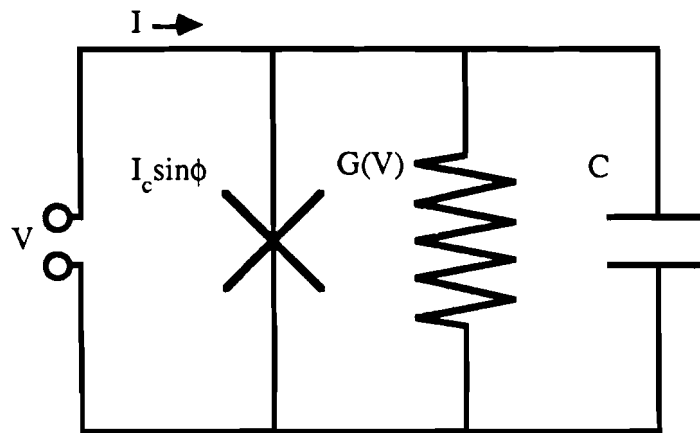
Figure 3C.1 Equivalent circuit for a real Josephson junction

In addition to an ideal element described by the Josephson relations (Eqs. 3.1a and 3.1b), the circuit includes a junction capacitance, C, and a voltage dependent conductance, G(V). The equation describing this circuit is the Stewart-McCumber relation [15], [16]:

$$I = I_c \sin\phi + VG(V) + C\dot{V} \qquad (3C.1)$$

By substituting Eq. (3B.1b) into (3C.1) and taking G(V) as constant, the voltage dependence can be eliminated:

$$I = \frac{\hbar C}{2e}\ddot{\phi} + \frac{\hbar G}{2e}\dot{\phi} + I_c \sin\phi \qquad (3C.2)$$

Compare this equation to that of a pendulum of mass m, swinging on a massless

rod of length l, moving in a medium with damping c:

$$T = M\ddot{\phi} + c\dot{\phi} + mgl \sin\phi \qquad (3C.3)$$

as shown in Fig. 3C.2. The total applied torque is T, and M is the moment of inertia of

the pendulum. A comparison of Eqs. (3C.2) and (3C.3) is given in table 3C.1. This

analog is useful for predicting junction behavior in many situations.
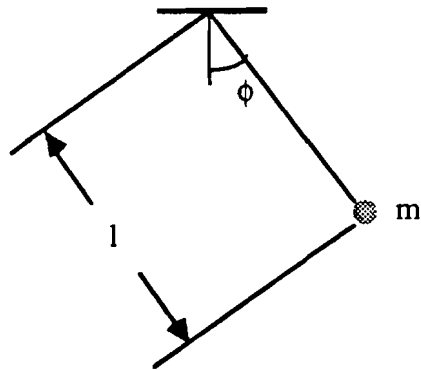
Figure 3C.2 Pendulum analog

Table 3C.1

Electrical: Eq. (3C.2)	Mechanical Analog: Eq. (3C.3)
Phase Difference ϕ	Angle ϕ
Voltage ($\propto \dot{\phi}$)	Angular velocity $\dot{\phi}$
Capacitance C	Moment of Inertia M
Conductance G	Damping c
Critical Current I_c	Maximum Torque For No Rotation
Source Current I	Applied Torque T
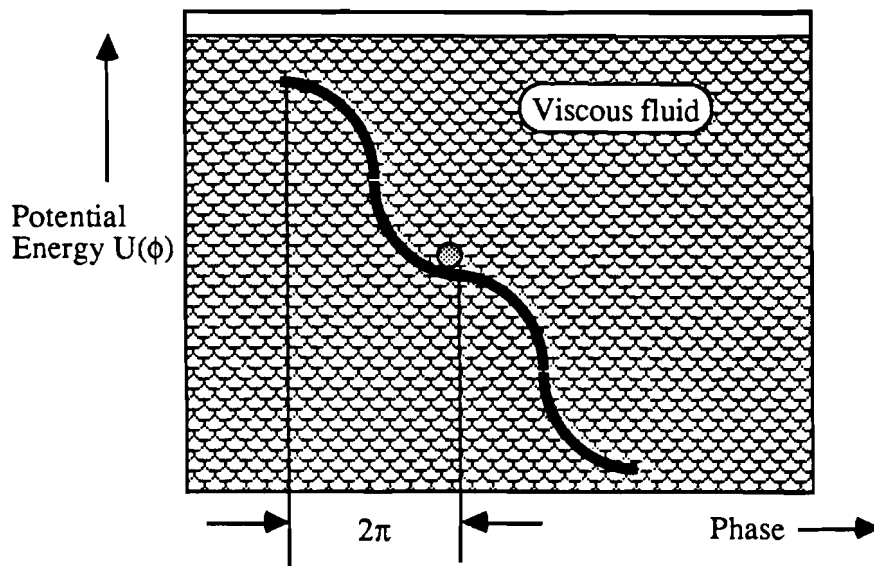
Figure 3C.3 Washboard analog

Another useful concept is the washboard analog. Here, as shown in Fig. 3C.3, the junction is modeled as a ball of mass m, sitting in a "washboard" potential, which is immersed in a viscous liquid. The comparison of this version of Eq. (3C.3) to Eq. (3C.2) is given in Table 3C.2. Since the axes in Fig. 3C.3 are energy and phase, this model is useful in considering current-phase relationships.

Table 3C.2

Electrical	Washboard Analog [17]
Capacitance C	Mass
time constant 1/(RC)	Viscosity
$-I\phi + I_c - I_c \cos\phi$	Potential energy
CV	Momentum

Finally, it is possible to reformulate Eq. (3C.2) to make it more tractable for numerical methods:

$$\frac{I}{I_c} = \beta_c \frac{d^2\phi}{d\theta^2} + \frac{d\phi}{d\theta} + \sin\phi \qquad (3C.4)$$

where $\theta \equiv \left[\frac{2e}{\hbar}\right]\left[\frac{I_c}{G}\right] t \equiv$ normalized time and $\beta_c \equiv \left[\frac{2e}{\hbar}\right]\left[\frac{I_c C}{G^2}\right]$.

Here the Stewart-McCumber parameter, β_c , indicates the amount of hysteresis

in the junction , as shown in Fig. 3C.4. When $\beta_c = 0$, no hysteresis appears, but for

$\beta_c \gg 1$, a large hysteretic region results.

It should be noted that all of the above analogies were formulated for a constant
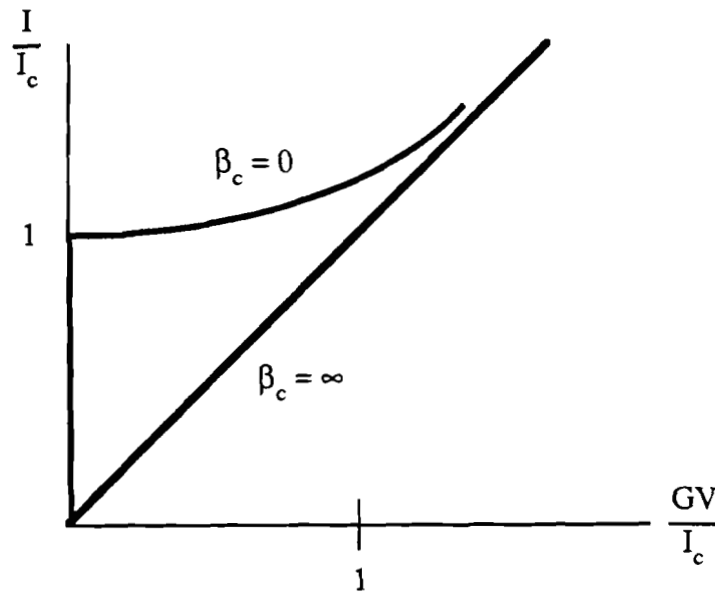

Figure 3C.4 Normalized I-V characteristic.

conductance. Real tunnel junctions exhibit the energy gap structure shown in Fig. 3B.2. However, for most purposes these models suffice for demonstrating general dc behavior and functional relationships.

4A Purpose

The first set of experiments used a laser-driven photoconductive switch to excite a Josephson tunnel junction. The laser available at the time was a low repetition rate, relatively long-pulse system. However, since this was the first attempt to characterize a junction using this technique, the experiment was designed to be as simple as possible: large area tunnel junctions were used to insure that the junction response time would be slow relative to the response of the system and the use of lead junctions allowed junctions to be fabricated in house.

Due to the low repetition rate of the laser, the experiment was necessarily a single shot one. However, by utilizing the hysteretic nature of the tunnel junction, a successful switching event resulted in the latching of the junction into the voltage state. The junction could then be reset by grounding the biasing supply between laser shots. By adjusting the dc bias, the pulse width and the pulse height, the switching threshold was mapped out.

This ability to set the bias, I_b, for each shot was an advantage of the single shot system, as previously published simulations such as Ref. [17] had used current biased junctions driven by a small overdrive.

The intent of these early experiments was to show the feasibility of using laser-generated electrical pulses to measure the response of a Josephson junction.

The first section describes the fabrication and testing technique used to make samples for these experiments. Next, the method of making short electrical pulses from short optical pulses is presented. Section 4C(ii) presents details of the signal measurement technique. The results of these experiments are described in section 4C(iii). Finally, the results are modeled using a theory based on flux flow, and in the last section the limits of this theory are discussed.

4B Lead Junction Fabrication

Many superconducting metals have been used to construct tunnel junctions. Since tin is easy to work with, it has been used in the past (both at University of Rochester and elsewhere), for fabricating tunnel junctions [18],[19]. However, the transition (or critical) temperature of tin, i.e. the temperature at which it becomes superconducting, is 3.7 K, which is less than the boiling point of liquid helium (4.2 K at atmospheric pressure). To the experimenter, this means that the liquid helium must be transferred from the storage dewar into an experimental dewar, which is then pumped on with a vacuum pump. The process of transferring and pumping on liquid helium is wasteful of both time and helium.

At the beginning of these experiments it was decided that it would be useful to develop an alternative to the tin junction, which had not been fabricated at the university for some time. Lead was chosen since its transition temperature of 7.2 K is greater than the boiling temperature of liquid helium at atmospheric pressure. This meant that a lead junction could be tested by merely placing it in the storage dewar and observing its dc I-V characteristic. Unfortunately, developing a usable, high-quality junction proved to be a difficult proposition. While lead junctions are easily fabricated and have been used by others in the past, lead has other properties which make sandwich-type junctions with thermally grown oxides especially susceptible to mechanical failure. Specifically, as the lead films are grown on an insulating substrate, there are large differences in the coefficients of thermal expansion. When the junction is heated, cooled, or for that matter just left lying around for a few hours, the metal film becomes stressed and distorts.

One mechanism which can relieve this stress is shown in Fig. 4.B1. As shown, "hillocks" have grown on the surface and unfortunately, through the thin oxide layer

which forms the junction. In addition to hillocks, tiny whiskers can form, growing

perpendicularly from the metal surface. These too, are capable of puncturing the oxide
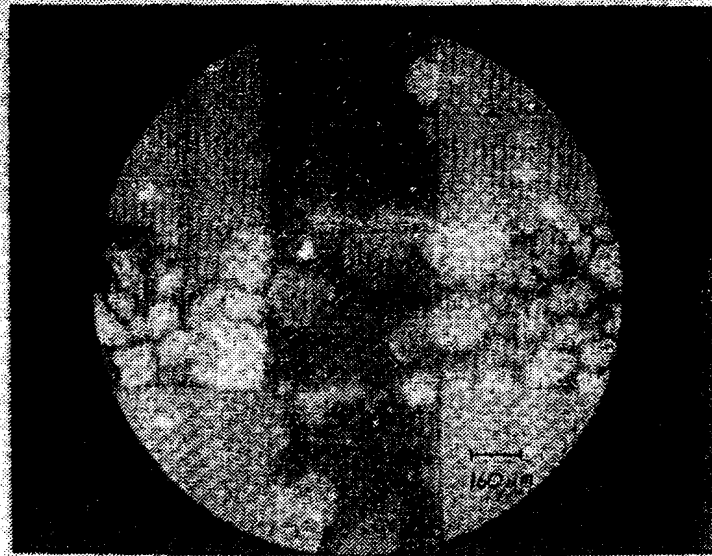
Figure 4.B1 Microscope picture of a used cross type tunnel junction. Hillocks appear

as white spots due to side illumination. Blotches result from condensation.

layer and while they were not observed in these experiments, they have been seen by

other groups [20].

Once the oxide is punctured, the junction will behave as if shorted by a small

superconducting link. A junction shorted in this way may still exhibit a finite

zero-voltage current, but not due to the Josephson effect. Figure 4.B2 shows an I-V

curve for a lead junction, which was probably shorted by one of the above

mechanisms.

In order to test whether a junction was good or not, the simple arrangement of

Fig. 4.B3 was used to display the dc I-V curve of the junction. From the I-V curve it is possible to gauge the quality of the junction.

Lead junctions were fabricated on 0.250 x 0.500 x 0.010 in. sapphire substrates.
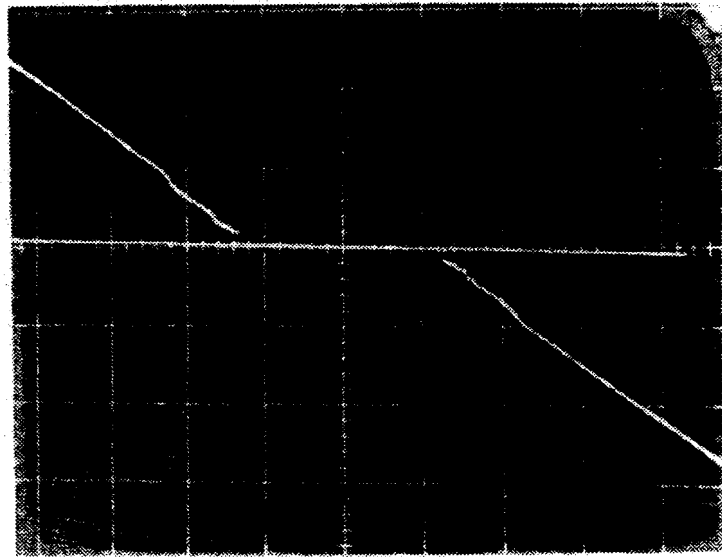
Figure 4B.2 I-V characteristic of a shorted junction (oxide punctured). Scales are 20mV/div vertically, and 5mA/div horizontally.

Metal deposition took place in a CVC vacuum system capable of pumping down to ~4 x 10^{-6} torr.

The fabrication process began with cleaning the substrates, which were then placed into the vacuum system. As shown schematically in Fig. 4.B4, the substrates were held upside down using vacuum grease. The metal to be evaporated was placed in "boats", which are strips of sheet metal with circular depressions. After pumping
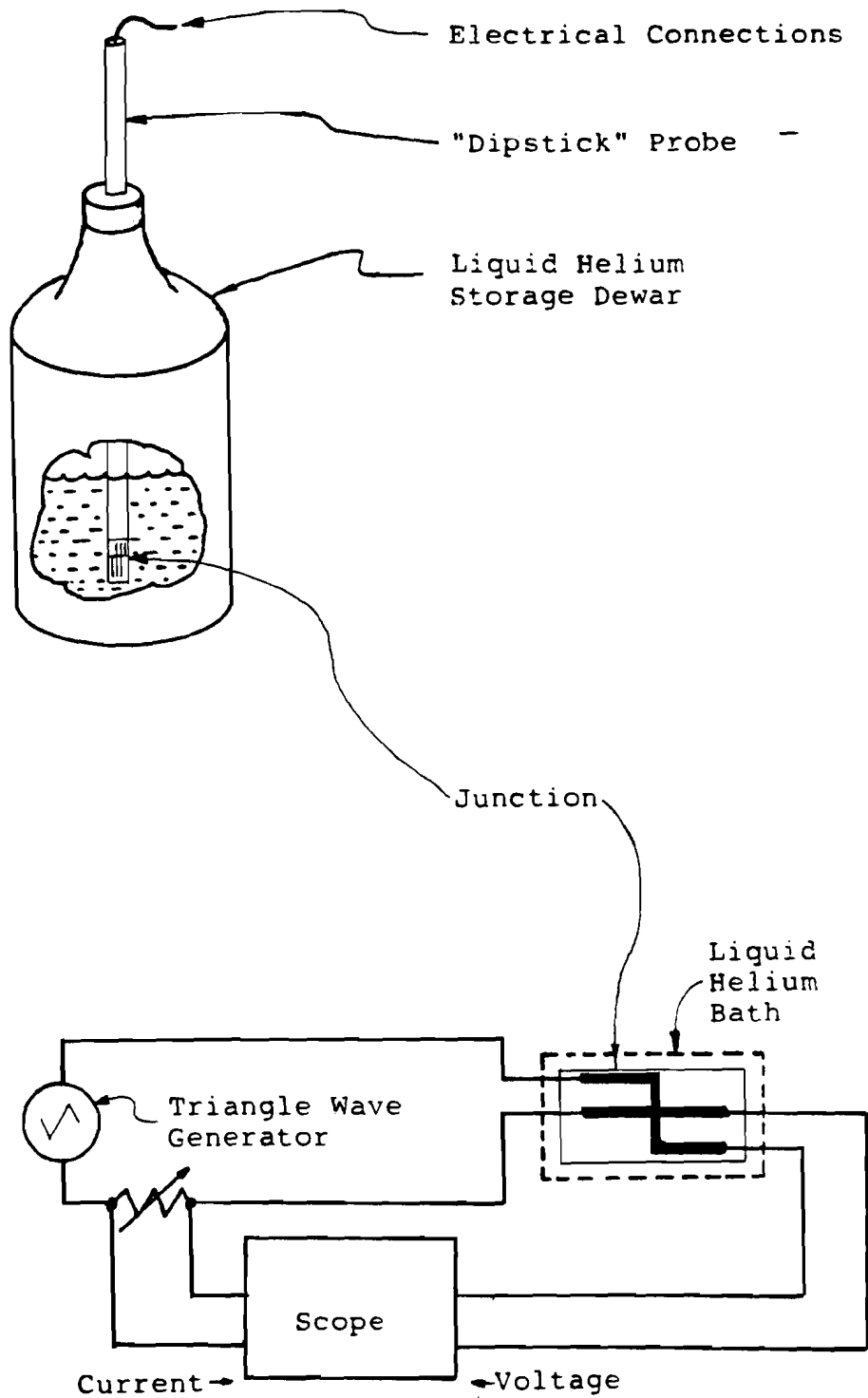
Figure 4B.3 Test set-up
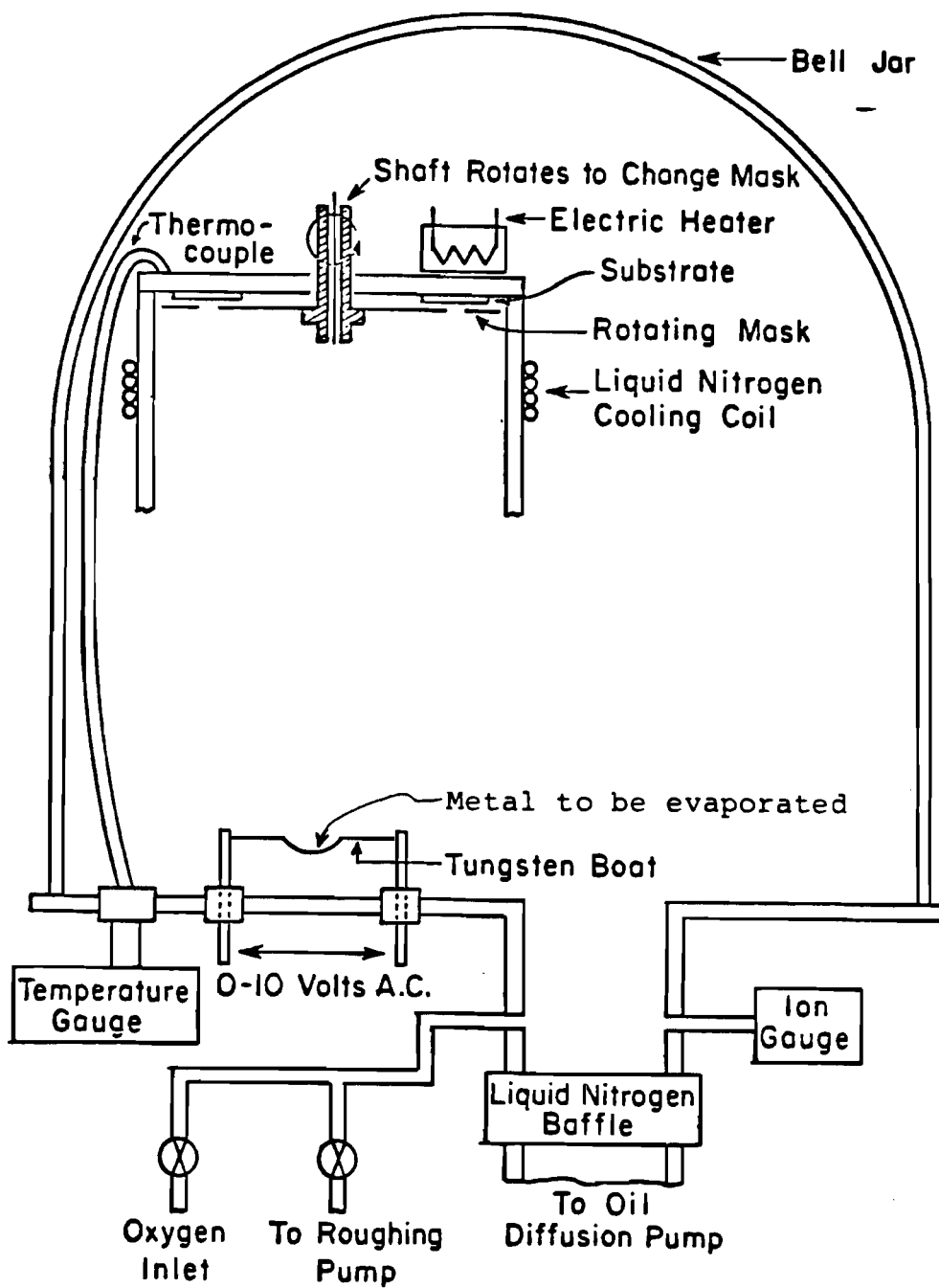
Figure 4B.4 Vacuum system schematic.

down to the correct pressure, the metal was evaporated by passing a large current through the boat. The correct pattern was formed by positioning a stainless steel shadow mask in the proper location. A sector of a typical mask is shown in Fig. 4.B5. In the order in which they were used, the patterns are, (3) parallel stripe contact pads, (2) parallel stripes, (1) oxidation window, (4) "Z" stripe, (5) "Z" contact pads.

After the parallel stripes were evaporated onto the substrate, the entire metal surface was oxidized. First the stage was electrically heated to 65° C. Then the pressure in the bell jar was raised to atmospheric. This was followed by blowing a small jet of oxygen onto the substrates. Since small traces of water vapor may increase the rate of oxide growth [21], the oxygen which was "dry" from the tank, was allowed to pass across the surface of de-ionized water before impinging onto the substrates. After approximately thirty minutes, the heat and oxygen were turned off and the bell jar was pumped out. During evacuation the stage was cooled to room temperature.

Finally the "Z" stripe was evaporated, followed by the "Z" stripe contact pads. After removal from the vacuum system, small wires are attached to the contact pads by sandwiching the wire between "blobs" of indium. This is shown in Fig. 4.B6.

Once the junction had been fabricated, it was a relatively simple task to obtain a dc I-V curve. However, because testing was restricted to the storage dewar, it was not possible to employ the standard test for the presence of the Josephson effect, namely applied magnetic- and RF fields.

In lieu of these tests, there are several calculations that can be made to gauge the quality of a given junction.

First, it can be shown (Sec. 3A) that for voltages, $V \ll V_g$ and for $T \ll T_c$, the quasiparticle current is exponentially related to the voltage:

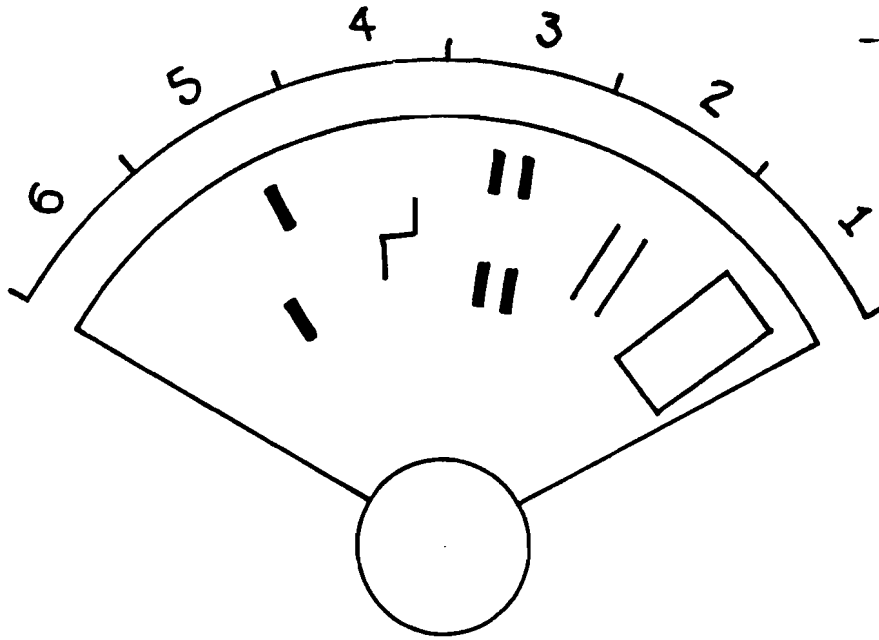$$I \propto \exp[\frac{eV}{kT}] \tag{4.1}$$

Figure 4B.5 Section of shadow mask (enlarged).
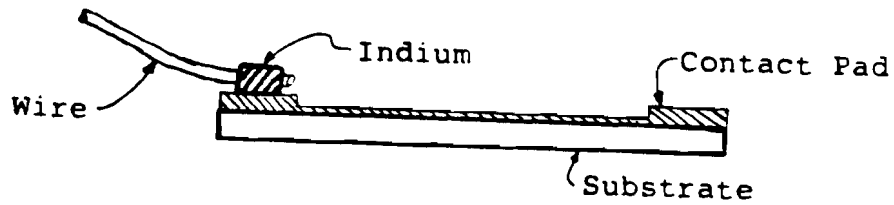
Figure 4B.6 Wire attachment method.

This relation is especially useful for lead junctions, because of their tendency to form shorts. By plotting voltage versus log current for $V \ll V_g$ one can determine the linearity of equation 4.1. Also, if the plot is nonlinear, one can determine the value of the resistance shunting the junction by fitting an equation such as Eq. (4.1), but with an additional resistive term. This procedure, then, gives an indication of the junction quality.

Another important parameter useful in characterizing the quality of a junction is the critical current density. For junctions where the magnetic field induced by the currents in the junction is negligible, the critical current density, J_c , is just the critical current, I_c , divided by the junction area.

After finding the critical current density, one can find the Josephson penetration depth, λ_j , from:

$$\lambda_j^2 = \frac{\hbar}{2eJ_c\mu_0(2\lambda + d)}$$ (4.2)

where $(2\lambda + d)$ is the effective oxide thickness. If the Josephson penetration depth is much greater than the junction dimensions, then the assumption made in calculating the critical current density, namely, that the magnetic field induced by currents in the junction is negligible, is justified. If however, the Josephson penetration depth is significantly less than the junction dimensions, then the critical current density must be recalculated using:

$$J_c = \frac{I_c}{P\lambda_j}$$ (4.3)

where P is the junction perimeter. The new value of critical current density must then be justified against the value used in Eq. (4.2).

Another insight into large junction behavior can be seen by considering the Displaced Linear Slope (DLS) effect [22] shown in Fig. 4B.7. The behavior can be
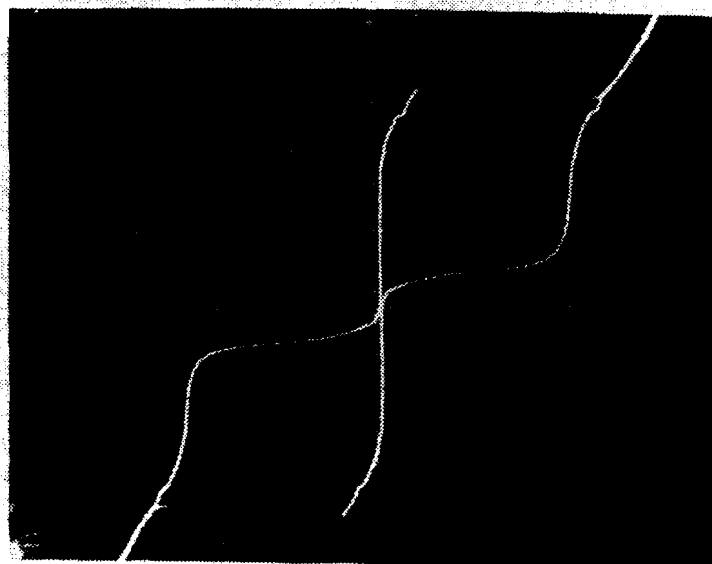
Figure 4B.7a I-V Curve for large area Pb-PbO$_x$-Pb junction showing DLS effect. Scales are 0.5 mA/div vertically and 1mV/div horizontally.

Figure 4B.7b I-V Curve for large area Pb/In/Au alloy junction showing DLS effect. Scales are 5 μA/div vertically and 1mV/div horizontally.

qualitatively explained by considering the flow of fluxons [8] which interact with a current flowing in the same direction in the junction. For the one dimensional case, current entering from one end of the junction forces fluxons towards the center, and current entering from the other end forces antifluxons towards the center, where they annihilate each other and form a "breather" region. The DLS effect arises from the dissipative effect associated with the flow of the fluxons. This flux flow behavior in large junctions will be discussed again in Sec. 4D.

4C(i) Pulse Generation

High speed electrical pulses, with rise times from picoseconds to femtoseconds, can be generated using a semiconductor switch [23]. A typical layout of such a switch is shown schematically in Fig. 4C.1. Switches have been fabricated in both microstrip- and coplanar transmission line geometries. Basically the switch consists of a broken transmission line fabricated on a semiconductor substrate.
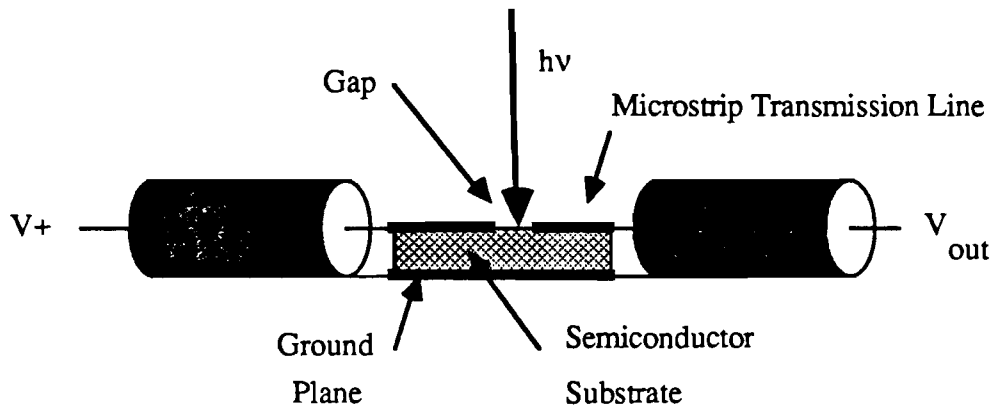
Figure 4C.1a Microstrip transmission line switch geometry (side view)
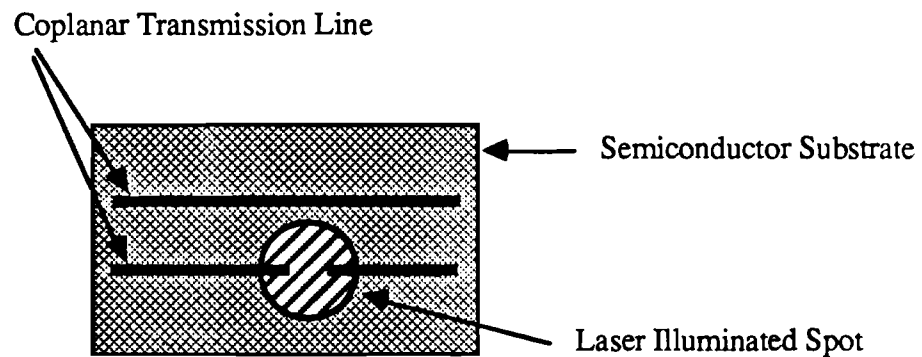
Figure 4C.1b Coplanar transmission line switch geometry (top view)

The operation of the switch is as follows. One side of the switch is connected to a voltage, V+. The transmission line between the source and the switch acts as a charge line, and with the high resistance of the switch gap there is essentially no output. The maximum (safe) field across the gap is generally a function of the electrode uniformity, and at room temperature is usually about a volt per micron of gap length. For soft materials like gold or indium, the switch failure mode is thought to be whisker formation across the gap caused by local nonuniformities in the electrodes, which cause locally high fields. Next, if the gap is illuminated by a short wavelength (short relative to the energy gap) laser pulse, a region of surface photocarriers will be created. This effectively shorts out the gap, and a voltage will appear at the output. This voltage will persist until either the gap reverts to the high-resistivity state, through carrier recombination, or the charge stored in the charge line is depleted. The time duration in the charge-line mode can easily be adjusted by changing the length of the charge line.

For the single-shot experiment the laser pulses were produced by an actively- and passively- mode locked and Q-switched Nd:YAG laser which produced pulses of 30 ps-FWHM at 1.06 μm. The semiconductor used was semi-insulating silicon. Even though silicon has a very long recombination lifetime (microseconds), the laser repetition rate was even longer (≈0.5 Hz). However, this did allow for nearly rectangular, adjustable time duration, electrical pulses to be made. For this experiment, the charge line was made from 0.141 in. semirigid coaxial cable.

4C(ii) Measurement Technique

Figure 4C.2 shows the apparatus used in this experiment. The laser [3] used was an actively- and passively-mode locked and Q-switched Nd:YAG system, which produced 30-ps FWHM pulses at 1.064 μm. Passive mode locking was achieved through the use of a saturable absorber dye dissolved in di-chloro-ethane. The active mode locking was accomplished with an RF-driven acousto-optic modulator. Single pulses were picked out of the pulse train of ≈ 20 pulses using a krytron driven tandem electro-optic switchout. The repetition rate was something less than one Hertz, so this was truly a single-shot experiment.

A coaxial charge line was used to control the length of the electrical pulse, and a battery supply was used to control the amplitude. Different pulse widths could be obtained by merely changing the length of charge line. The length of the pulse corresponded to one round trip in the coaxial cable. This is due to the nature of the photoconductive switch; even in the "on" state, the gap resistance is not zero. This nonzero resistance gave rise to reflections which propagated back down the charge line towards the charging resistor. Since the charging resistor was relatively large (10 k-ohm), the resistor behaved as an open circuit and the boundary condition at the resistor was that of zero current. The second reflection was therefore a voltage pulse of nearly equal magnitude, but opposite in sign, which effectively canceled the voltage on the charge line. At the output of the switch, one observed the voltage pulse, corresponding to one round trip in the cable, followed by several other reflections which were very small in size, and were due to the non-ideal nature of the terminations. The scope used to observe the high speed signals was a Tektronix storage scope with sub-nanosecond resolution.

The high speed pulse was then conducted to the junction via 0.141 in. semirigid coaxial cable and 18 GHz SMA connectors. Devices were placed in a glass helium dewar with a liquid nitrogen outer dewar, so that the total propagation distance from switch to device was about one meter. The end of the cable was pressed onto the junction using a cross sectional slice of indium wire to make a cold weld.
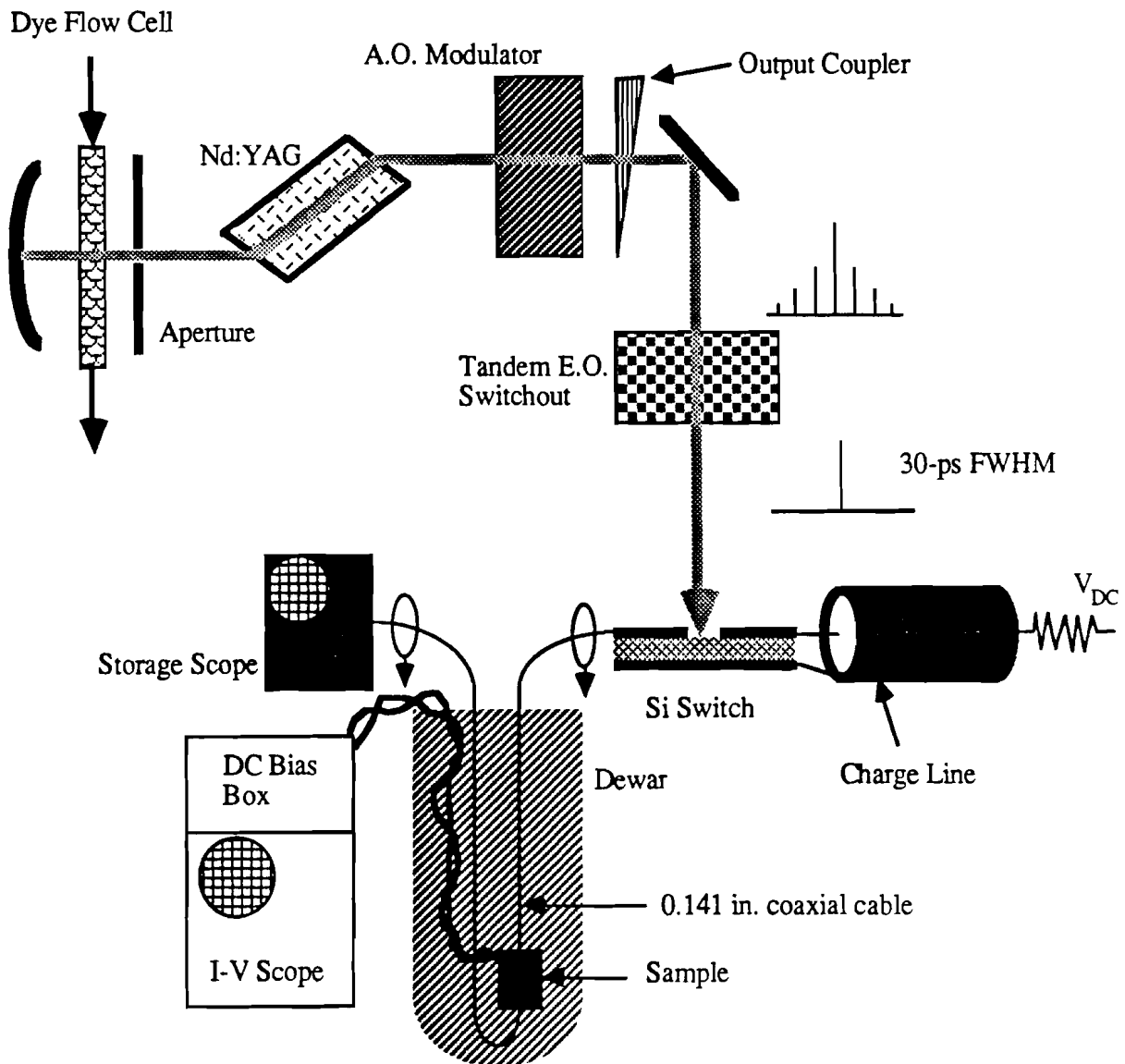
Dye Flow Cell

A.O. Modulator

Output Coupler

Nd:YAG

Aperture

Tandem E.O. Switchout

30-ps FWHM

Storage Scope

V_{DC}

DC Bias Box

Si Switch

Dewar

Charge Line

I-V Scope

0.141 in. coaxial cable

Sample

Figure 4C.2 Experimental setup.

Finally, another cable was attached to the output of the junction, and routed out of the dewar to be terminated in a 50 Ω load at the storage scope. This allowed each laser shot to be monitored, as the pulses arrived at the storage scope with very little degradation. A laser shot with unusually low amplitude would result in a very small electrical pulse at the scope and so could be ignored. Larger than normal pulses, however would not affect the experiment as the Si switch was driven into saturation with this system.

The dc I-V curve for a particular junction was traced out using a home-built bias box which operated at tens or hundreds of Hertz. DC biasing, as well as temporary device grounding, could also be provided from the same circuit. Four-wire connections to the junction were made using twisted pairs of wires inside the dewar, and twisted pairs of coaxial cables outside.

In practice, assuming the liquid helium had been transferred in time to achieve a functioning junction and that the laser was working, the experiment would be performed as follows. First, a charge line length would be chosen and the bias voltage, V_{dc}, would be set. Next, the bias current would be set to a particular value, and after the laser shot, switching (or not switching) could be determined by checking the junction state using the I-V scope. Finally the junction would need to be grounded (reset) using a push-button built into the bias box for this purpose, provided the last laser shot had indeed resulted in the junction switching into the voltage state.

After performing several runs using this procedure, it became apparent that the junction could in fact be switched by the abundant RF noise present whenever the laser fired. To cure this, all cables were wrapped in aluminum foil and then grounded. This included the high-voltage lines for the laser flashlamps, as well as the cables associated with the junction dc biasing network. Despite the fact that these cables were coaxial, it appears that the sheath, which was stranded wire, behaved as a waveguide operated below

cutoff, but was simply too short to be effective. At the top of the cryostat, all bias wires were fed through inductive ferrite beads. In addition, the dewars were enclosed in a double mu-metal magnetic shield, and then grounded. Finally, the switch output was attenuated using an 18-GHz 20 dB attenuator. This allowed the noise to be attenuated while the signal amplitude was increased. The data presented in the next section were taken *after* these precautions were taken.

4C(iii) Results

Experiments were performed using two different size junctions; large and small,

where the size was relative to the Josephson penetration depth, λ_j. The device parameters

are given in Table 4C.1. The mean free path for these lead films was 35 nm.

TABLE 4C.1	Large Area Junction	Small Area Junction
Dimensions (l)	$420 \times 240 \ \mu m^2$	$50 \times 50 \ \mu m^2$
Area	$10^{-7} \ m^2$	$2.5 \times 10^{-9} \ m^2$
λ_j (approximately)	$300 \ \mu m \ (\lambda_j < 1)$	$250 \ \mu m \ (\lambda_j \gg 1)$
Critical Current Density	$3.8 \ A/cm^2$	$5.2 \ A/cm^2$
Critical Current	$3.8 \ mA$	$0.12 \ mA$

I-V curves for these same junctions are shown in Fig. 4C.3. The curves indicate

that these were indeed high quality junctions. Trapped flux could be freed in these

junctions by raising the entire experimental rig above the surface of the liquid helium

(and so raising T above T_c), so these curves truly represent the maximum critical

current.

Data were taken using a variety of pulse lengths as excitations, ranging from

less than one to several nanoseconds. A typical pulse showing very good signal to

noise is shown in Fig. 4C.4. The lower limit was defined physically by the smallest

charge-line which could be constructed. The nature of this experiment was such that

the result was a phase diagram. For values of the pulse width and amplitude which

were smaller than the critical value, no switching occurred, while those values which

were larger resulted in a switching event. The critical combinations of pulse widths
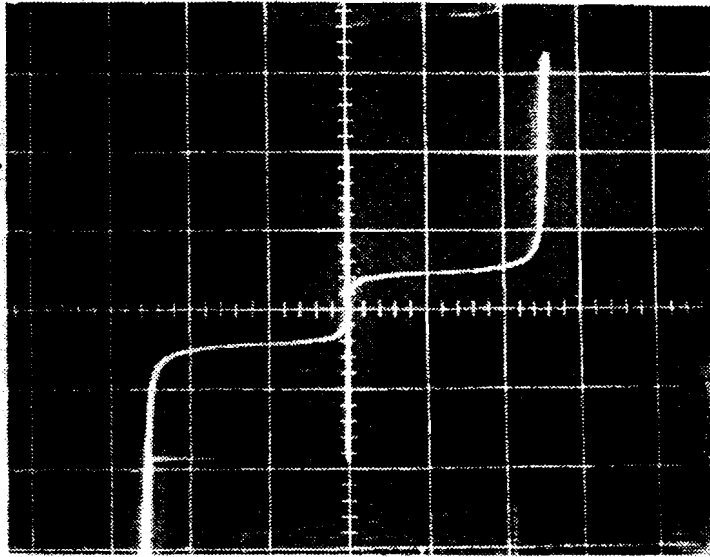
Figure 4C.3a Large area junction I-V curve. Scales are 2mA/div (vertically) and 1mV/div (horizontally)
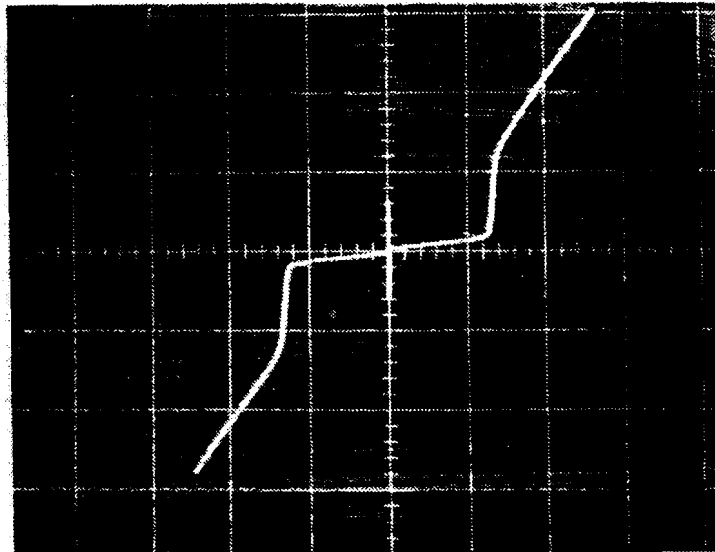
Figure 4C.3b Small area junction I-V curve. Scales are 0.2mA/div (vertically) and 2mV/div (horizontally)
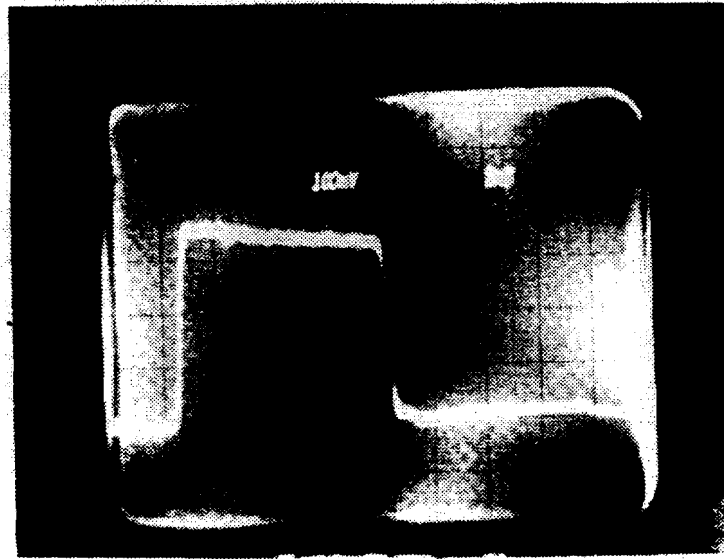
Figure 4C.4. Measured silicon switch output. Scales are 100mV/div and 2ns/div (horizontally). Slow decay during on state was due to carrier recombination.

and amplitudes defined the switching threshold for a particular junction.

Figure 4C.5 shows data taken for a large area junction. Two important points to note on the plot are the intercepts: I_0 and ΔI. The I_0 intercept is simply the dc critical current (compare with the measured value from Table 4C.1). ΔI on the other hand is the pulse amplitude required to switch the junction without a dc bias.

For the small area junction, it was found that all pulse widths fell on essentially the same threshold curve. A typical such curve is shown in Fig. 4C.6. The lack of deviation for different pulse widths was an indication that the junction response was faster than the apparatus. This was expected, since the area was less than the penetration depth, λ_j, and the capacitance was also small .

Figure 4C.5 Phase
diagram for large
area junction.
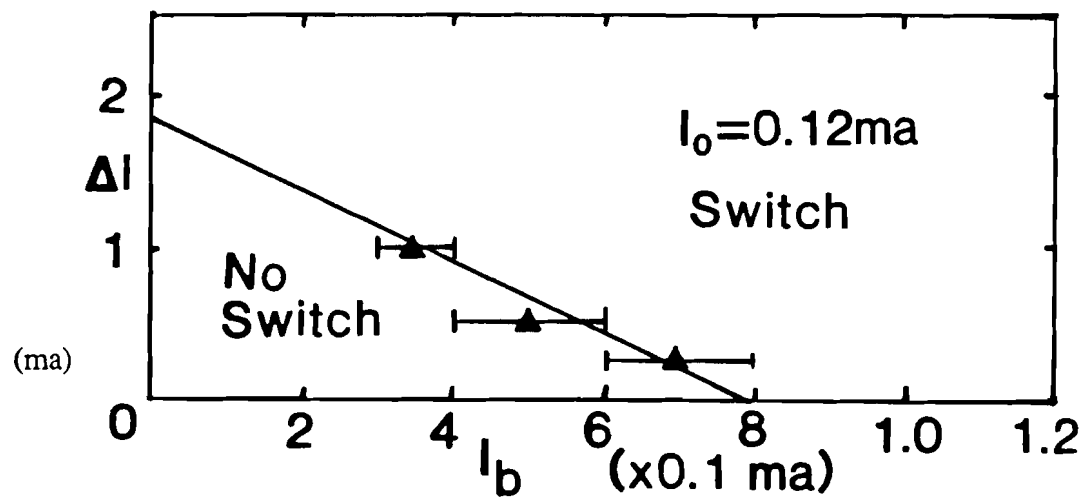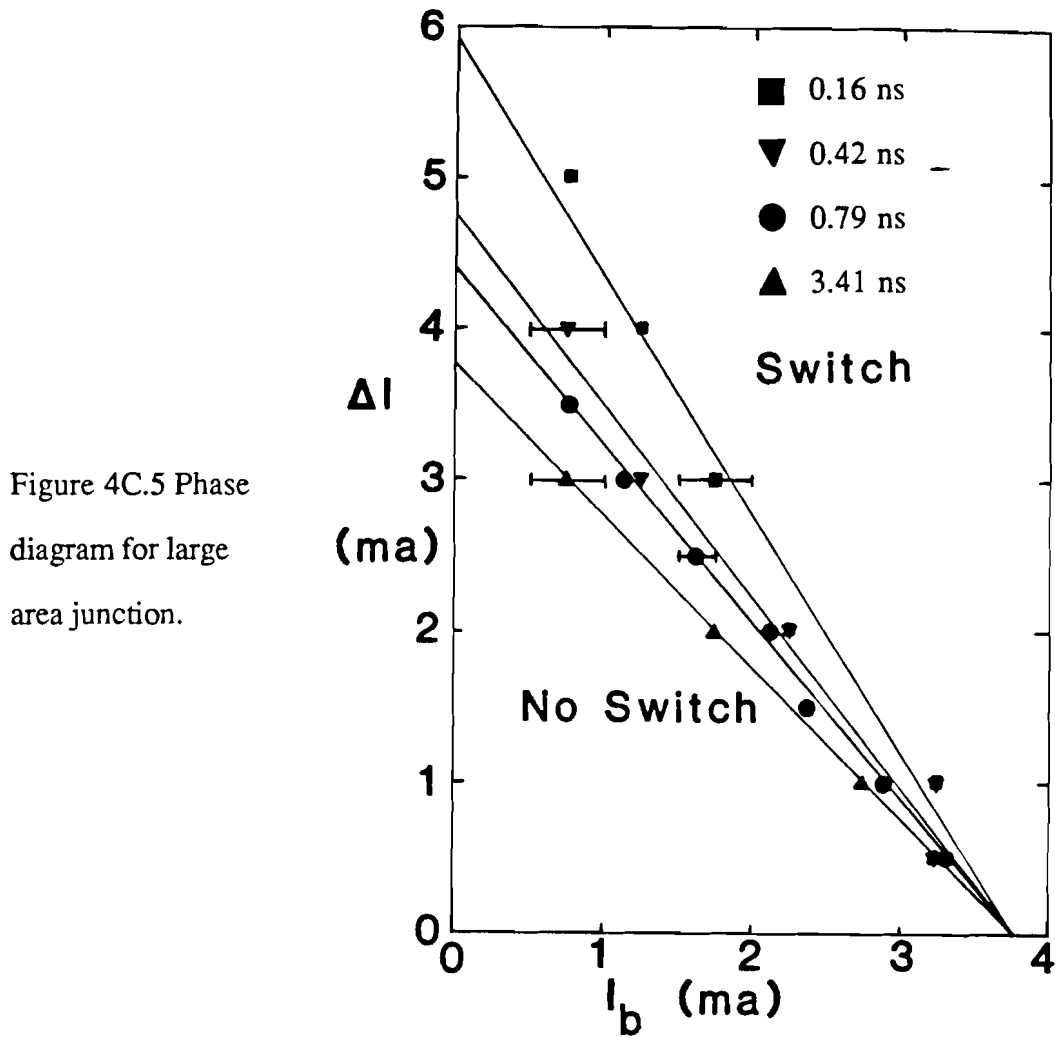
Figure 4C.6 Phase diagram for small area junction. Pulse width is ≈ 100 ps.

4D Flux Flow Theory

In order to model the results of these experiments, let us start by using the the equations proposed by Dhong and Van Duzer [17]. Using the pendulum analogy, the minimum width control pulse, τ , can be divided into two portions, τ_1 , the time required to swing the pendulum to the critical point and, τ_2 , the time required to impart the necessary energy to the bob to overcome the damping. This situation is shown schematically in Fig.4D.1.
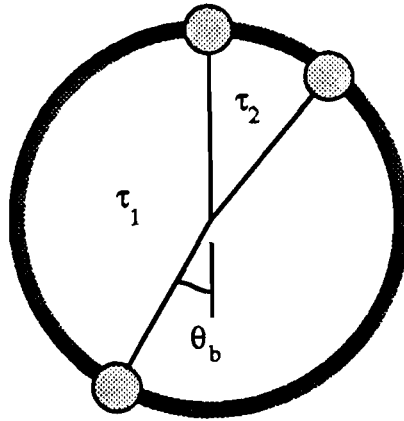
Figure 4D.1 Pendulum analog. θ_b is the applied bias torque.

The times τ_1 and τ_2 are calculated to be (Ref. [17]):

$$\tau_1 = \sqrt{\frac{2C_j\Phi_0}{\pi I_0}} \, \sin^{-1}\sqrt{\frac{\pi I_0}{4I_b}} \approx \sqrt{\frac{\pi C_j\Phi_0}{2I_0}} \tag{4D.1}$$

$$\tau_2 = \Phi_0/(R_N I_0) \tag{4D.2}$$

For the large area junctions used in the experiment, C_j = 16 pF, R_N = 0.13 Ω,

and I_0 = 9.0 ma. Using these values, one computes a value of τ of about 4 ps. Clearly, this is almost three orders of magnitude **too small** compared to the experimentally determined values shown in Fig. 4C.5.

Given such a large disparity between the predicted and measured values, one needs to seek another transient limiting mechanism. It has been known for some time that large junctions exhibit flux flow behavior when the current bias is switched from one value to another [24]. The origin of this flux is the self-induced edge field due to the bias current. As the flux drags through the junction after a change in bias, the viscosity it experiences results in a significant time delay. This viscosity is caused by the finite junction resistance. To understand how flux is redistributed in a large area tunnel junction, consider the diagram in Fig. 4D.2.

As shown in the figure, for a large area junction biased in the zero voltage state, most of the current is conducted along the outside edges of the junction. After the junction has switched into the voltage state however, the current becomes evenly distributed, and so the magnetic field becomes linear. The location of the average field is marked by the dots in each picture. After the switching event, the average location of the field has moved a distance L.

To calculate the time required for the field to move this distance, we first need to know the Lorentz force:

$$f_L = \eta v = J \, \Phi_B \qquad\qquad (4D.3)$$

The electric field is given by:

$$E = \Phi_B v / L \qquad\qquad (4D.4)$$
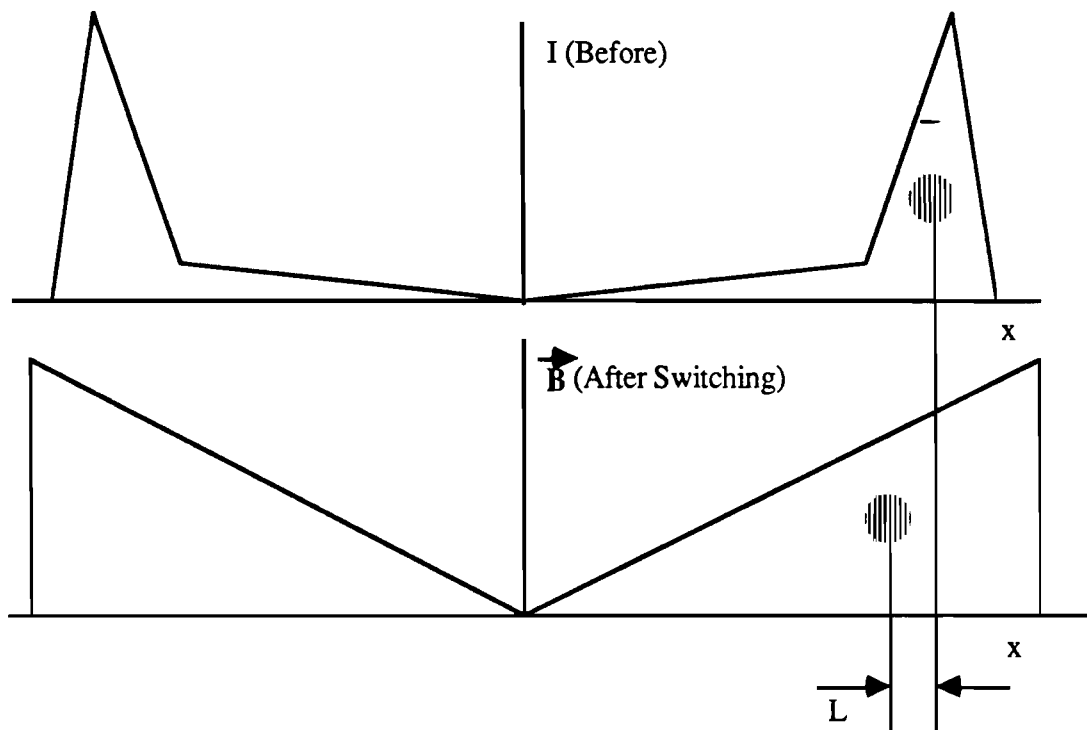
Figure 4D.2 Flux flow diagram. Note that it is the current distribution shown before switching and magnetic field shown after switching to the voltage state. The average value of magnetic field is shown as the shaded dot.

The energy dissipated is due to the normal current which extends one penetration depth into the conductors, and so the flux flow resistivity is just the normal state resistance:

$$\frac{1}{2} \frac{1}{\rho_f} E^2 = \frac{1}{2} \eta v^2 \qquad (4D.5)$$

$$\Rightarrow \rho_f \equiv \frac{\Phi_B^2}{\eta L^2} \qquad (4D.6)$$

and $\rho_f = \rho_N$

$$\therefore v = \frac{J\rho_N L^2}{\Phi_B} \qquad \text{and so:} \quad \tau = \frac{L}{v} = \frac{\Phi_B}{J\rho_N L} \qquad (4D.7)$$

To use equation (4D.7) to perform a sample calculation using the measured values of the large area junction we need to calculate the current density:

$$J = \frac{I_b + \Delta I}{A} = 5 \times 10^4 \text{ A/m}^2$$

$$\rho_N(\text{Pb}) = 3.1 \times 10^{-8} \Omega\text{m} \; ; \; \lambda_L(\text{Pb}) = 37 \text{ nm}$$

We can estimate L using the measured resistivity ratio (6.4): $\rho_1 = 1.05 \times 10^{-15}$

Ωm^2 and $\rho(300K) = 1.92 \times 10^{-5}$ Ωcm, so the mean free path, $l = \rho_1 / \rho_{4K} = 35$ nm.

$$\Phi_B = \frac{\mu_0 I}{2L} \lambda_J 2\lambda_L = 6.97 \times 10^{-16} \text{ Wb}$$

$$\Rightarrow \tau = \frac{L}{v} = \frac{\Phi_B}{J\rho_N L} = 4.65 \text{ ns}$$

Clearly, this calculation gives a much more reasonable result. In addition the pulse width τ is seen to be inversely proportional to the total current, so a plot of inverse pulse width versus bias current should be linear. This is shown in Fig. 4D.3. For all but small bias values, there is very good agreement with Eq. 4D.7.
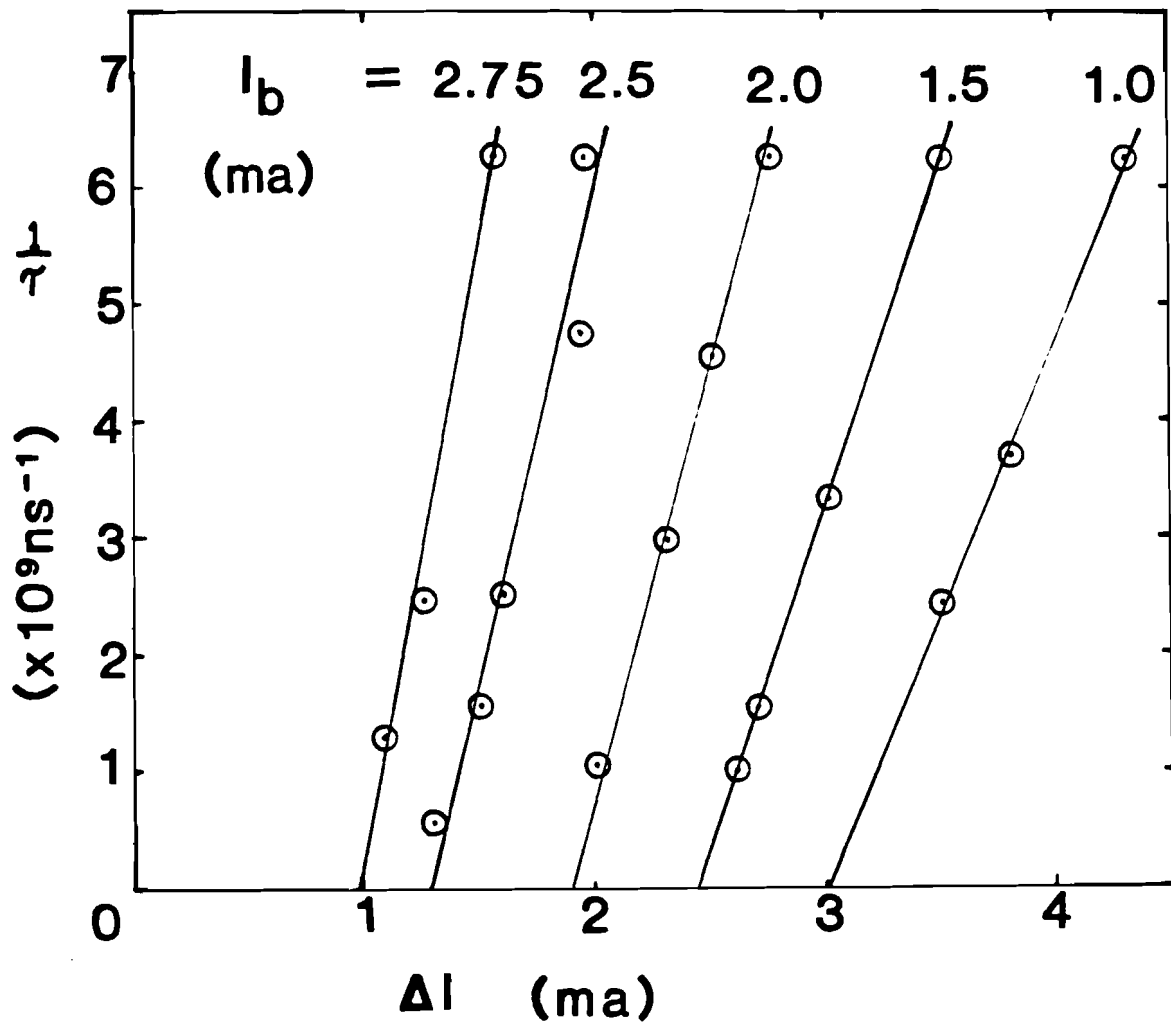
Figure 4D.3 Large area junction results replotted.

4E Limitations Of The Theory

Given the somewhat surprising result that these junctions were slower than expected, some further experiments were immediately attempted. Namely, for a material dependent phenomenon, it seemed reasonable to repeat the experiment with a different material. This was attempted for junctions made with lead and varying amounts of indium or bismuth. However, it soon became obvious, given the nature of these lead films, that no useful devices could be produced.

In order to overcome this problem, two major decisions were made. First, it was clear that a new source of devices was necessary. Devices, which were high quality, fast, and even possibly recyclable were required to enable experiments to be performed. Also, a laser system was required which would offer the speed, reliability and ease of use that these new devices would require.

The first requirement was satisfied by the availability of lead alloy fabrication facilities at the National Bureau of Standards (NBS) in Boulder, Colorado. I was invited to make use of their facilities to produce virtually state-of-the-art Josephson devices. This procedure is described in Chap. 6.

In order to be sure that the measurement system would be capable of characterizing these faster devices, the Nd:YAG laser was replaced by the very much faster (both in pulse width and repetition rate) laser described in the next chapter.

Electro-optic Sampling

This chapter opens with a brief introduction to the optics involved in these experiments. Both the laser and the Pockels effect are described along with a new detection scheme developed by the author for these experiments. This scheme was required by the very small voltages produced by the junctions.

Next, the cryogenic implementation of the electro-optic sampler is described. The development of this capability was essential to allow time resolved measurements to be made on superconducting devices and circuits. This was accomplished by the author in a series of steps, culminating in an unprecedented rise time measurement of 360 fs. Furthermore, it is shown that the frequency content of this signal exceeds the energy gap frequency of the electrodes used in the transmission line.

Finally, a brief study of the propagation of these ultrafast rise time pulses is presented. The purpose of these measurements was to insure that the pulses being applied to the junctions were not distorted during the propagation from photoconductive switch to device. The issue of signal propagation is an important aspect of any high speed experiment and will be discussed further in Chap. 8.

5A(i) CPM Laser

The underlying speed of the electro-optic sampling technique is the direct result of the laser used to make the measurement. This laser is the Colliding Pulse Mode Locked (CPM) system [3], and in its present form is capable of generating pulses as short as 27-fs FWHM [25]. The CPM laser has been described in the literature, so only a brief description of the version used in these experiments will be given.

A commercial Coherent Ar^+ laser (Innova model I-100-20) which produces nearly 10 Watts of cw light at 514.5 nm is used as the pump for the CPM laser. The argon laser is normally run in the range of a few watts and an optical feedback loop is used to control precisely the output power and to limit the noise to about 0.3% RMS.

The CPM laser itself is a dye laser using both a gain medium, Rhodamine 6G and a saturable absorber, DODCI (DiethylOxa-DicarboCyanine Iodide). These two dyes are a well-matched set and are used together often in dye lasers. The CPM laser however, is a somewhat different animal, as shown in Fig. 5A.1.
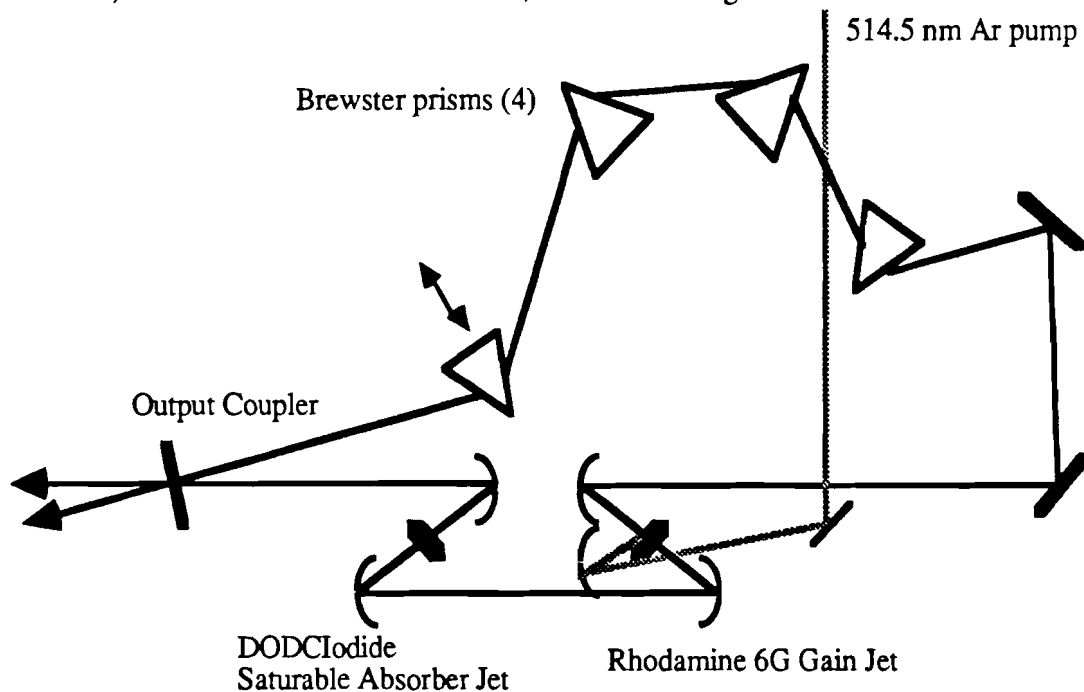
Figure 5A.1 Colliding Pulse laser system.

As shown in the figure, the laser is laid out in a ring geometry. The Rhodamine dye is flowed in a commercial dye jet (thick) and together with the DODCI jet (thin) produces passively-mode locked pulses. These pulses counter propagate in the laser and become shortened when they collide in the saturable absorber. This accounts for the two beams shown leaving the cavity in the figure.

Next, the four Brewster angle prisms are placed into the cavity. These prisms serve to compensate for any linear dispersion which occurs in the propagation paths inside the cavity, through the introduction of negative dispersion. By varying the amount of glass in the beam path, the pulse width can be minimized. The resultant autocorrelation is shown in Fig. 5A.2.
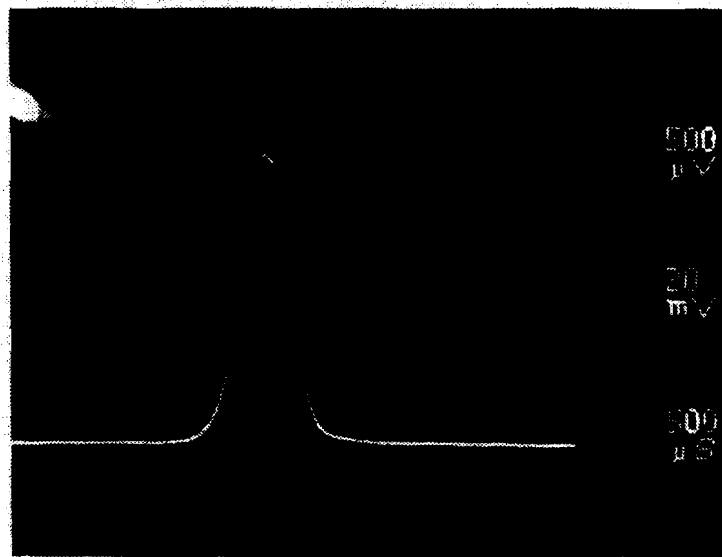
Figure 5A.2 Autocorrelation [3] of the CPM laser. Pulsewidth is calculated at Full Width and Half Maximum (FWHM) and assumes a hyperbolic secant shape, so that the measured width is multiplied by 0.6482 to obtain the actual pulse width of ~70 fs.

Although the record for this type of system is 27-fs FWHM, the stability is much better for the longer pulse widths. The exposure time for Fig. 5A.2 was 1/2 second and there is virtually no deviation from a single trace. The reason more laboratories do not make use of this very fast source is the dye system itself. Both dyes have unknown health hazards, and in particular, the DODCI is very short lived. If no particular precautions are taken, the DODCI has a useful life of about two weeks. In order to extend the useful life of the dye, several factors were identified as contributing to the dye dying prematurely. Basically, air (oxygen), water, heat, old dye and light all have detrimental effects on the dye lifetime. To mitigate these effects slightly, the following changes were made. A cooling network was placed into the dye reservoir, although the temperature setting had to be warm enough to prevent condensation (just below room temperature). All fittings and hoses were replaced with either 316 stainless steel, or non-staining tubing. A non-staining tube is one that can be completely cleaned after immersion in the dye: teflon is, tygon is not. The filter assembly, which was used to remove air bubbles from the dye, was replaced by a disposable cartridge type with a cleanable housing. Finally, some tubing was replaced with a type that had a black outer tube. The result of these changes was an increase in the average dye lifetime by a factor of two.

While the Rhodamine dye was considered relatively inert, it turned out that it too suffered the same problems as the DODCI, although not to the same degree. In fact it turned out that the brass fittings used were tinting the dye green. Many of the same improvements have been applied to the Rhodamine system and the dye can now be expected to last many months.

5A(ii) Pockels Effect

Once an electrical signal has been generated using a CPM laser pulse and the photoconductive switch, it has to be detected using the second optical pulse from the CPM laser. The transformation between the electrical regime and the optical regime is accomplished through the use of the Pockels effect.

Basically, the Pockels effect alters the state of polarization of an electro-optic medium in the presence of an electric field. If the medium is placed between crossed polarizers, the birefringence results in a change in intensity. Since this change is due to changes in the crystal on an atomic scale, the speed can be as fast as a few femtoseconds.

Specifically, if polarized light is incident on an electro-optic material, the two orthogonal polarizations will each see a different index of refraction. For small distances, 1, the total phase shift is:

$$\delta = \frac{2\pi}{\lambda} l \Delta n \qquad (5A.1)$$

where λ is the free space wavelength and Δn is the birefringence. The output beam will have a net polarization change of δ. This change of polarization can be converted to a change in intensity by placing the electro-optic modulator between crossed polarizers. The change in intensity can be maximized if the input beam is oriented with a 45 degree polarization. In that case the transmitted intensity, I, will be:

$$I = I_0 \sin^2 \left[\frac{\delta}{2} \right] \qquad (5A.2)$$

where I_0 is the intensity of the input beam. The transmission is just I/I_0, and is plotted in Fig. 5A.1. The transfer function is most linear in the central region around the 50% transmission point. However, the modulator will have a certain amount
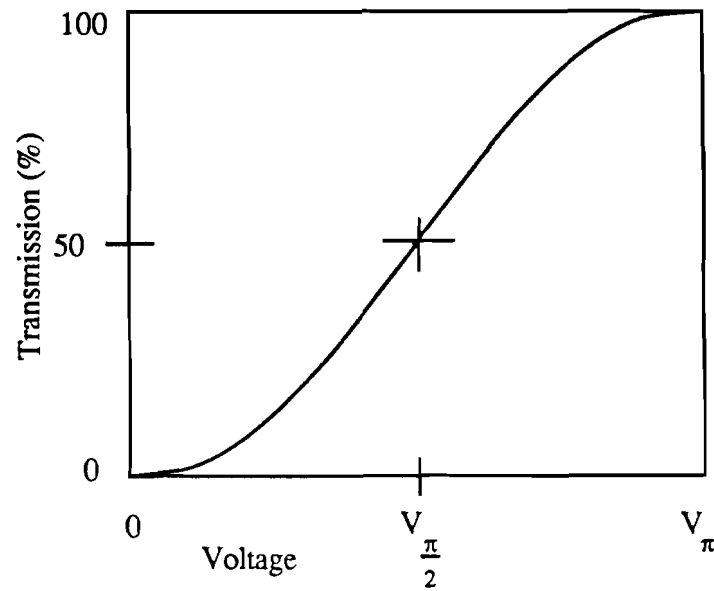
Figure 5A.1 Modulator transmission function

of static birefringence, even in the absence of an applied field. By placing a variable retardance device in the beam path, between the polarizers, it is possible to "optically bias" the modulator to this 50% point. In these experiments this was accomplished with a commercially available Soleil-Babinet compensator.

In practice, a given modulator can be calibrated by using the compensator to find both the minimum and maximum transmission points. The 50% point is then defined as the midpoint. Next the voltage scale can be calibrated by simply applying a known voltage and measuring the resultant change in intensity. Since the half wave voltage,

V_π, is usually in the kilovolt range for the modulators used in these experiments, the assumed linearity is a very good approximation. Finally, the specific choice of material, lithium tantalate, is based on previous experience, and is the best compromise, among the competing qualities of sensitivity, robustness, ease of processing, etc.

5B Microvolt Sampling

As shown in the previous section, one can change the transmitted intensity through a modulator by an applied voltage. The specific implementation used in these experiments is shown in Fig. 5B.1.
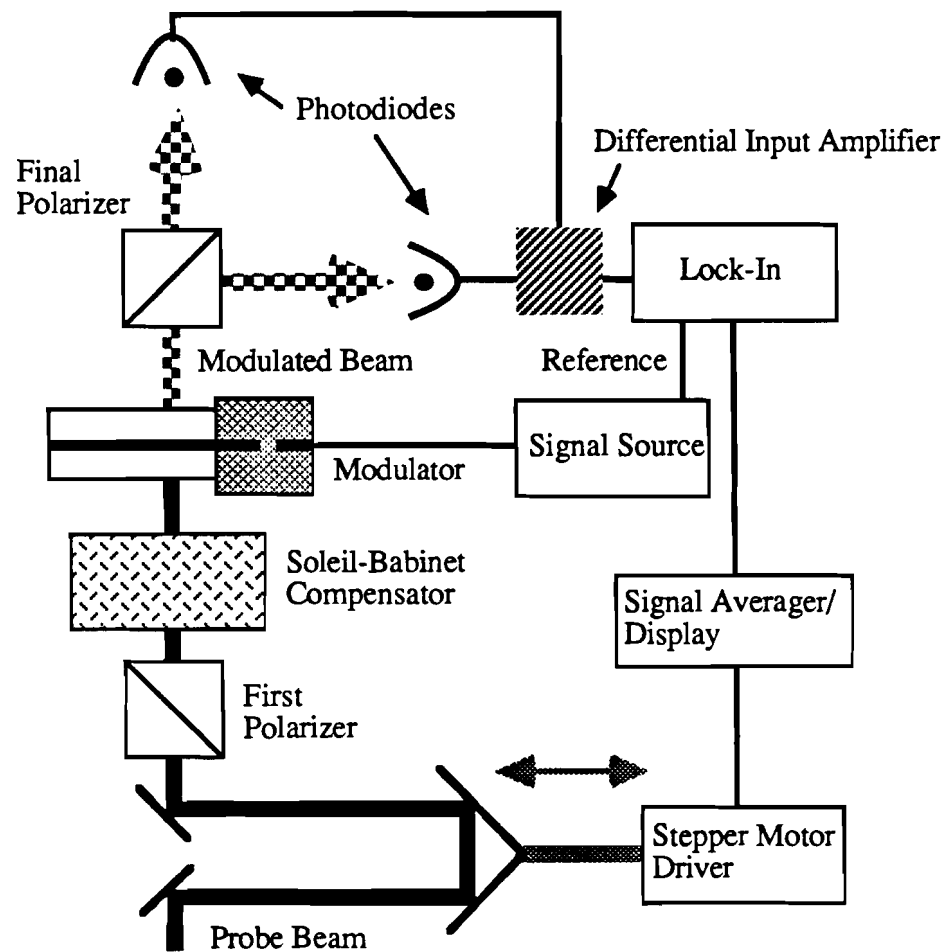
Figure 5B.1 Sampling system schematic. Excitation beam is omitted for clarity.

In absolute terms, the change is very small. Most electrical signals of interest are in the volt or even millivolt range, whereas the halfwave voltage for most of the modulators used was in the kilovolt range.

The first step in measuring a real signal is provided by the laser itself. With a repetition rate of 100 MHz, small signals can be quickly integrated up into large ones.

Next, a lock-in amplifier is used. As shown in Fig. 5B.1, the lock-in amplifies a particular frequency which is used to modulate the experiment. In the case of electro-optic sampling, this modulation is easily applied directly to the photoconductive switch as its bias. The advantage of this scheme is that the lock-in frequency can be chosen in a regime of low noise.

For the sampling system, the major source of noise is the laser itself. The noise spectrum for the CPM laser is shown in Fig. 5B.2.
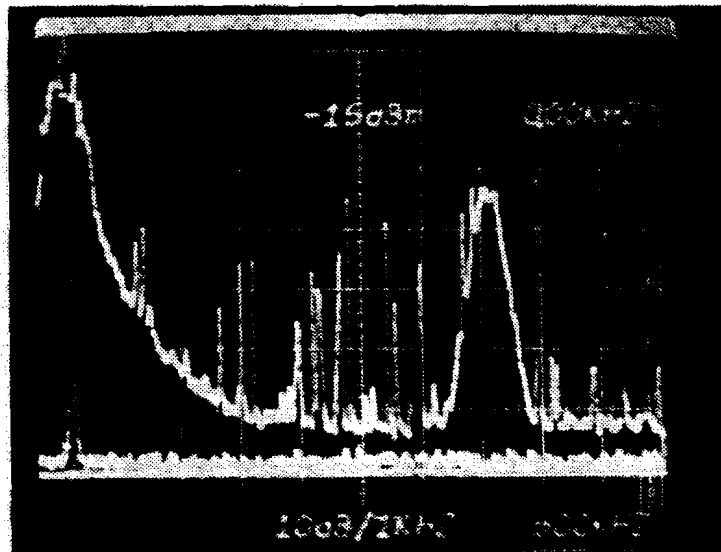
Figure 5B.2 Noise spectrum of CPM laser. Horizontal scale is 500 kHz/div. Vertical scale is 10 dB/div. Lower trace is noise spectrum of FND 100 photodiode with no incident light. Traces were taken with 1 kHz bandwidth.

As shown in the figure, there are several features, which may be due to various resonances inside the cavity (they are not present in the argon laser spectrum), but the general behavior is 1/f until the noise floor is reached at about 2 or 3 MHz. The spectrum was taken using an EG&G FND-100 photodiode which was used as a detector for a Tektronix 7104 spectrum analyzer (0 - 5 MHz).

From the preceding discussion, it would appear that the obvious solution would be to operate the lock-in above this frequency. However, the limit for the PAR-124A being used was only 100 kHz, so the improvement was not dramatic.

The next step was to change the lock-in. This is not quite so simple, as the only commercially available lock-in which runs at high frequency (PAR-5202), had very poor performance in our application. In addition to inadequate overall sensitivity, this unit lacks the capability to perform a differential measurement. As shown in Fig. 5B.1, when the two polarizations are separated in the final polarizer, an analog differential amplifier is used to cancel the noise partially, and to increase the signal level (note that even in the absence of noise the signal level would be increased by a factor of two).

However, as the frequency increases, this differential amplifier becomes a very complex beast indeed. In conjunction with the 5202, an Analog Modules GaAs differential amplifier was used, and much of the data reported in the following sections used this scheme. For those experiments the modulation was limited to the 2-4 MHz range, as some other link in the detection chain experienced a frequency roll-off, probably the detector diodes themselves.

The next incremental improvement was made by replacing the 13-MHz Analog Modules amplifier with a Tektronix oscilloscope. The particular scope, a 7000 series, allowed two signals to be subtracted, as well as an upper bandwidth limit of 20 MHz. This bandwidth limit helped to limit the noise presented to the lock-in outside the

passband.

Finally, an improved solution was found. On the one hand, the laser has a noise floor at 5 MHz, and on the other hand, the best commercially available lock-in only runs to 100 kHz. Therefore, a mixer was constructed to mix down the high frequency modulation to match the 124A lock-in. This method yielded improved signal to noise, despite the ≈ 5 dB conversion loss of the mixers, due to the far superior sensitivity (two orders of magnitude) of the 124A. The layout is shown in Fig. 5B.3.
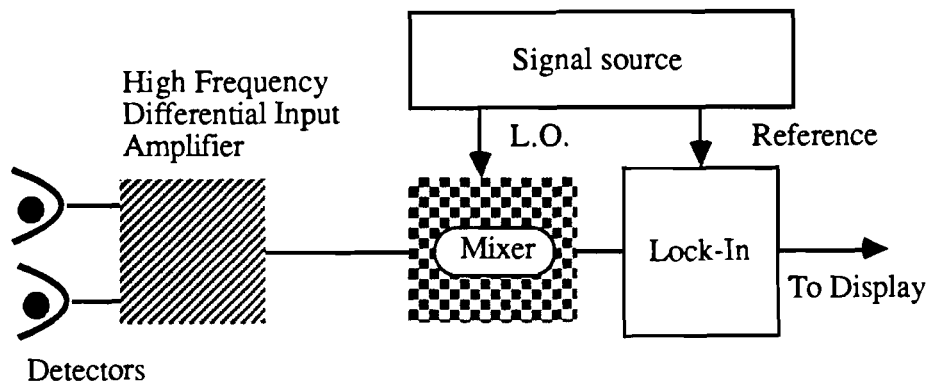
(a) High frequency differential amplifier used with single mixer
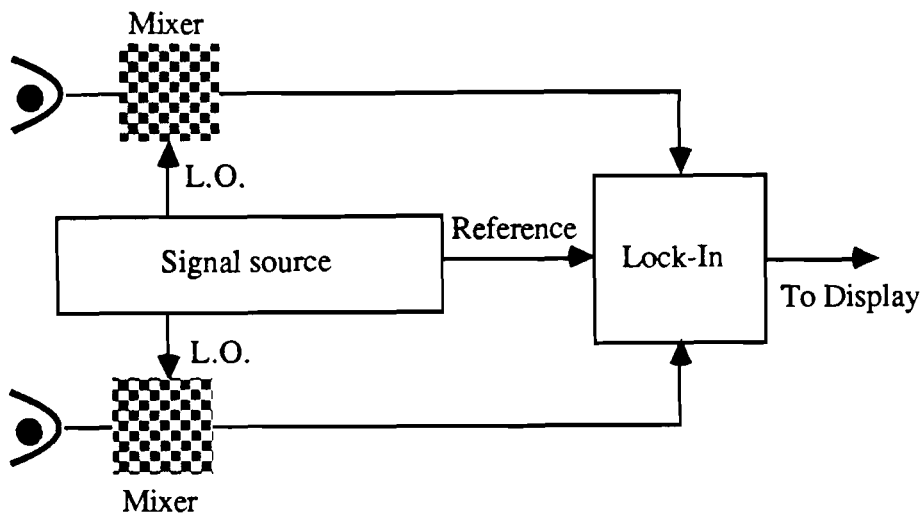
(b) Individual mixer scheme using low frequency differential amplifier in lock-in.

Figure 5B.3 Mixer schematics
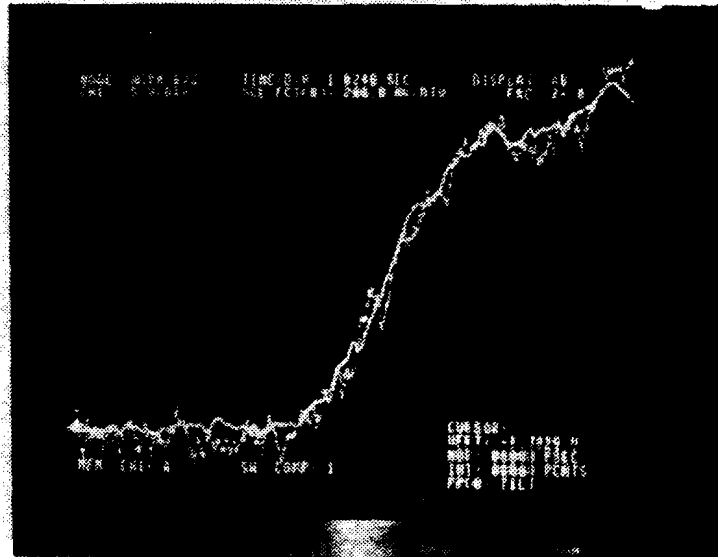
Figure 5B.4 Actual measured risetimes for comparison of detection systems.
Mixer based system has significantly higher signal to noise ratio.

A comparison of the 124A / mixer based- and 5202 based systems is shown in Fig. 5B.4. The data were taken using a laser driven modulator, and both systems were tested immediately following one another. The higher signal-to-noise ratio of the mixer based system is clearly visible.

Finally, several detail changes were made to improve impedance matching of the various blocks in the system. Since the mixers are all 50 ohm impedance, while the lock-in had a maximum signal-to-noise ratio at an input impedance of ≈100 kohm, the lock-in is run in transformer mode. The transformer matches the input impedance of the photodiodes to the lock-in preamp. This allows the lock-in to be run in a relatively

low noise regime, and still operate at a frequency above the usual noise sources such as 60 Hz line noise.

In addition, matching of the diodes to the mixer inputs was addressed. The diodes are rated at 350 MHz bandwidth into 50 ohms. Clearly, this bandwidth is unnecessary, so the diodes were terminated into ≈ 1 kohm to increase the signal level at the expense of the bandwidth. This practice may in fact be the reason for the upper limit in bandwidth to the few megahertz frequency range.

The signal source used originally was an HP test oscillator which was in turn used as a reference for a digital circuit which produced the lock-in reference, local oscillator (L.O.) and modulation signals for the photoconductive switch. This system had an upper limit of 2 MHz defined by the requirements placed on the digital electronics. To overcome this limitation, an HP 3326A has been used. This system can produce both the reference and L.O. signals, as well as the modulation signal. Even with the bandwidth limitations elsewhere in the system, this mixing scheme has still been run as high as 3.5 MHz.

5C Cryogenic Implementation

In order to characterize superconducting electronics on a picosecond timescale, the electro-optic sampling system had to be modified. For the initial experiments, the modifications were minimal: a helium dewar was used for the experiment, and long cables were used to route the signals into and out of the cryogenic environment. However, it was always the intention to construct an integrated system, although this was achieved in a series of steps.

First, a dewar had to be designed for such an integrated system. This was accomplished by a special design with a total of four in-line windows (all neither crystalline nor birefringent) to allow laser beams to pass through undistorted. The inner windows were fused silica and the outer ones were generic optical quality glass with no coatings. In addition, the liquid helium which is placed in the dewar must also be non-distorting, so the temperature in the dewar must be reduced to the superfluid or

λ point (by reducing the pressure in the dewar). At this temperature (2.18K), all boiling stops in the liquid, except for a thin layer at the surface. This technique had the added advantage of excellent thermal equilibration, as no temperature gradients are allowed, which may help to prevent thermal birefringence in the sampling crystal.

The first experimental step was to place one part of the sampling system into the cryogenic environment at a time. The sampling geometry used was a coaxial type with a microstrip geometry sampling crystal placed in a cut cable. This layout is shown in Fig. 5C.1. Using 0.085 inch semirigid coaxial cable and 40 GHz connectors, a rise time of 16.4 ps was measured, as shown in Fig. 5C.2, in a cold (liquid helium level just below the sampling crystal) dewar by placing the sampling crystal into the dewar [26].
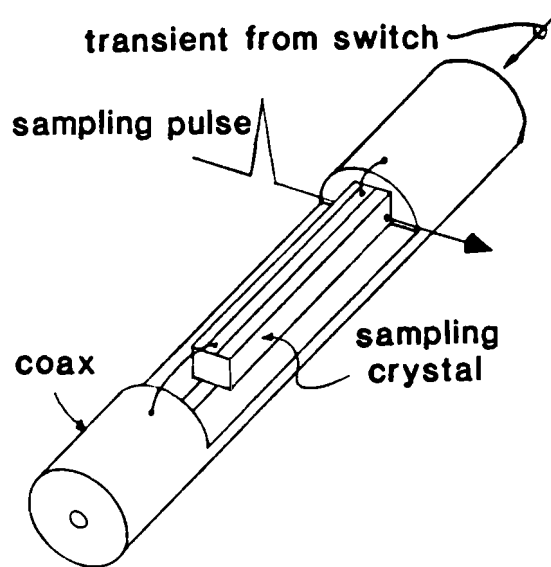
Figure 5C.1 Coaxial sampler geometry. Sampler was built from 0.085 inch cable
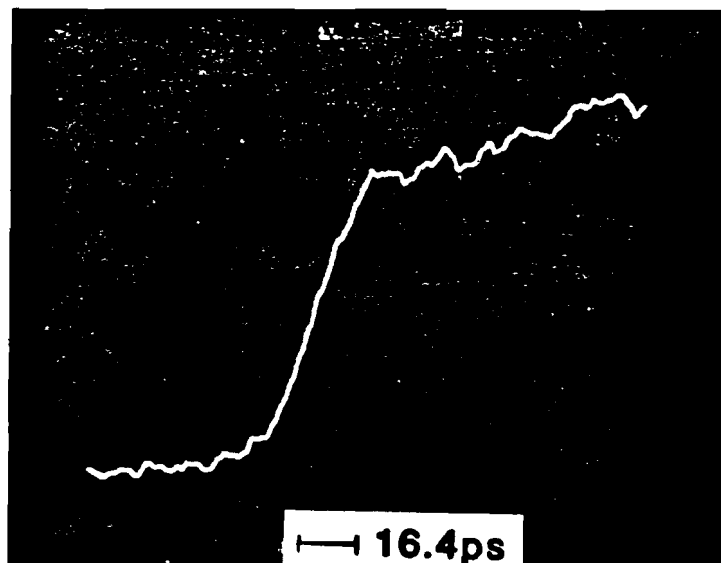
Figure 5C.2 Cryogenic sampler rise time of 16.4 ps measured with cold crystal

and room temperature signal source.

The rather long rise time was a direct result of the long cables (several feet) required to route the signal from the room temperature switch into the dewar.   —

The next step was to integrate the switch and the sampling crystal into the same structure. Several structures were considered, and the first choice was to use the reflection mode geometry. In this geometry the sampling crystal is coated with a nonconductive dielectric reflective coating. This geometry promised several advantages. First, it had already been demonstrated at room temperature. The very short propagation distances had led to a rise time of 0.75 ps at room temperature [27]. To improve on this basic structure, the geometry of Fig. 5C.3 was used.
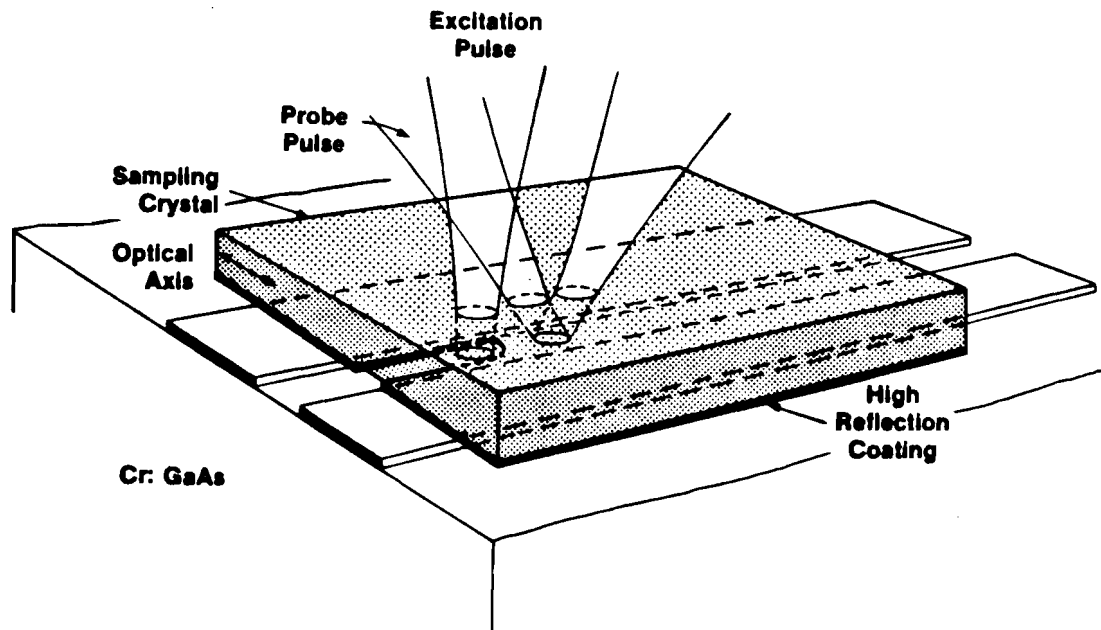
Figure 5C.3 Gapless sampling structure. The high reflection coating was a dielectric stack, which provided both high reflectivity and electrical insulation. Both the probe and excitation beams could be moved up and down the transmission line.

This gapless structure allowed the switch to be defined by the laser excitation beam, and not a predefined gap. In addition to allowing even shorter propagation distances, this structure allowed more flexibility in changing the propagation path length. A sampler made in this geometry using lead electrodes had a measured rise time of 1.8 ps at room temperature. However, it became apparent that several problems were associated with this design, even at room temperature. Specifically, the signal-to-noise ratio for this geometry was generally much worse than other, more conventional layouts. This may have been due to the double pass geometry, stress birefringence induced by the spring clips used to attach the sampling crystal, or retro-reflections back into the laser cavity. In any event, after *many* attempts, the decision was made to change to a more conventional geometry. However, this design has been adapted recently by Duling, *et al* at IBM who are taking advantage of the gapless structure [28].

5D Femtosecond System

The alternate geometry which was chosen has also been used at room temperature, having a measured rise time of 460 fs [5]. In designing a version for low temperature operation, several design criteria had to be met.

First, the smallest geometry currently available was used. In this design, the switch and sampling crystal were edge-polished until a mating surface was produced with micron uniformity. These were then glued down onto a microscope slide, and surface polished. The resultant structure was so uniform that metal electrodes could be evaporated continuously across the interface. This is shown in Fig. 5D.1.
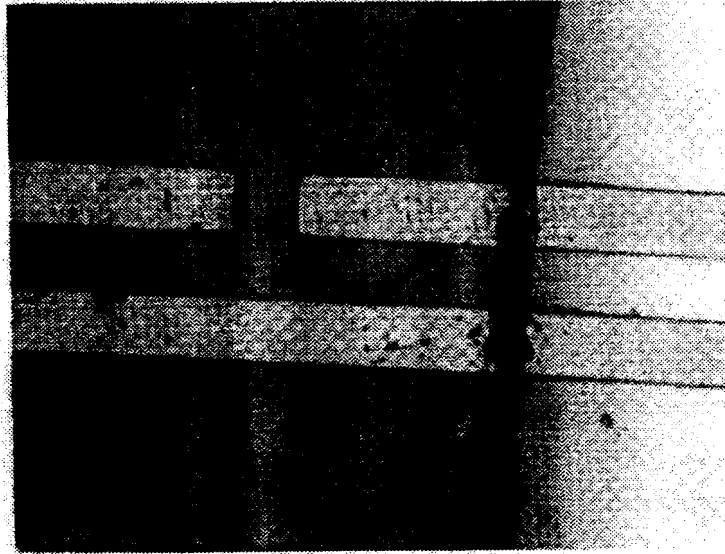
Figure 5D.1 Photomicrograph of integrated structure. Lines are 20 µm spaced

by 20 µm. The gap in the upper conductor forms the photoconductive switch.

The sampling structures were fabricated using photolithographically defined lines and indium metallization. This structure was then characterized using the CPM laser sampler and superfluid helium. The measured rise time of 360 fs is shown in Fig. 5D.2. The jittery nature of the trace is due to the very low time constant used on the lock-in, which was necessitated by the high minimum speed of the optical delay line. In other words, since the translation stage moved so rapidly, the lock-in had to have a very small time constant in order to resolve the rise time.
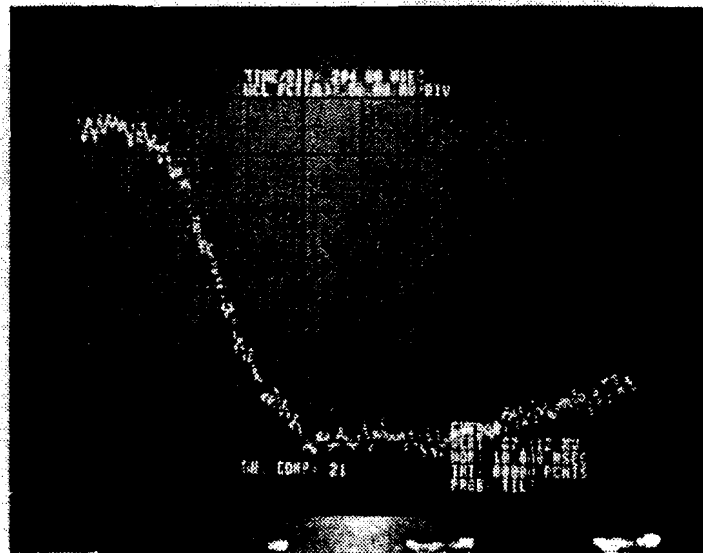
Figure 5D.2 Electrical rise time of 360 fs.

In addition, the rise time was measured as a function of distance. As shown in Fig. 5D.3, the rise time increased to only 2 ps after 3 mm of travel compared to 9 ps after only 2 mm of travel for an equivalent room temperature sampler with gold
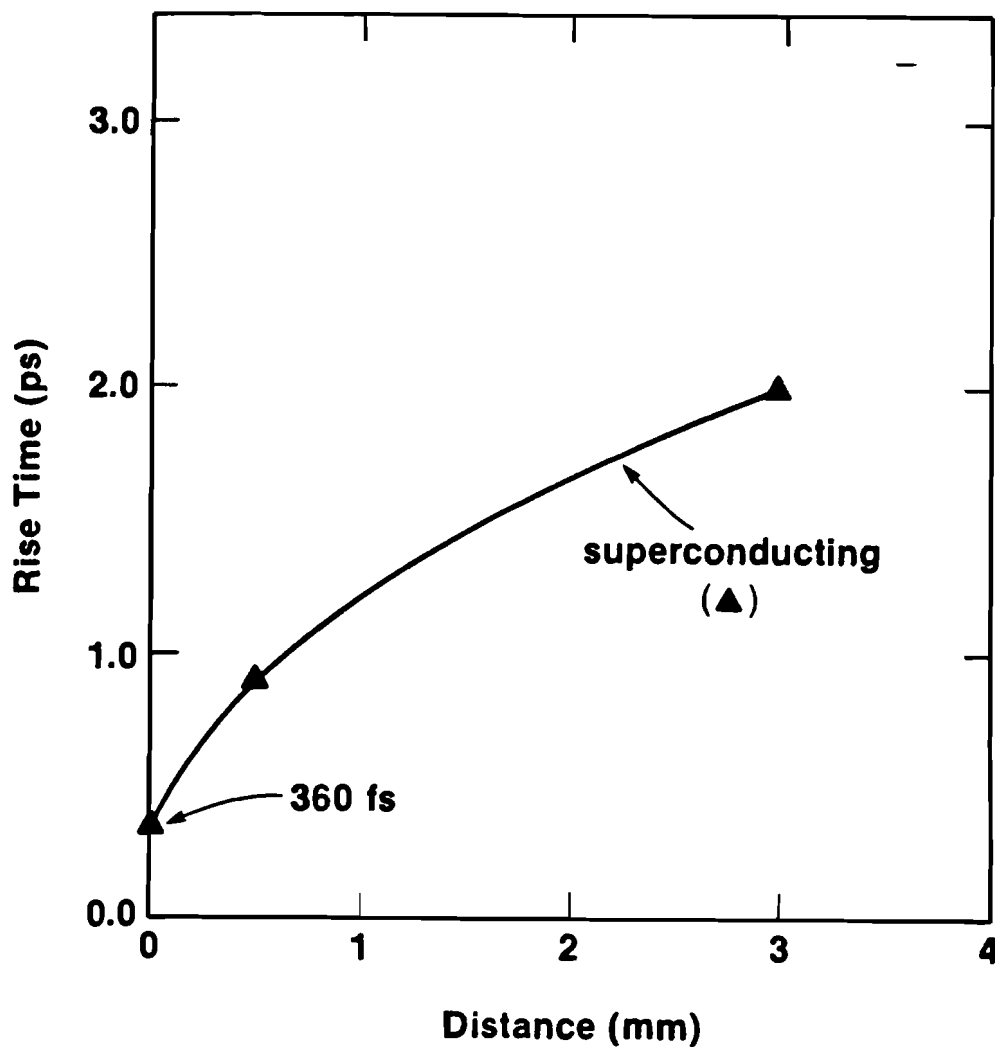
Figure 5D.3 Measured dispersion on superconducting transmission line.

electrodes. These results gave some startling information about the performance of superconducting transmission lines.

Consider the energy gap of indium. This can be related to a frequency by E=hv, which for indium is ≈250 GHz. Clearly, a rise time of 360 fs has frequency

components close to 1 THz. What this means is that frequency components well above the gap frequency are apparently still being conducted. By comparing the superconducting structure to the same geometry with higher conductivity gold electrodes, it is likely that strictly normal electrons are **not** the sole conduction mechanism. A numerical calculation was made to simulate an experimental dispersion curve using only modal dispersion to model the system, and excellent agreement was achieved. A more detailed discussion of these simulations is presented in Chap. 8.

The importance of these results should not be understated. Namely, that superconducting transmission lines can conduct frequencies well above the energy gap frequency means that terahertz frequencies can now be conducted from one device to another with little or no distortion. By using materials and geometries optimized for minimal dispersion, circuits operating in the terahertz regime are clearly feasible. In fact, for a "real" machine with finite propagation distances, the importance of a theoretical "zero rise time" device is overshadowed by the need to propagate that signal from place to place.

6 Cryogenic Results

This chapter opens with a review of the design requirements for the coplanar strip transmission lines used in these experiments.

Next, the cryogenic probe is discussed. While based on an NBS design, the author's version differs significantly in its usage of only one very high speed transmission line to service all the circuits on a given chip. The advantage of this design is a tremendous decrease in the thermal loading of the helium bath by reducing the number of heat pathways to room temperature.

Two sets of experiments are described in this chapter, and they are divided into sections: quasi static experiments (Secs. 6D and E) and integrated experiments (Secs. 6F and G).

In the quasi-static experiments, the sampler and photoconductive switch were both in the room temperature environment. This placed a lower limit on the pulse width that could be delivered to the junction due to the long signal paths into and out of the dewar. These experiments provided a base line against which the integrated experiments could be compared.

For the integrated experiments, the switch, junction and biasing line were all integrated on a single substrate. In addition, the signal path between the switch and the junction was minimized to insure an unprecedented rise-time pulse would be delivered to the junction. The signal path length was in fact smaller than the path length which resulted in the 360 fs rise time reported in the previous chapter. This experiment represented the highest level of integration ever attempted using electro-optic sampling -- at any temperature, and the first time a subpicosecond rise-time pulse had been used as an excitation for a device of any kind at any temperature.

6A Transmission Line Theory

For these experiments coplanar transmission lines were used to facilitate fabrication. In order to maintain a constant 50-ohm impedance through the entire structure, the lines as well as the contact pads were designed for this impedance. A quasi-static analysis was carried out by Wen [29], although this analysis neglects finite substrate thickness.

The characteristic impedance, Z_0, for a transmission line is given by:

$$Z_0 = \frac{1}{Cv_{ph}} \qquad (6A.1)$$

$$\text{where } v_{ph} = \sqrt{\frac{2}{\varepsilon_r + 1}} \, c \qquad (6A.2)$$

In the expression for the phase velocity, v_{ph}, an average value of the dielectric constant is used, assuming an air superstrate, so that $\varepsilon_{eff} = \dfrac{\left[\varepsilon_{r(substrate)} + 1 \right]}{2}$.

For coplanar waveguide the capacitance per unit length is:

$$C = (\varepsilon_r + 1)\varepsilon_0 \frac{2a_1}{b_1} \qquad (6A.3)$$

where a_1 and b_1 are the waveguide dimensions as shown in Fig. 6A.1 (z_1-plane).
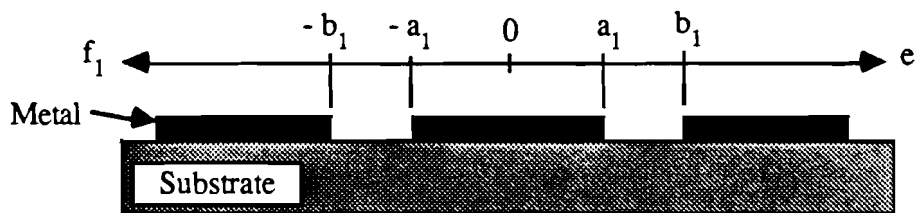
Figure 6A.1 Coplanar waveguide geometry (z_1-plane).

Next, in order to find the characteristic impedance for a coplanar strip transmission line, a conformal transformation is made into a rectangle, such that the dielectric fills the interior. This mapping is shown in Fig. 6A.2 (z-plane).
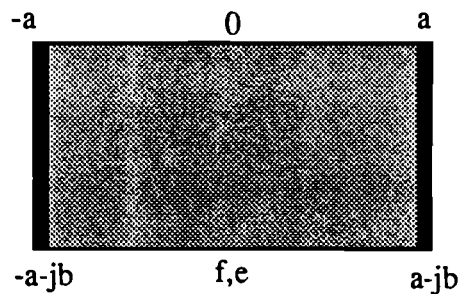
Figure 6A.2 Conformal map into z-plane.

In this mapping, the dielectric interfaces are now on the top and bottom surfaces, and the electrodes are on the sides:

$$\frac{dz}{dz_1} = \frac{A}{\sqrt{z_1^2 - a_1^2} \; \sqrt{z_1^2 - b_1^2}}$$ (6A.4)

where A is a constant. The ratio of a/b can be found by using the integral:

$$a + jb = \int_0^{b_1} \frac{A}{\sqrt{z_1^2 - a_1^2} \; \sqrt{z_1^2 - b_1^2}} \; dz_1$$ (6A.5)

and the following formulae can then be found:

$$a/b = K(k)/K'(k)$$ (6A.6)

where $K(k)$ is the complete elliptic integral of the first kind and:

$$k = a_1/b_1 \quad \text{and} \quad K'(k) = K(k')$$

$$k' = \sqrt{1 - k^2}$$

Substituting these expressions into equations 6A.1-3, the characteristic impedance becomes:

$$Z_0 = \frac{\sqrt{2}}{\sqrt{\varepsilon_r + 1} \, \varepsilon_0 c} \left[\frac{a}{b} \right] \qquad (6A.7)$$

For a given impedance then, the tabulated values of K can be linearly interpolated to yield a value for the line dimensions. As an example, for $Z_0 = 49.82 \, \Omega$; k = 0.037 and $\theta = 2.12°$, K = 1.57137, K' = 4.69405 so that a_1/b_1 = .33476 and and so a/b = 0.038.

For a minimum dimension of $5\mu m = 2a$, then b = $63.29\mu m$. In addition, to fit 5 contact pads on a 1/4 in. chip, pads were chosen to be 47.03 mils wide with corresponding gaps of 3.72 mils. This maintained the 50-ohm impedance through the entire structure.

While this strategy represents an optimization, it should be noted that it is, as stated in the opening paragraph, a quasi-static approach. The reality of a high-speed, broad-bandwidth structure, is that different frequencies will experience different impedances. Furthermore, the abrupt change in dimensions in the transition between the transmission lines and contact pads also represents a violation of the "gradual change" rule of microwave design, namely that changes in structure should be gradual, relative to a wavelength. Despite these shortcomings, this design, along with the probe design discussed in this chapter, proved to be very workable.

6B Sample Design

Devices were constructed at NBS in Boulder, Colorado on two different occasions, and the brief outline given here summarizes the procedure used.

The first devices constructed were subject to several design constraints. As described earlier, the high speed signals were to be routed into and out of the cryogenic environment. This required the entire structure to have as close to 50 ohm impedance as possible to minimize reflections. To accomplish this, everything, including the contact pads, was designed to have 50 ohm impedance. In addition, in order to test any devices at NBS, a particular contact pad pattern had to be used in order to mate to existing NBS probes [30]. Specifically, test devices were fabricated around the perimeter which mated properly to the NBS test probes.

The basic fabrication technology is the IBM lead alloy type [31]. In addition, niobium ground planes were available, and this layer was patterned into a backing layer for the contact pads. The basic layout is shown in Fig. 6A.1.
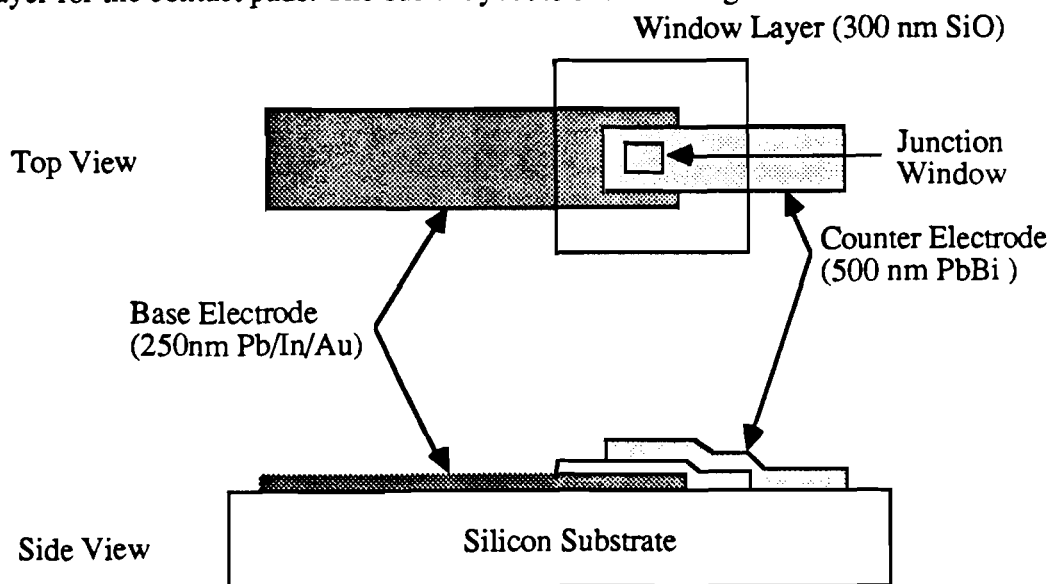
Figure 6A.1 Tunnel Junction Fabrication

Not shown in the figure are the niobium layer and the protective layer of SiO (100nm) that was put on top of the lead bismuth layer. The process had a 5 μm line rule with 0.75 μm runout on all edges. Also, contact between the Pb/In/Au and PbBi layers was not allowed as Bi migration would occur. This required the use of large area "shorting junctions" to be used to make connections to the base electrode layer from the Pb Bi counter electrode.

SiO window layers were used to mask the oxide layer, which was formed by RF oxidation with O_2 pressures varying from 15-20 μm. The junction was defined by the inner square of the window layer shown in Fig. 6A.1. A typical result is shown in Fig. 6A.2.
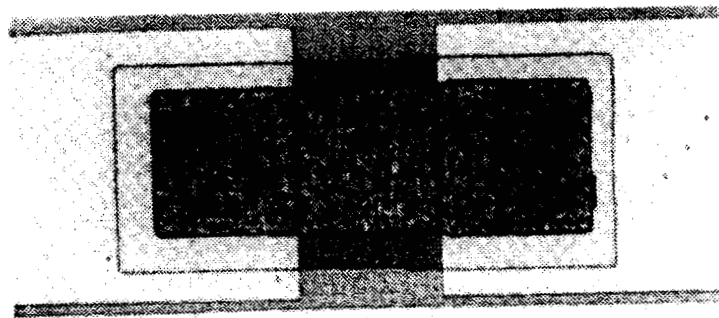
Figure 6A.2 Photomicrograph of transmission line structure. Junction is 10^{-3} cm^2. Shorting junction (right side) is 20% larger.

An I-V curve for a small area test device is shown in Fig 6A.3. The O_2

pressure was 15 μm.
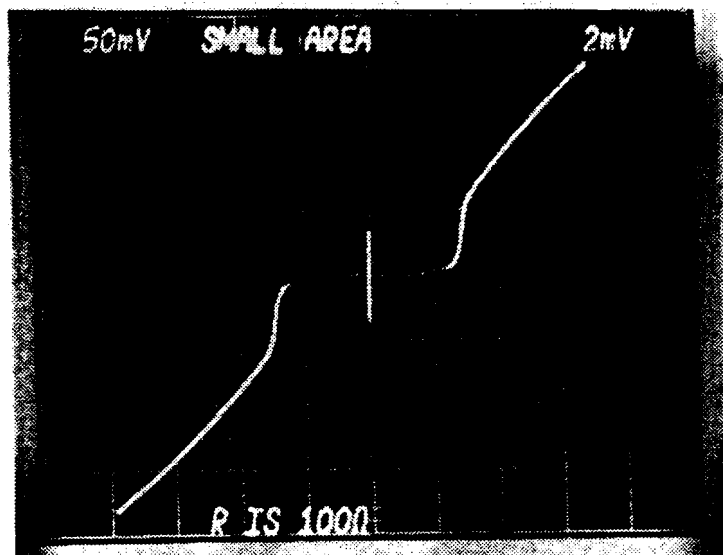
Figure 6A.3 Small area test device tested at NBS showing high quality device

characteristics. Current is 50 mV/100 Ω = 0.5 mA/div.

One of the outstanding features of these devices is their long shelf life. Devices

were tested up to one year after fabrication, and found to to have little or no change in

critical current.

6C Probe Design

The probe for this experiment was based on a design by C.A. Hamilton (Ref. 30) of NBS. This was done for several reasons. First, such a design allowed testing of devices to be accomplished at NBS during the fabrication process. It also allowed easy changing of chips as this was a "drop in" design. Finally, the design could easily be modified to match the design theory presented in this chapter.

Standard circuit board material (G-10) was used as a substrate for the chip carrier. Beryllium copper was used for the metallization, as this material maintains its springiness even at cryogenic temperatures. The lines were fabricated using the same procedures as for the chips themselves, except that the reticles were used as the masks (rather than being reduced on a step and repeat camera for chip use). The layout of the carrier is shown in Fig. 6C.1.
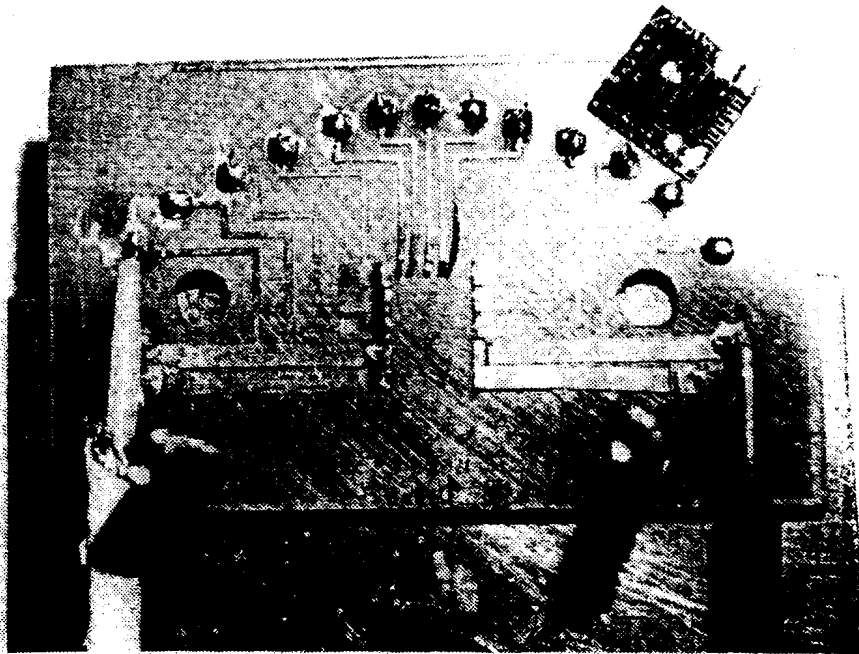
Figure 6C.1 Chip carrier substrate. Chip is 0.25 in. square.

As shown in the figure, only one set of transmission lines was fabricated on the substrate. Since the I/O lines were 0.141 in. semirigid cable, multiple lines would have been an excessive thermal load. Also shown in the figure is a flexible coaxial cable designed to provide a dc bias to the experiment.

The contact pad for each line was formed by lifting the edge of the copper strip, and inserting a small diameter wire beneath it. The strip was then rolled over the wire to produce the contacts shown in the figure. In addition, the indium blob technique was used to enhance the contacts on the chip as shown on the sample in the photograph.

For the chip carrier itself, a novel technique was used which allowed all the transmission lines on the chip to be easily accessed with only one set of I/O lines. This arrangement is shown in Fig. 6C.2.
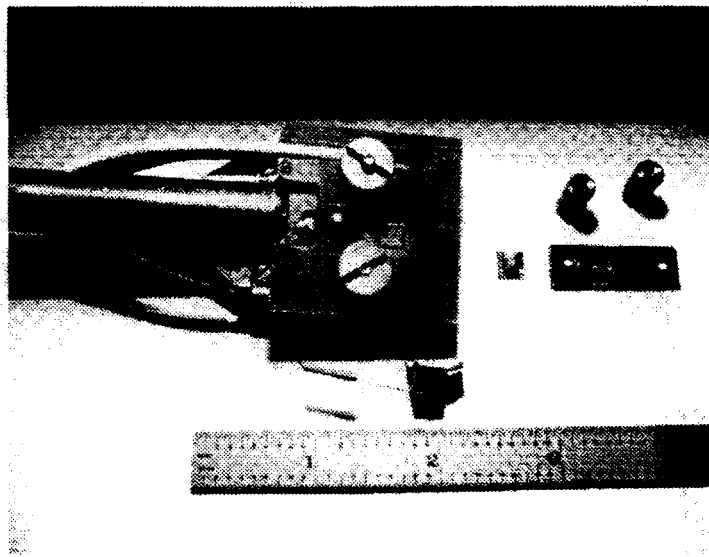
Figure 6C.2 Probe photograph. Parts are described in the text.

As shown in the figure, the two large thumbscrews were used to hold down a movable fiberglass (G-10) chip holder. In this way, the chip holder could be moved relative to the substrate, to allow each of the transmission line structures on the chip to be aligned with the output lines.

After the chip had been positioned, a brass block and Be-Cu spring were placed on the back of the chip to hold it in place. The brass block also contained a small resistor, which was used as a heater to drive trapped flux out of the junction. Behind the brass block was a plate and two threaded cylinders which held the block in place. These are shown in the right side of the photo. The small square is the 0.25 in.^{2} chip.

6D Tunnel Junction Experiments I (Quasi-Static)

Experiments were performed using the electro-optic sampling system, in much

the same way as the single shot experiments described in Chap. 4. Here however, the

repetition rate of the laser (100 MHz) precluded the use of dc biasing, so all dc

information was shorted from the input line by an "inductive short". Although the

short did reduce the signal level, it also completely suppressed the dc. The layout for

this experiment is shown in Fig. 6D.1.
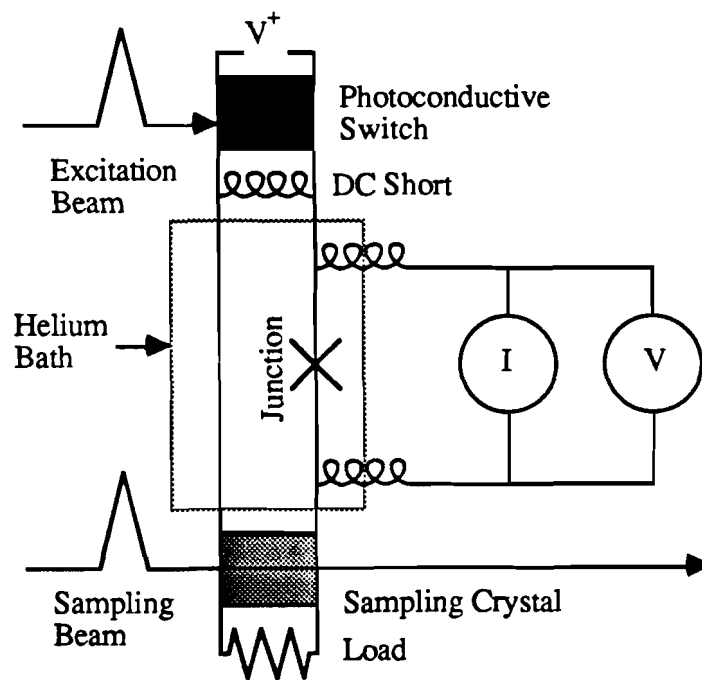
Figure 6D.1 Schematic Layout. Laser and Detection equipment are omitted for clarity.

The signal generation scheme was described in Chap. 4. In this version Fe:InP

photoconductive switches were provided by MIT Lincoln Laboratory [32].

Interdigitated gaps were used which produced efficient switching at the expense of

some speed. These devices were mounted in an alumina microstrip carrier, and so the

charge lines were also constructed in this geometry. Charge lines of various lengths

could be connected and disconnected in a matter of minutes using conductive silver

paint. An actual measured output signal from one of these charge lines is shown in

Fig. 6D.2.
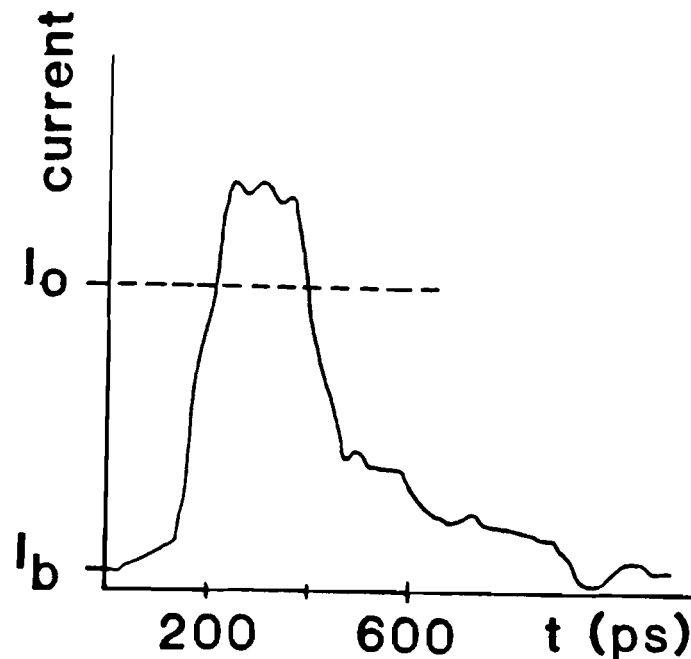
Figure 6D.2 Measured Fe:InP switch output with charge line attached. The slower

portion of the rise time was due to reflections within the sampling crystal.

As shown in the figure, the rise time (80 ps) was limited by the propagation

distance. The detector used for these measurements was a coaxial design and nearly

identical to the one described in Chap. 5.

Switching thresholds were measured directly for these devices by noting the

change in impedance that accompanied a change of state. As shown in Fig. 6D.3, this

change in impedance or reflection coefficient, results in turn in a change in the

measured output voltage. This change in impedance is due to the change of the

junction from the zero-resistance to the finite-resistance state. The results for various

pulse widths are shown in Fig. 6D.4.
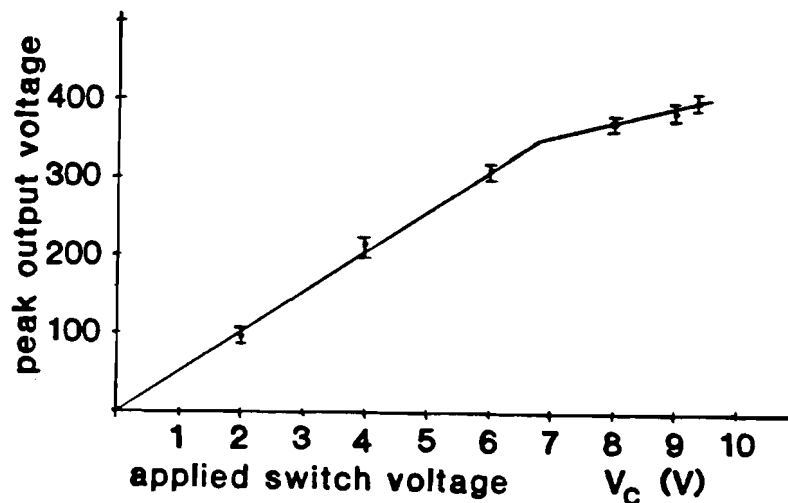
Figure 6D.3 Output voltage as measured with the sampler, versus applied voltage. As

discussed above, the change in slope corresponds to the junction switching threshold.

The straight line behavior in Fig. 6D.4 is a clear indication that the junctions in

this experiment are still behaving in an essentially dc manner. This can be confirmed

by calculating the minimum pulse width for these devices using the model of Dhong

and Van Duzer (Ref. 17). In this model, the minimum pulse width consists of two

parts: a phase rotation time, τ_0, required to drive the phase across the junction by

approximately $\pi/2$, and a rise time, τ_1, required to initiate a nonzero asymptotic dc
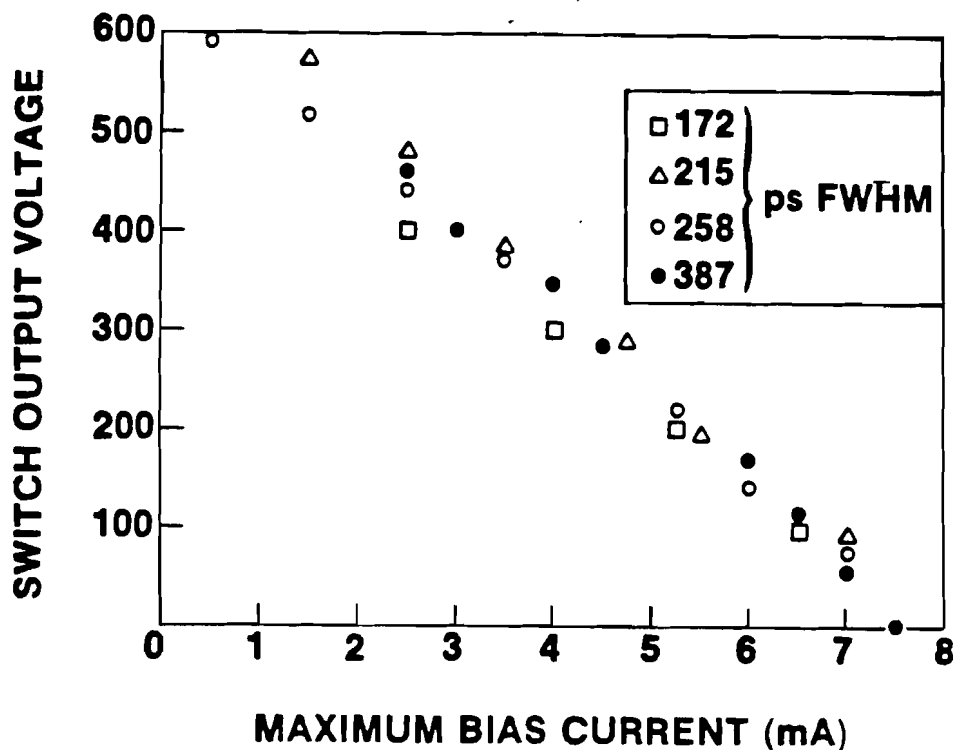
Figure 6D.4 Threshold pulse height plotted versus bias current. The intercepts at both

the vertical and horizontal axes correspond to the dc critical current.

voltage. The term τ_0 is determined by the capacitance and critical current of the

junction. In the pendulum analog, this is the time required for an impulse to push the

bob to just over the first half rotation. In the worst case analysis, where the bias

current, I_b, is zero and the pulse current, I_p, is just equal to the critical current, I_0, and

light junction damping, the minimum pulse width is (see section 4D):

$$\tau_0 = \sqrt{\frac{2C_J\Phi_0}{\pi I_0}}\ \sin^{-1}\sqrt{\frac{\pi I_0}{4I_b}}$$

$$= \sqrt{\frac{\pi C_J \Phi_0}{2 I_0}} \qquad \text{(6D.1)}$$

where C_J and Φ_0 are the junction capacitance and flux quantum respectively.

The rise time, on the other hand, is determined by the time required for the junction to overcome the damping and so it is related to the normal state resistance, R_n. This additional time is:

$$\tau_1 \approx \frac{\Phi}{R_n I_0} \qquad \text{(6D.2)}$$

The total pulse width required is $\tau = \tau_0 + \tau_1$ and for the case where $I_b + I_p \approx I_0$, τ can be estimated using the experimental data of $C_J \approx 50$ pF, $R_n = 0.13 \, \Omega$, and $I_0 = 9$ mA to be approximately 6 ps. Since the shortest pulse available experimentally was ≈ 170 ps, the RSJ model would indicate that the junctions behaved with a threshold essentially that of the dc behavior, as indicated in Fig. 6D.4.

6E Indirect Measurements (I-V)

Using the I-V measurement apparatus, it was possible to measure the I-V curve

for a junction with and without the presence of the high-speed excitation. Essentially,

the junction would mix down the high-speed excitation to the frequency of the curve

tracer (normally tens of hertz). The advantage of this technique is that critical current

values could be directly determined in the presence of the excitation. Figure 6E.1

shows several I-V curves taken under varying levels of excitation.
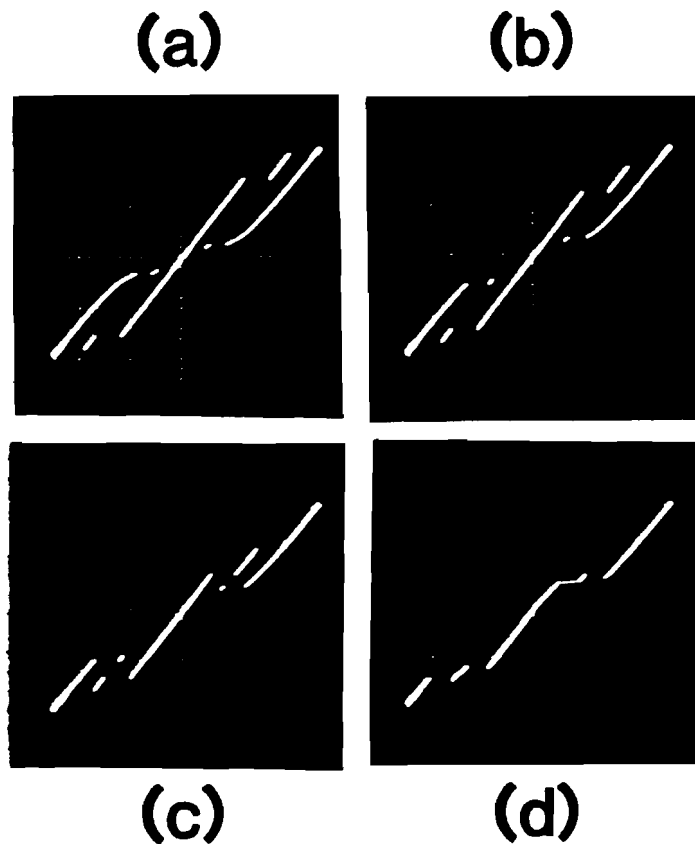
Figure 6E.1 Series of oscillographs showing two wire I-V curves for a number of

increasing pulse heights (a to d), all having the same duration. The vertical scale is 5

mA/div and the horizontal scale is 5 mV/div.

The entire I-V characteristic was slanted due to resistance of the wires used in the two-probe I-V measurements. Two-wire measurements were made to minimize the impact of the tracing apparatus on the high-speed signal paths. In the absence of excitation (Fig. 6E.3a), the I-V curve was that of a high-quality hysteretic tunnel

junction with leakage less than 50 μA. The second switching in these curves was due to the larger (shorting) junction described in Sec. B of this chapter. When current pulses were applied, the entire I-V structure became asymmetrical (Fig. 6E.1b and c). In the direction parallel to the pulsing current the junction switched at a bias less than

I_0. This situation was experimentally found to correspond directly to the impedance change shown in Fig. 6D.3, providing a separate measurement of the switching threshold. Finally, at large pulse amplitudes, the junction stayed in the resistive state, as shown in Fig. 6E.1d.

6F Tunnel Junction Experiments II

—

In order to time resolve the switching event, the integrated geometry of Sec. 5C was adapted to the experiment with new devices fabricated at NBS, Boulder. In this iteration, however, the substrate material was GaAs (undoped), which allowed photoconductive switches to be fabricated in situ. The switch (50 μm gap) was fabricated very close to the junction (about 70 μm). The measured 360-fs rise time discussed in Chap. 5 corresponds to roughly the same propagation distance. The pulse width was controlled by the length of charge line on the chip and for this design was about 10 ps. In addition, an inductive (meander) line (10 μm) for I-V curve characterization was fabricated directly on chip. A photomicrograph of an actual sample is shown in Fig. 6F.1.

The junction output was connected to a 50-Ohm gold coplanar stripline fabricated on the sampling crystal through 18 μm gold wire bonds. In order to minimize the propagation distance, the original output contact pads were cut off, using a dicing saw, and bonds were made directly from the superconducting electrodes to the gold lines. Bonding to the superconducting electrodes proved to be very difficult. The Pb alloy is a soft material and was fabricated in a thin layer on the chip. Much worse however, were the PbBi lines, as these were covered with a protective layer (100 nm) of evaporated SiO. Bonds to this layer were made by ultrasonically "exploding" through the SiO to reach the metal underneath. Very careful examination of Fig. 6F.1 shows the PbBi line to be flared out underneath the wire bond "foot", evidence of the extreme conditions during the bonding event.
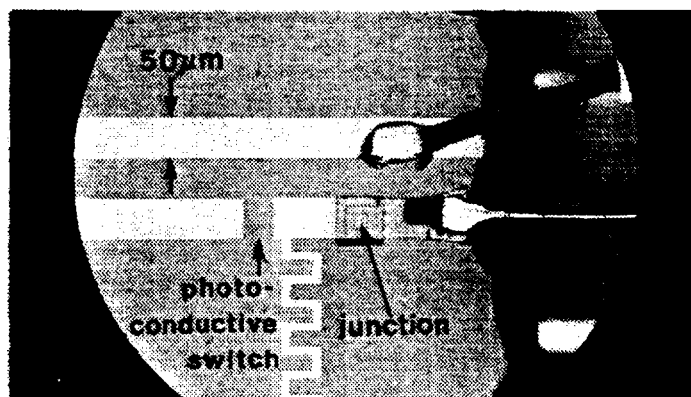
Figure 6F.1 Micrograph of an actual sample. The inner square on the right hand side

of the meander line is a 30 x 30 μm^2 tunnel junction.

Since all the high speed signals were restricted to the immediate vicinity of the

sample, a very simple probe structure was required. Individual chips were wire

bonded using 18 μm gold wire to gold covered alumina pads.

The entire structure was immersed in superfluid helium and operated as

discussed in Chap. 5.

This apparatus was designed to measure the difference in transient waveforms

propagating along the transmission line on the sampling crystal, depending on the state

(zero voltage or resistive) of the junction. The difficulty of this measurement lies in

discriminating the junction response of less than three millivolts from the much larger

excitation pulse. In addition to the excitation pulse there are various reflections and

radiated signals from the photoconductive switch. These reflections limited the useful

temporal window to the arrival of the first major reflection. For the geometry used here, the first major reflection is launched by the GaAs/LiTaO$_3$ discontinuity. This reflected wave then propagates backwards through the circuit and reflects again off the second discontinuity: the large input contact pads (not shown in Fig. 6F.1) at the end of the sample. The time required for this signal to propagate twice across the GaAs chip is at least 30 ps. This value gives a reflection-free temporal window for time-domain measurements. Direct time-domain measurements were then made for different dc bias conditions. One such data set is shown in Fig.6F.2. The top waveform in the figure was measured with the junction biased in the linear resistive

3.4 ps
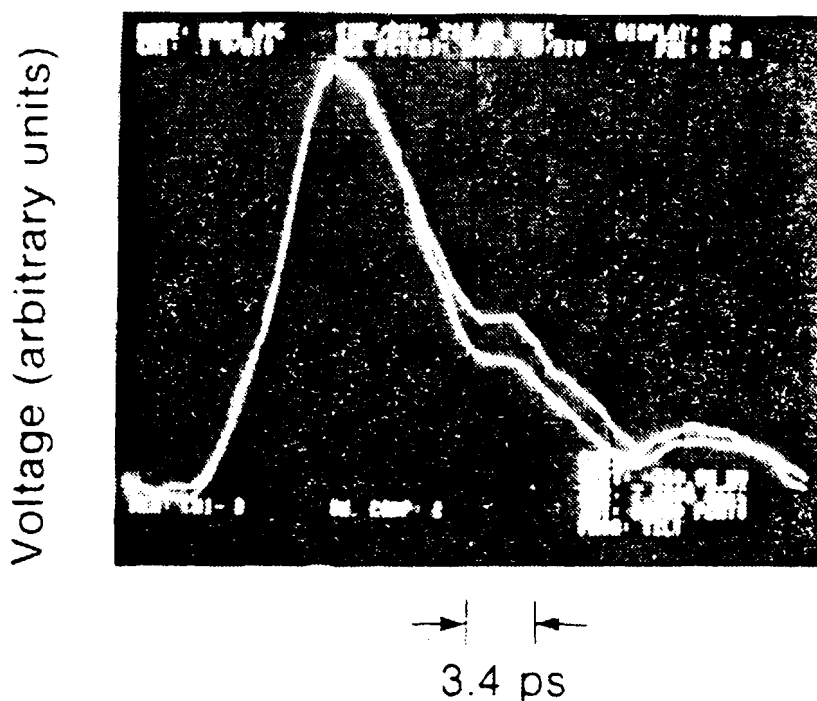
Figure 6F.2 Junction voltage waveforms. Upper curve corresponds to the "no junction" condition in the transmission line, and the lower curve is the unbiased junction response.

state, while the bottom curve corresponds to the dc unbiased junction. In both cases, the input pulse amplitude remained the same. It is important to note that high, positive dc bias is equivalent to a "no junction" condition in the transmission line, as the junction exhibits strictly resistive behavior in this regime. In addition, the junction could be driven into the normal state by illuminating it with laser light. This was accomplished using a small fraction (few mW) of the cw argon ion laser pump, which emits at 514.5 nm. The apparent contradiction of a normal state junction in a superfluid helium bath may be explained by the fact that the PbBi counter electrode was insulated from the superfluid by the SiO protective layer. This latter technique turned out to be equivalent to the high bias condition -- the measured waveforms remained the same in both cases.

The results of Fig. 6F.2 clearly indicate that the junction switching transient is a small perturbation compared to the total measured signal. The bottom waveform in Fig. 6F.2 shows that the signal experienced a reflection during the early stages of propagation. This is the only portion of the waveform clearly attributable to the junction switching from the zero-voltage to the nonzero-voltage state. It therefore appears that the junction starts to respond when the input pulse reaches its maximum, and the full voltage across the junction is developed at the time corresponding to the input pulse duration. No significant delay is present in the junction response.

Based on these measurements, the response time of the junction was at most 12 ps, but it should be noted that virtually all the dispersion evident in Fig. 6F.2 was incurred after the pulse had passed through the junction. As mentioned earlier, the distance from the switch to the junction is only 70 μm, while the sampling point was several hundred micrometers further away, most of the distance being in the much more dispersive LiTaO$_3$ sampling crystal.

6G Indirect Measurement (Chaos)

In this section, as in Sec. 6E, the technique of measuring the high speed behavior through the use of the I-V curve is presented. Here, as in the previous section, the extreme speed of the system enables new phenomena to be measured.

The I-V characteristics are those of the junction of Fig. 6F.1. The I-V curves are shown are in Fig. 6G.1 for 8 levels of incident excitation. Although these are two wire measurements, a differential output from the I-V driver allowed corrected curves to be measured. In Fig. 6G.1a, for small input pulses, only the critical current on the positive branch was reduced (here "positive" is defined as the polarity of the excitation signal). The negative branch was virtually unchanged (there was only a small decrease in the value of the critical current). When the input pulse amplitude was increased to just compensate the positive branch of the critical current (i.e. reduce the critical current to zero on the I-V tracer), a switch bias of 1.2 V was required. For current pulses above this threshold, (Figs. 6G.1c - f) "noisy" (i.e. chaotic) behavior set in on the negative branch, while the positive branch retained the typical quasiparticle tunneling curve described in Chap. 3. Figures 6G.1c and d represent a situation where the input pulse amplitude was too small to completely compensate the negative branch of the critical current. In this instance (Fig. 6G.1d) the junction displayed a novel "reentrance" process in which, with an increasing level of bias, the junction switched from the oscillatory regime back to the stable, zero-voltage state. Finally, note that the chaotic behavior was possible only for bias currents less than the critical current. For larger bias, the junction always remained in the stable finite-voltage state.
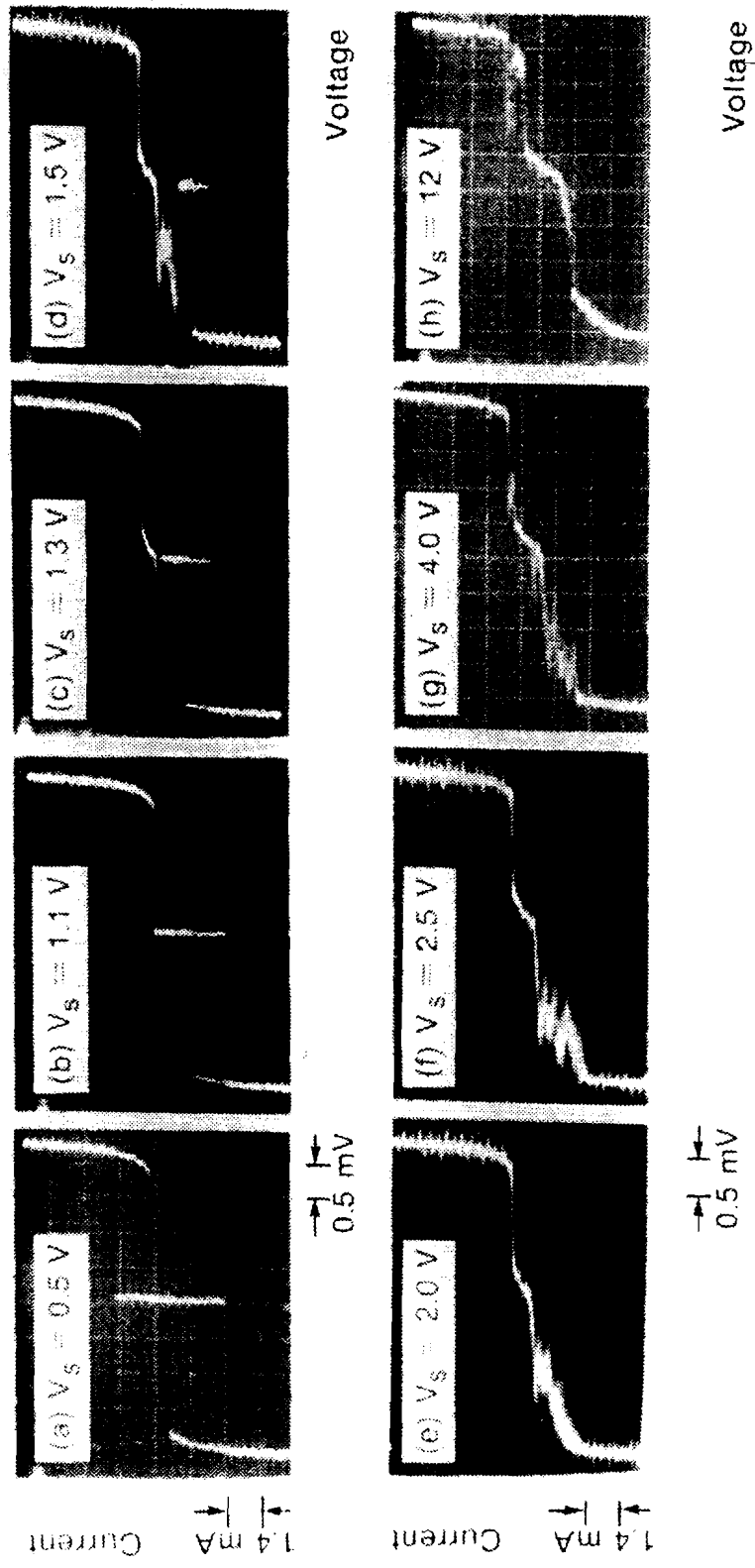
Figure 6G.1 Experimental I-V curves for eight different values of the amplitude of the input pulse. The small noise signal present on the gap-voltage section of the quasiparticle I-V curves is due to the 60 A laser power supply noise which was then picked up by the oscilloscope outside the cryostat. All measurements were preceded by a 1-MHz low pass filter.

At very high values of the applied pulse (Figs. 6G.1g and h), chaotic behavior also appeared on the positive branch of the I-V curve. At the time of the measurements, the data were clearly exhibiting new phenomena, although it was not until simulations were performed and the oscillatory behavior was reproduced that a strong case for chaos in these junctions could be made. However, it was immediately noted that the gap voltages and quasiparticle structure of the junctions remained the same as for the unperturbed junction. This implied that the entire behavior must be associated with the junction itself, as the dc superconducting characteristics remained unchanged. These results are presented in the next chapter. The absence of chaos on the positive branch in simulations, suggests that the chaos evident in Fig. 6G.1g and h is in fact due to reflections (negative) in the experimental apparatus. Reflections of this type are typical and occur at any discontinuity (such as contact pads) in the transmission line structure.

Numerical Simulations

The data of the previous chapter were taken under different experimental conditions than those for which previous simulations were done. This required a new set of simulations to be performed which took the actual conditions into account.

These simulations are therefore the first to show chaos in a periodically kicked Josephson junction. In addition, the origin of the chaotic behavior was traced to the sensitivity of the model to the rise time of the excitation pulse. This led the author to introduce the concept of a critical rise time, which gives another parameter to use in characterizing tunnel junctions in the picosecond-pulse regime.

7A JSPICE Simulations

Numerical simulations of Josephson logic gate switching, based on the RCSJ model, have been extensively studied, mostly at NBS Boulder [33] and at the University of California, Berkeley [17]. Their studies covered a single junction gate as well as multiple junction interferometers. The bulk of the results were obtained for small overdrive (above the junction critical current) with rectangular, or step function pulses, suitable for studying threshold switching and the corresponding turn-on delay and rise time.

In the case of the chaos studies, however, the junction is in an unbiased condition, and is excited by a stepped, picosecond input pulse. The RCSJ model for this case, with no load conductance is:

$$C_J \frac{dV(t)}{dt} + \frac{1}{R_J} V(t) + I_C \sin\phi = I(t) \qquad (7A.1)$$

where $V(t)$ is the time dependent voltage across the junction, C_J is the junction capacitance, R_J is the voltage dependent shunting resistance (it models the quasi-particle characteristics) , I_C and ϕ are critical current and phase across the junction, respectively. Following the experimental situation, it is assumed that $I(t)$ is a high amplitude, picosecond pulse, characterized by a subpicosecond rise time and total duration t_p -- a slightly simplified version of the original pulse presented in Sec. 5D.

The transient numerical calculations are based on Eq. (7A.1) and implemented using the JSPICE circuit simulation program [34], for the device parameters corresponding to the measured junctions.

The model used in the original JSPICE program is based on the piecewise linear

approximation shown in Fig. 7A.1. The variable DELV is the gap transition voltage, which is 0.1 mV for these simulations. The more realistic model shown in Fig. 7A.2, is the model actually used in this study and corresponds more closely to the measured I-V curves shown elsewhere.
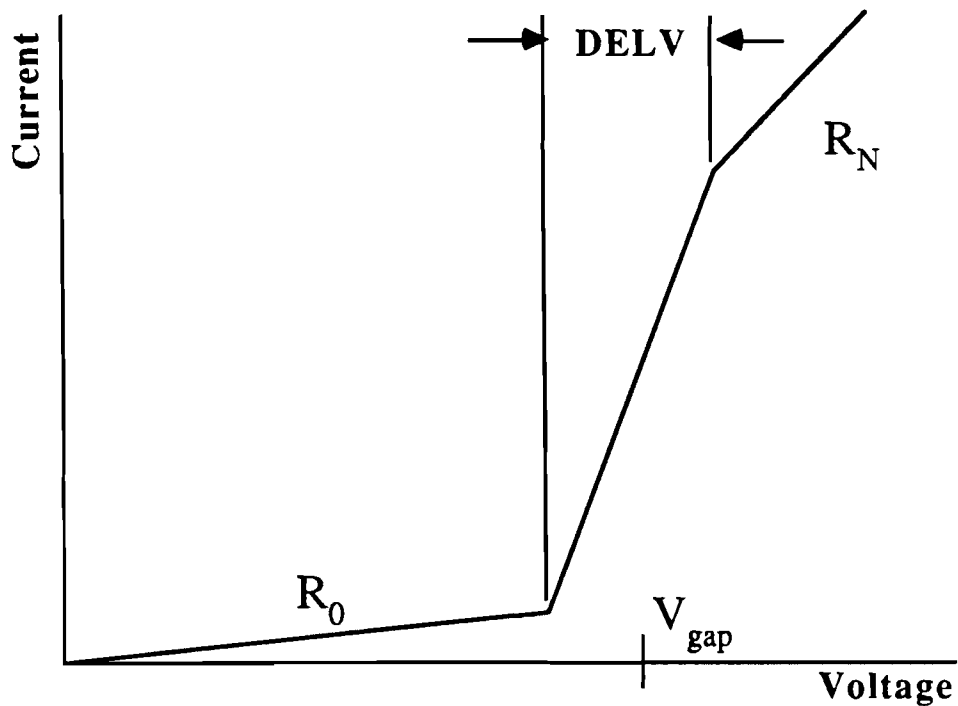
Figure 7A.1 Basic I-V curve used in JSPICE simulations.

In this model a Fermi-like weighting function is used for values of the resistance between R_0 and R_N:

$$I(V) = V \frac{G_0 + G_N \exp(\gamma)}{1 + \exp(\gamma)} \qquad (7A.2)$$

$$\gamma = (|V| - V_{gap})/DELV \qquad (7A.3)$$

where $G_0 = 1/R_0$ and $G_N = 1/R_N$. The transition region is about six times as wide as

the piecewise linear model. The smoothed model is shown in Fig. 7A.2.
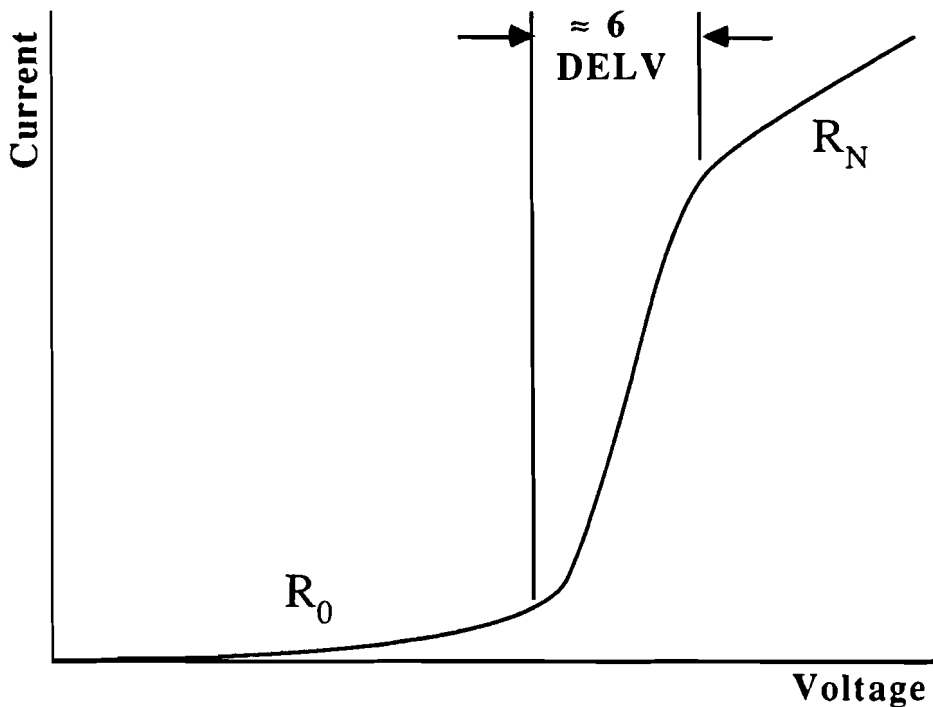
Figure 7A.2. Smoothed I-V curve used in JSPICE simulations.

The simulations presented here were run on a DEC VAX 11/750. They were performed under the control of a high-level DEC command language (DCL), which took care of updating the various parameters which were then passed to the JSPICE program, written in Fortran. Although the DCL program was slow to execute, it allowed the updating of the JSPICE data file as well as writing output files suitable for plotting routines such as the RS1 plotting package, while at the same time updating and testing the parameters used in the JSPICE simulations. In addition to the main control program, several other subroutines were written which performed the specific file manipulations such as updating a particular variable in a Fortran data file. The programs are listed in the Appendix, along with the various subroutines.

Basically, the program functioned as follows. After setting all the initial conditions, and creating output files, the JSPICE program is called and executed. The program then read each line of output which contained the calculated voltage value for that time step. The sign of the voltage value was then extracted from the voltage, and if the sign is negative, a no switch condition is inferred.

At this point, it is important to consider the conditions of the simulation. First remember that the window in which the simulation is run is finite. This means that even a subcritical current pulse can result in a switching event if the junction stays in the voltage state beyond the time window chosen. For the purposes of simulation, a switching event was defined as a positive value of the voltage which does not go negative anytime during the simulation.

Next, the program either increments the value of the pulse duration, or returns to the previous value and changes step size, depending on the result of the test for a switching event. The program loops on pulse duration until the convergence criterion is met, and then loops on pulse amplitude until the threshold curve has been mapped out.

The results of several simulation runs are shown in Fig. 7A.3. For these simulations the measured junction values of: $C_j = 16$ pF, $I_c = 2.0$ mA, $R_n = 1$ Ω, and $R_0 = 32$ Ω were used. The calculated RC time constant, τ_{RC}, is then 512 ps. This is clearly reflected in the figure. For values of the time window, $w \ll \tau_{RC}$, the results do not change very much with the value of w: the simulations for $w = 20$ ps and $w = 100$ ps were essentially the same. In addition, the asymptotic value of the minimum amplitude current pulse is significantly less than the dc value of the critical current.

Figure 7A.3 JSPICE simulations for the experimental junction
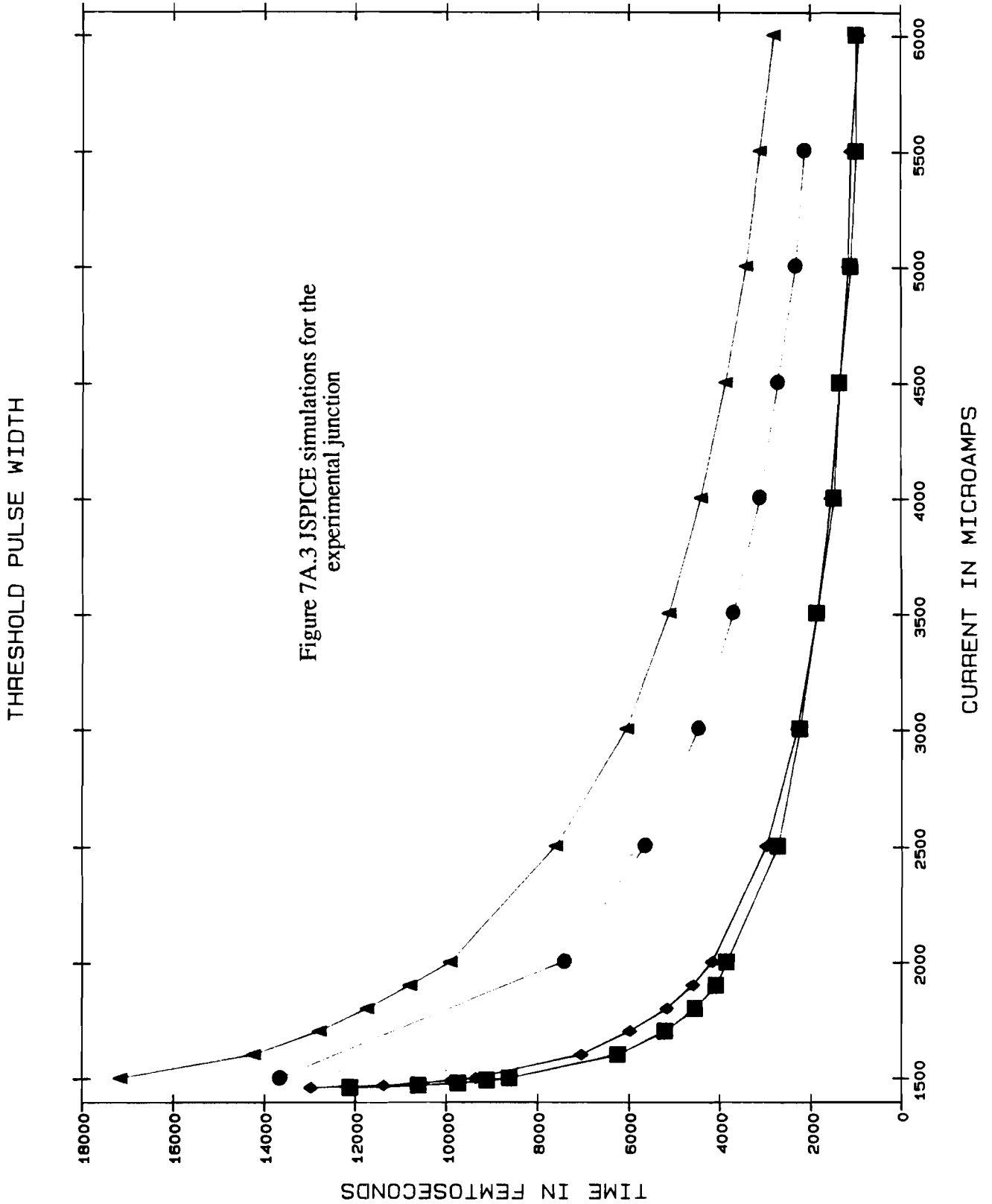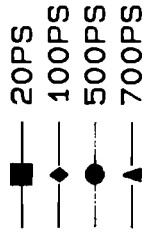
None of the results, even for $w > \tau_{RC}$ approached the dc value of the critical

current. Clearly for $w \Rightarrow \infty$, the results should approach the dc value, however

simulations were not run for $w \gg \tau_{RC}$ due to the long computation times required:

the run time for $w = 700$ ps was more than 15 hours (in batch mode).

These results indicate that the junction used in these experiments was very

different than the simulated junctions of Refs. [17] and [33]. In those simulations, the

excitation pulse was on the order of the RC time constant, and so the response of the

junction was very sensitive to the actual pulse dynamics. In this case, the RC time

constant is so long, that the pulse has come and gone before the junction has time to

react.

It is for this reason that the total charge in the pulse which is delivered to the

junction is the critical parameter. This same line of reasoning says that the exact shape

of the pulse is unimportant, as long the the area underneath the envelope (charge) is

known.

7B Introduction To Chaos

It has been shown in recent years that many simple nonlinear systems, whose dynamics are described by deterministic equations of motion, can show chaotic behavior [35],[36]. Among these systems, Josephson junctions have received much attention, because they (along with lasers) represent a small class of dissipative quantum systems that exhibit deterministic chaos.

Josephson junctions have been simulated for the case of rf excitation [37]-[38], which has an extensive historical precedent as Josephson junctions have been used as rf detectors much longer than they have been thought of as digital switching elements.

Mathematically Eq. 3C.2 can be modified to include the periodic kicks of amplitude, I_p, duration, t_p, and repetition rate $1/T$ ($t_p \ll T$) to give the form:

$$\ddot{\phi} + \Gamma\dot{\phi} = -K\sin\phi \sum_{n=0}^{\infty}\left[\Theta(\tau - nT) - \Theta(\tau - \tau_p - nT)\right] \qquad (7B.1)$$

where the normalized time $\tau = \omega_0 t$, and $\omega_0 = (2eI_0/\hbar C)^{1/2}$, $K = I_p/I_0$, $\Gamma = 1/\omega_0 RC$, with I_0, C and R corresponding to the junction critical current, capacitance and voltage-dependent shunting resistance.

In order to rewrite Eq. 7B.1 as a system of first-order nonlinear independent difference equations, the substitution $v = d\phi/d\tau$ (v is in units of $I_0 R$) is made. These can be reduced to a two-dimensional map for ϕ and v:

$$(\phi_n, v_n) = \lim_{\varepsilon \Rightarrow 0}\left[\phi(nT - \varepsilon), v(nT - \varepsilon)\right] \qquad (7B.2)$$

under the assumption that $\sin\phi(\tau)$ does not change during the applied excitation.

The resulting map is:

$$v_{n+1} = \exp\left[-\Gamma T\right]\left[v_n - \frac{\exp\left[\Gamma\tau_p\right] - 1}{\Gamma}K\sin(\phi_n)\right] \qquad (7B.3)$$

$$\phi_{n+1} = \phi_n + \frac{1 - \exp\left[-\Gamma T\right]}{\Gamma}\left[v_n - \frac{\exp\left[\Gamma\tau_p\right] - 1}{\Gamma}K\sin(\phi_n)\right] \qquad (7B.4)$$

For an undamped ($\Gamma \Rightarrow 0$) junction, Eqs. 7B.3 and 4 can be reduced to a modified Chirikov map [39]:

$$v_{n+1} = v_n - K\tau \sin(\phi_n) \qquad (7B.5)$$

$$\phi_{n+1} = \phi_n + Tv_{n+1} \qquad (7B.6)$$

For these equations, the resulting dynamics have been studied extensively, including routes to chaos, types of intermittent behavior, and models using phase-locked loops.

However there are two distinct differences between the actual experiment and the Chirikov model. First, $\Gamma \neq 0$ so that the simple Chirikov map cannot be used.

In addition, the applied excitation is not a single frequency sinusoid, but a current pulse such that $\tau_p \ll 1/\Gamma$. That is, the pulse width is less than the plasma frequency of the junction and contains a broad spectrum of frequencies.

Due to the lack of a simple model to simulate the junction behavior, a computer program is presented in the next section that was used to simulate the junction using the full equations of motion.

Additional insight into the chaotic behavior can be obtained by computing the

real time junction dynamics, illustrated in Fig. 7B.1. For the simulations presented here, the electrical pulse duration was 8 ps, and the repetition rate was 600 ps. The repetition rate rate is not critical, as long as it is longer than the RC time constant of the junction, which was 460 ps using the subgap value of the resistance and 10 ps for the normal state value. The normalized bias and pulse currents are $i_b = -0.18$ and $i_p = 2.0$ respectively; other parameters are the same as in the previous section. Note that the excitation pulses have widths too short to be discerned in the figure.

In the example presented, the amplitude of the input pulse train was high enough to sweep the bias point temporarily into the positive value voltage state. The pulse repetition rate was long enough that the voltage across the junction had returned to one of the two equilibrium values, zero or the gap voltage, depending on the instantaneous phase value at the moment of the kick. Note that the bias is applied at $t = 0$ along with the first pulse, so the response due to the first pulse should be ignored.

To see how the nature of the pulse affects the dynamics of the junction behavior, consider the same simulation, but with longer rise-time pulses substituted for the short ones (10 ps versus 0.1 ps). In this case, the onset of the pulse is not instantaneous with respect to the evolution of the phase, and so the exact time of arrival of the pulse becomes less distinct. The result is that the junction loses its sensitivity to the pulse arrival time as shown in Fig. 7B.2. All values are identical to those in Fig. 7B.1 except for the longer rise time. Here, the first two pulses were required to set the junction into the negative voltage state.

From these studies it seems that an additional parameter that affects the junction switching threshold is the rise time of the excitation pulse. In fact, it appears that the rise time is an important parameter, as the rise time in Fig. 7B.2 was increased by a factor of ten without decreasing the pulse area proportionately.
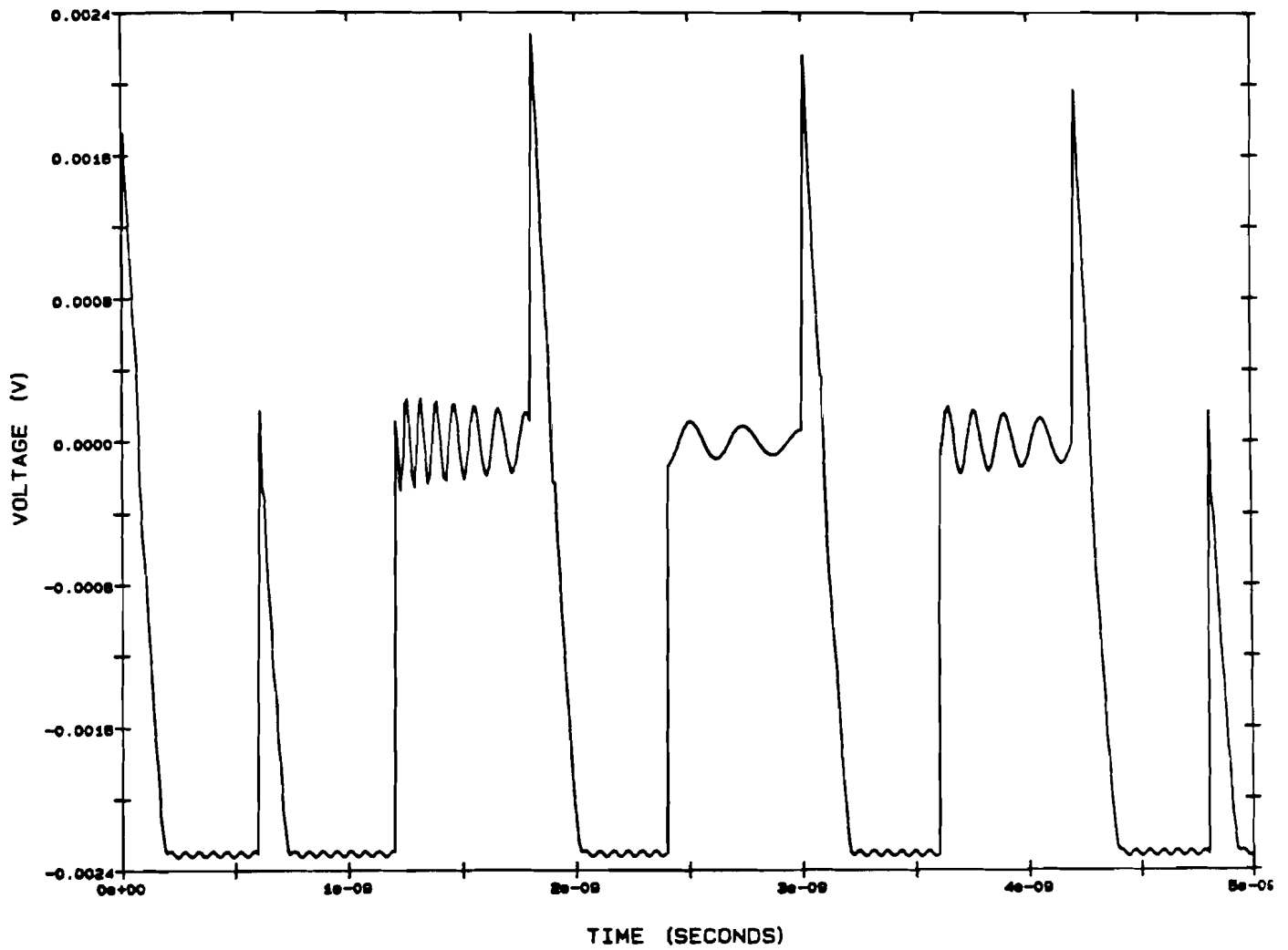
Figure 7B.1 Numerical simulations of the voltage evolution for the first several pulses

applied to the junction (Rise time = 0.1 ps).
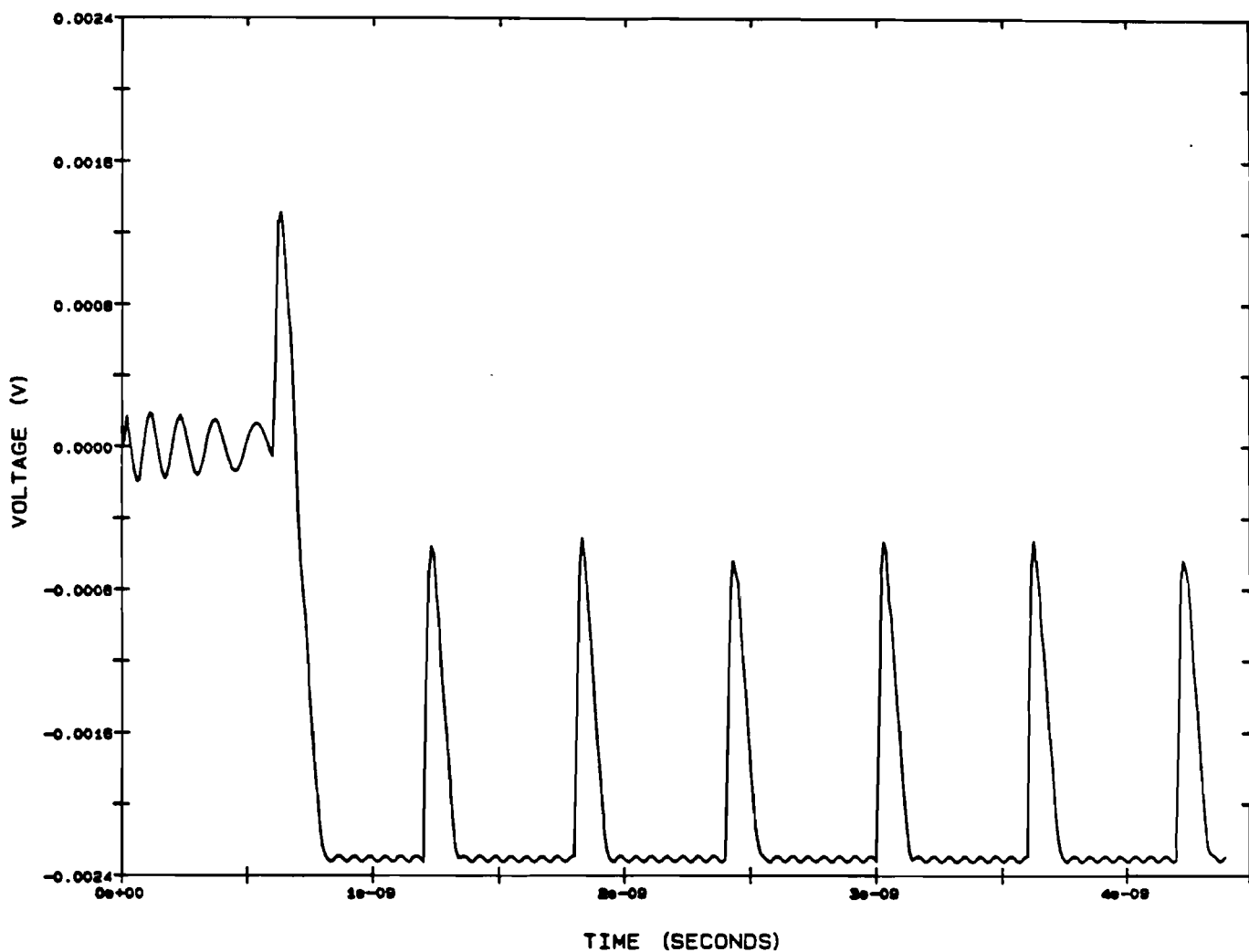
Figure 7B.2 Numerical simulations of the voltage evolution for the first several pulses

applied to the junction (Rise time = 10 ps).

7C Numerical I-V Simulations

Simulations of the data presented in Sec. 6G were performed at IBM Yorktown Heights, in collaboration with C.-C. Chi and C. Vanneste. They were performed on an IBM mainframe computer and consumed as much as ten hours of CPU time per run. The reason for the long computation times was the same as for those in the Sec. 7A, namely that the time scale of the electrical excitation is 0.1 ps, while the repetition rate of the laser is nanoseconds. The form of the equation solved was the same as in the previous section; Eq. 7B.1. Here, however, a time average was performed to yield a point on the I-V curve.

For these simulations, the quantitative correspondence between experimental and numerical results was obtained by using the junction parameters and the shape of the driving pulse current pulses extracted directly from the experimental data. The only fitting parameter was the pulse amplitude at the threshold of complete suppression of the positive critical current, I_0. The experimental threshold value of the **voltage** V_s = 1.2 V was fitted to the numerical threshold **current** of $I_p = 0.82\ I_0$.

The simulated I-V characteristics for several values of normalized current are presented in Fig. 7C.1. The junction parameters are I_0 = 2.75 ma, and ω_0 = 725 GHz. At a pulse value slightly above the threshold (Fig. 7C.1a - corresponding to a switch voltage of 1.4 V, somewhere between the values of Fig. 6G.1c and 6G.1d), two stable solutions exist on the negative branch. Figures 7C.1b and c correspond almost directly to the experimental situation shown in Fig. 6G.1e and f. Chaotic behavior is present on the negative branch, while the positive part of the I-V curve represents the quasiparticle branch. One phenomenon which is absent in the
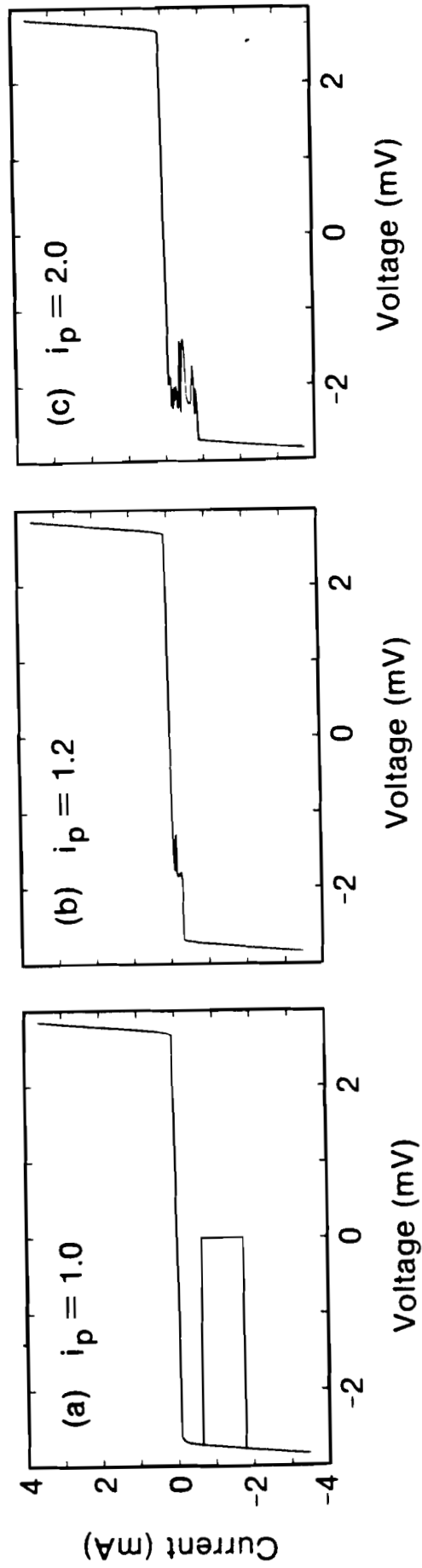
Figure 7C.1 Simulated I-V Characteristics for three different values of normalized amplitude of the input pulse.

simulated results is the reentrant behavior shown in Fig. 6G.1d. However, simulation did show that such behavior is possible if there are substantial fluctuations in the value of the applied current pulse (40% or more around the mean value), which are much larger than the short term fluctuations in the CPM laser. It is possible that long-term fluctuations or additional variations due to reflections of the current pulse may be responsible for the reentrant behavior. The increase in $<v>_{min}$ in Figs. 7C.1b and c also suggests that the reentrance may be due to excitation of self-resonant modes.

The experimental results of Chap. 6 and the numerical results presented here can be summarized by introducing a threshold curve which describes the dependence of the maximum zero-voltage dc current on pulse amplitude, for a given shape of the input pulse. This is shown in Fig. 7C.2. The area inside the solid line corresponds to the stable zero-voltage state. There is remarkable agreement between the experimental points and the simulated (solid) line. The solid vertical lines correspond to the stable region on the negative branch of I_0 in Figs. 6G.1c and d. The three regions are indicated: stable (region I in Fig. 7C.2), chaotic (III), as well as an intermediate region (II) where both solutions are allowed.

It is important to note that the corresponding numerical value of $I_p = 0.82\ I_0$ for the threshold of switching an unbiased junction is **less** than I_0. In fact the entire threshold curve in Fig. 7C.2 deviates significantly from a straight line dependence (dashed line) for the static limit [33], [40], where the chaotic behavior was not observed. As was discussed in Sec. 7A, when the pulse width is comparable $1/\omega_0$, where ω_0 is the plasma frequency, the critical current is no longer a single threshold
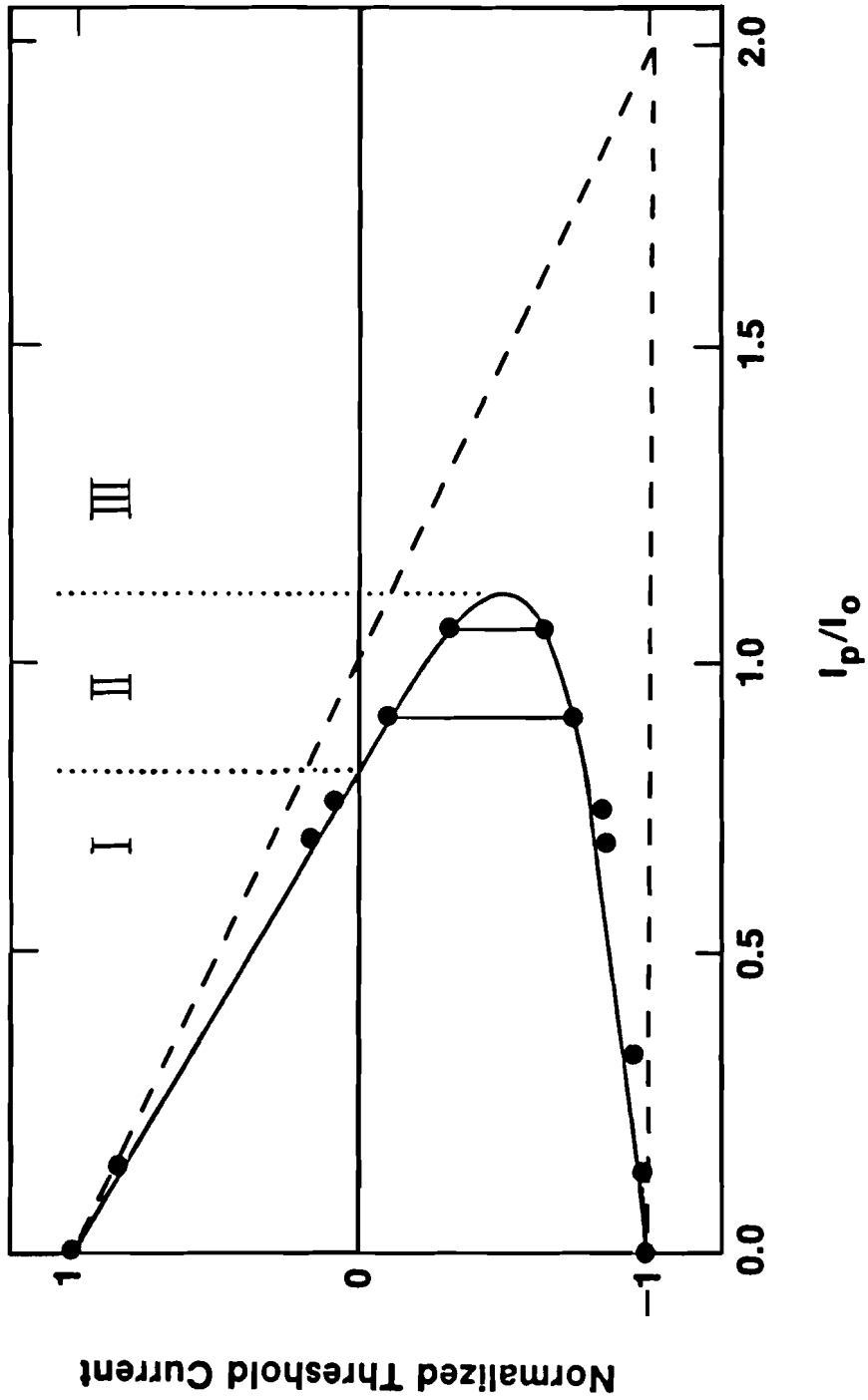
Figure 7C.2. Threshold current dependence on the normalized amplitude of the picosecond input pulse. The dashed line is the linear (static) limit.

parameter, and should be replaced by the new parameter "pulse charge" defined by the

time integral of the threshold current pulse and proportional to I_0/ω_0. In addition, the

rise time must also be included in considering the threshold of a given junction. This

approach differs from previous numerical studies and merits further study.

Finally, it should be noted that the frequency of the kicks was very much less

than was thought to be required (to induce chaos) previously [41], although

periodicities less than ω_0 have been predicted as being capable of resulting in chaotic

behavior [37].

8 Work In Progress

This chapter presents ongoing studies in new areas which have grown out of this work. The cryogenic sampling techniques developed for these experiments have been used to study other phenomena such as low-temperature spectroscopy and dispersion in superconducting transmission lines. In addition, new geometries are being investigated which hold the potential for even better sensitivity to the small voltage changes which occur in Josephson junction switching.

Also included is a study performed on a room-temperature device which is among the fastest now available; and it is presented as a comparison to superconducting technology.

8A Alternative Sampling Geometries

Another geometry used in the course of this work was the side-sampler or "voltmeter" configuration [42]. As shown in Chap. 6, the straight-through geometry was insensitive to the reaction of the junction, since this small change in signal was superimposed on a large feedthrough signal. In order to overcome this problem the geometry of Fig 8A.1 was used.
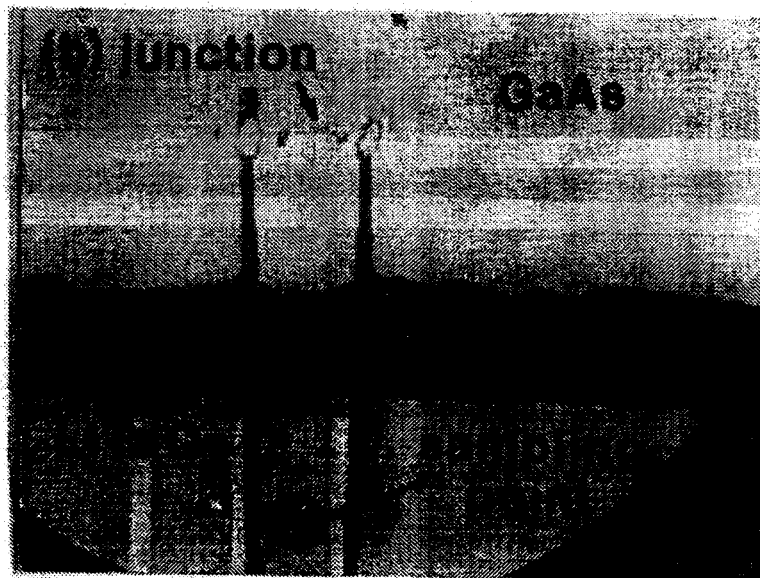
Figure 8A.1 Side-sampling geometry.

This geometry offers the potential to be insensitive to the large feedthrough signal, as only the voltage drop across the junction should result in a signal being launched in the tranmission line. Early results indicate however, that other signals are still present. In addition to the intended signal, the transmission line acts as an antenna

for signals radiated from the nearby circuit. More important than that is the radiated

signal from the dipole which is created in the switch gap. This signal radiates in all

directions, and is sensed in the bulk sampling crystal by the sampling beam as it

traverses the length of the crystal. The signal is integrated during an interaction length,

which for the typical 1/2 mm crystal can be many times the integration length of the

signal in the region of the transmission line.

To reduce the effect of the radiated dipole, several changes were made. As

shown in Fig. 8A1, the wire bonds leading to the sampling crystal cross over the

ground line. In addition, the sampling point was moved away from the radiation point,

in the hope that the radiated signal would fall off faster than the guided one. To further

reduce the radiated signal strength, a grounded piece of gold foil was inserted between

the GaAs substrate and the sampling crystal. Finally the sampling crystal was replaced

by a crystal which was only some 50 μm thick. This reduced the interaction length of

the radiated signal with the sampling beam, while leaving the guided signal unaffected.

After all of these changes were made, the radiated signal persisted, although

much reduced in magnitude. The difficulty in making these structures can be seen in

Fig 8A.1: the small nicks in the transmission lines around each wire bond were caused

by the bonding tool itself, and resulted in numerous failures.

While the suppression of the radiated signal is still being pursued to isolate the

response of the junction, computer techniques to subtract out the feedthrough signal

are also being used. This technique has been used successfully on resonant tunneling

diodes [43].

Finally, it should be noted that the dipole radiation signal is not all bad. In

Sec. 8C an experiment which makes use of this dipole is presented.

8B Dispersion On Superconducting Transmission Lines

The coplanar structures used in the experiments of Chap. 5 were dispersive, that is, as a high speed signal propagates along the transmission line it will be stretched out in time. There are several reasons for this behavior.

First, consider the geometry of the sampler shown in Fig. 5D.2. As shown below in Fig. 8B.1, the electric field lines extend above and below the dielectric interface.
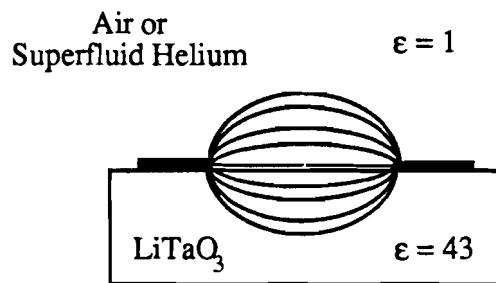
Figure 8B.1 Electric field line distribution

This results in the wave experiencing two propagation velocities, one above the interface and one below. The result is that the wave is literally dragged apart as shown in Fig. 8B.2. In that experiment the radiated waveform was sampled well away from the conducting transmission lines in a sampling configuration like that of Fig. 5D.2. The classic symptom of dispersion is shown in the figure: the rise time has become longer than the fall time. This is due to the higher frequencies being delayed relative to the lower frequencies.

In considering the effects of conducting current along the electrodes, one can first consider the two-fluid model, which allows for some current being conducted by

6.5 ps
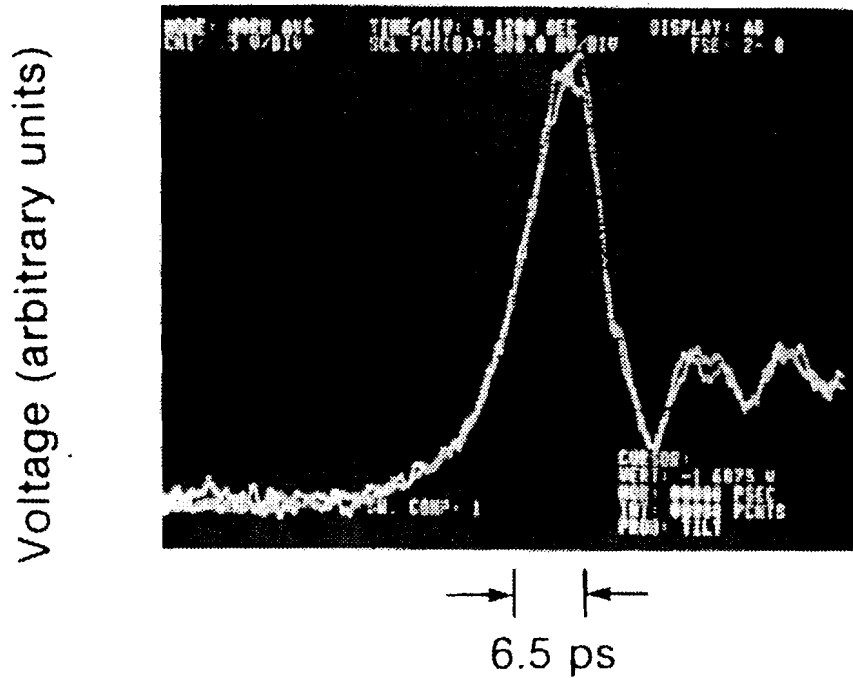
Figure 8B.2 Measurement of dispersed signal from transmission line of Fig. 8B.1

electrons in the superconducting state, and the rest in the normal state. The total current

density can be written as [8]:

$$J = J_n + J_s = (\sigma_1 + j\sigma_2)E \qquad (8B.1)$$

where E is assumed to have the form $E \exp[j\omega t]$ and

$$\sigma_1 = \frac{n_n e^2 \tau}{m(1 + \omega^2\tau^2)} \qquad (8B.2)$$

$$\sigma_2 = \frac{n_s e^2}{m\omega} + \frac{n_n e^2(\omega\tau)^2}{m\omega(1 + \omega^2\tau^2)} \qquad (8B.3)$$

It can be seen that the real part contains only the normal fluid contribution, while

the imaginary part contains both. The problem with this analysis is that it does not

consider the real conditions under which the currents actually flow. In addition, the

two-fluid model fails to predict the proper behavior at the gap frequency [44].

In a real conductor, the penetration depth into the conductor can be very small, on the order of tens of nanometers. The Mattis-Bardeen analysis takes this fact into account when calculating the conductivities [45]. Normalized to the normal electron conductivity, they are:

$$\frac{\sigma_1}{\sigma_n} = \frac{2}{\hbar\omega} \int_\Delta^\infty \left[f(E) - f(E + \hbar\omega) \right] g(E)\, dE$$

$$+ \frac{1}{\hbar\omega} \int_{\Delta - \hbar\omega}^{-\Delta} \left[1 - f(E + \hbar\omega) \right] g(E)\, d(E) \qquad (8B.4)$$

$$\frac{\sigma_2}{\sigma_n} = \frac{1}{\hbar\omega} \int_{\Delta - \hbar\omega, -\Delta}^\Delta \frac{\left[1 - 2f(E + \hbar\omega) \right]\left[E^2 + \Delta^2 + \hbar\omega E \right]}{\sqrt{\Delta^2 - E^2}\, \sqrt{(E + \hbar\omega)^2 - \Delta^2}}\, d(E) \qquad (8B.5)$$

where $f(\eta)$ is the Fermi function,

$$f(\eta) = \frac{1}{1 + \exp\left[\dfrac{\eta}{k_B T} \right]} \qquad (8B.6)$$

and

$$g(E) = \frac{E^2 + \Delta^2 + \hbar\omega E}{\sqrt{E^2 - \Delta^2}\, \sqrt{(E + \hbar\omega)^2 - \Delta^2}} \qquad (8B.7)$$

The first integral in Eq. (8B.4) represents the contribution due to the thermally excited quasiparticles and the second part accounts for the phonon-excited quasiparticles and is zero for $\hbar\omega < 2\Delta$. Equation (8B.5) is the contribution due to the paired electrons and the lower limit of the integral is $-\Delta$ if $\hbar\omega > 2\Delta$.

Next, the surface impedance of the conductor needs to be calculated [46]:

$$Z_s = \sqrt{\frac{j\omega\mu}{\sigma}} \qquad (8B.8)$$

where $\sigma = \sigma_1 - j\sigma_2$ is the form of the conductance found earlier. In general this can be converted to the form [47]:

$$Z_s(\omega) = \sqrt{\frac{j\omega\mu_0}{\sigma}} \coth\left[\sqrt{j\omega\mu_0\sigma}\ d\right] \qquad (8B.9)$$

where d is the thickness of the electrode.

Next, Eq. (8B.9) can be rewritten as the propagation constant $\gamma = \alpha + j\beta$. The real and imaginary parts of α are shown in Fig. 8B.3 for indium at a temperature of 2.18 K.

Finally, the geometrical contributions to dispersion can be found. Using a semi-empirical formula for the effective dielectric constant of a coplanar strip transmission line [47] :

$$\sqrt{\varepsilon_{eff}(f)} = \sqrt{\varepsilon_q} + \frac{\sqrt{\varepsilon_r} - \sqrt{\varepsilon_q}}{1 + aF^{-b}} \qquad (8B.10)$$

where $F = \dfrac{f}{f_{TE}}$ is the normalized frequency, $f_{TE} = \dfrac{c}{4d\sqrt{\varepsilon_r - 1}}$ is the cut-off frequency

for the lowest order TE mode, ε_q is the effective permittivity at the quasi-static limit, and a and b are geometrical constants. The effective ε is used to modify the imaginary part of the propagation constant:

$$\beta = 2\pi \frac{f}{c} \sqrt{\varepsilon_{eff}(f)} \tag{8B.11}$$

In order to follow the propagation of a signal, one can use the frequency-domain representation of an input signal and operate on it using the propagation constant:

$$E(\omega,l) = E(\omega,0) \exp\left[-\gamma l\right] \tag{8.12}$$

where $E(\omega,l)$ is the Fourier transform of the time-domain waveform.

An example of how this can be applied to the experimental situation is shown in Fig. 8B.4. The input signal was propagated along a real transmission line in the experiment, and an imaginary one in the computer. This program has been used in the past to predict propagation on microstrip transmission lines, and very good results have been obtained [49]. In this case very good agreement was achieved by merely considering the transmission line to be lossless, and only considering the dispersive effects of the transmission line structure.

Considering that the dispersive effects are the least understood (i.e. empirical), it seems that more study is needed in this area. One explanation for this behavior may be the existence of a pair-breaking lifetime that could be measured with the present arrangement using longer propagation distances, and comparing superconducting to normal propagation.

ATTENUATION DUE TO ENERGY GAP
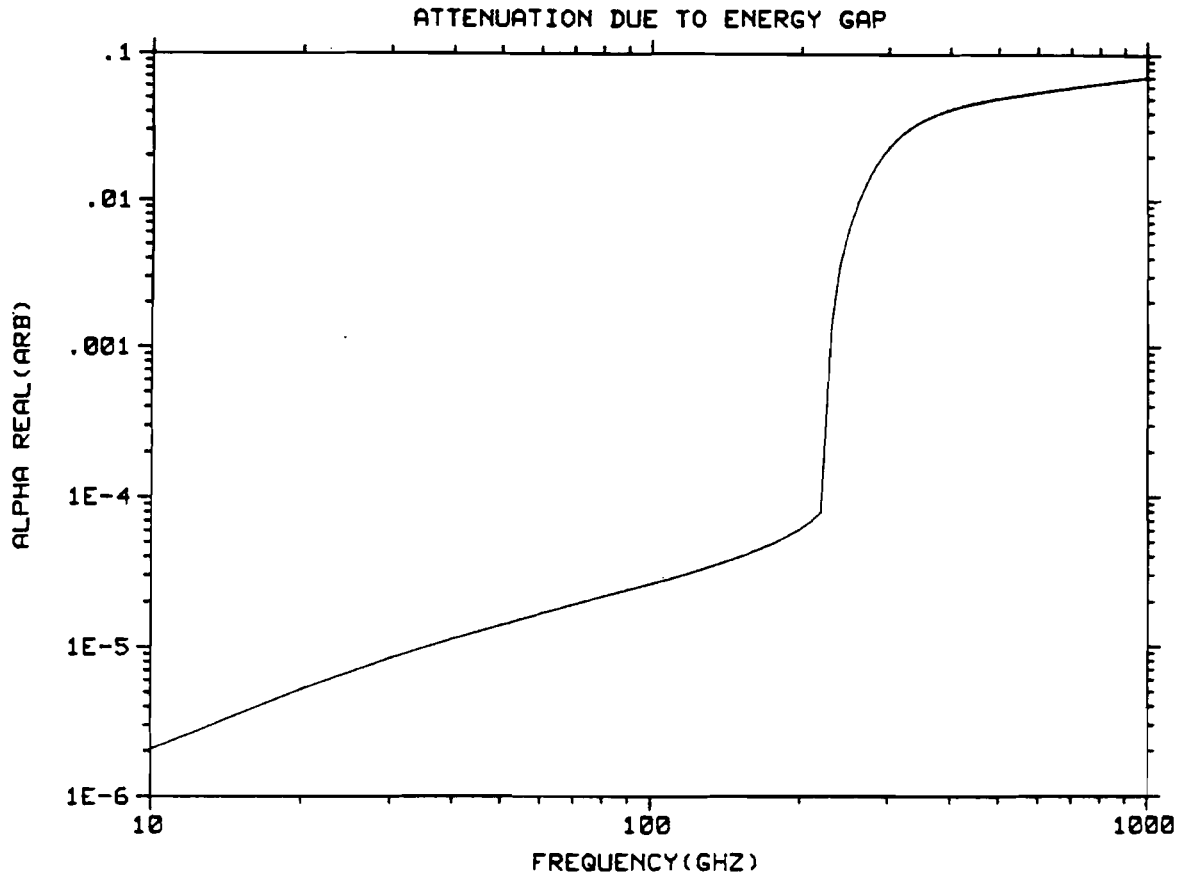
Figure 8B.3a and b. Real and imaginary parts of the attenuation constant α.

PHASE VELOCITY
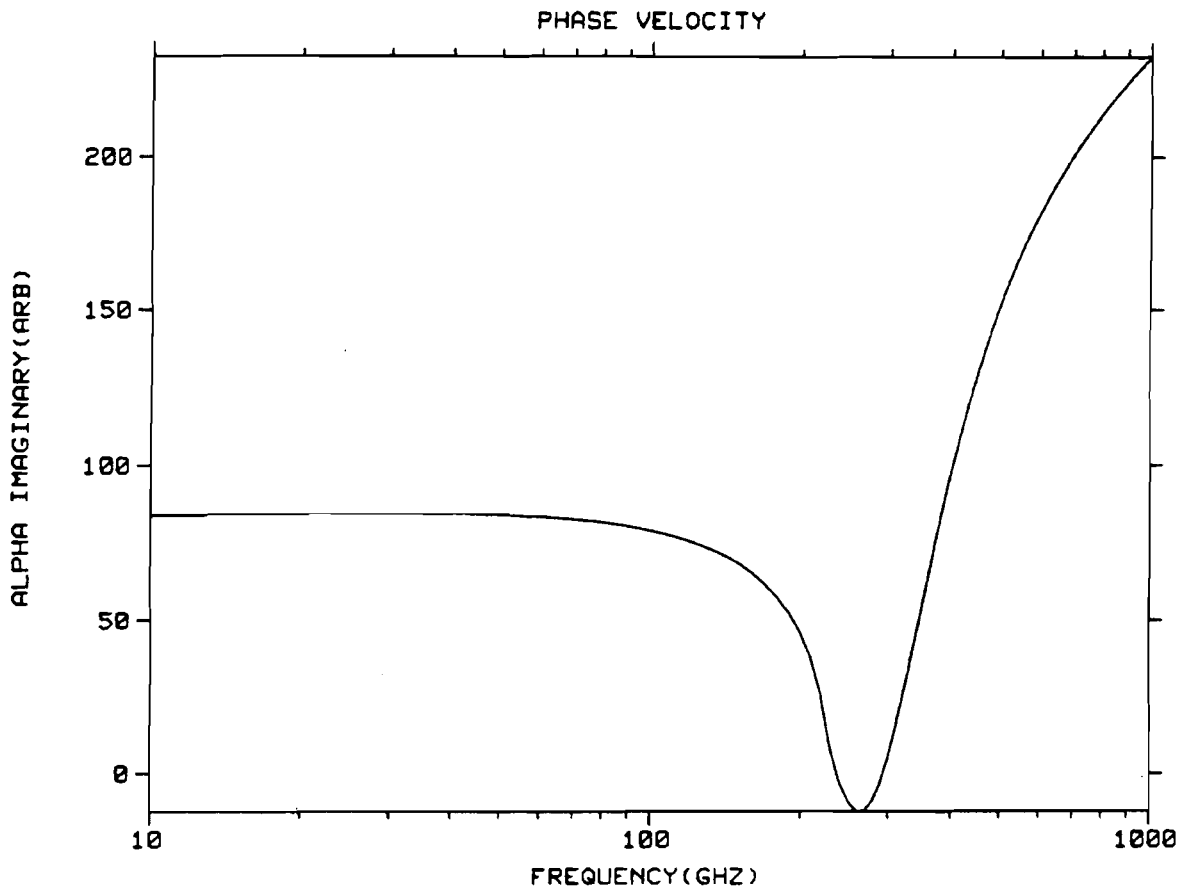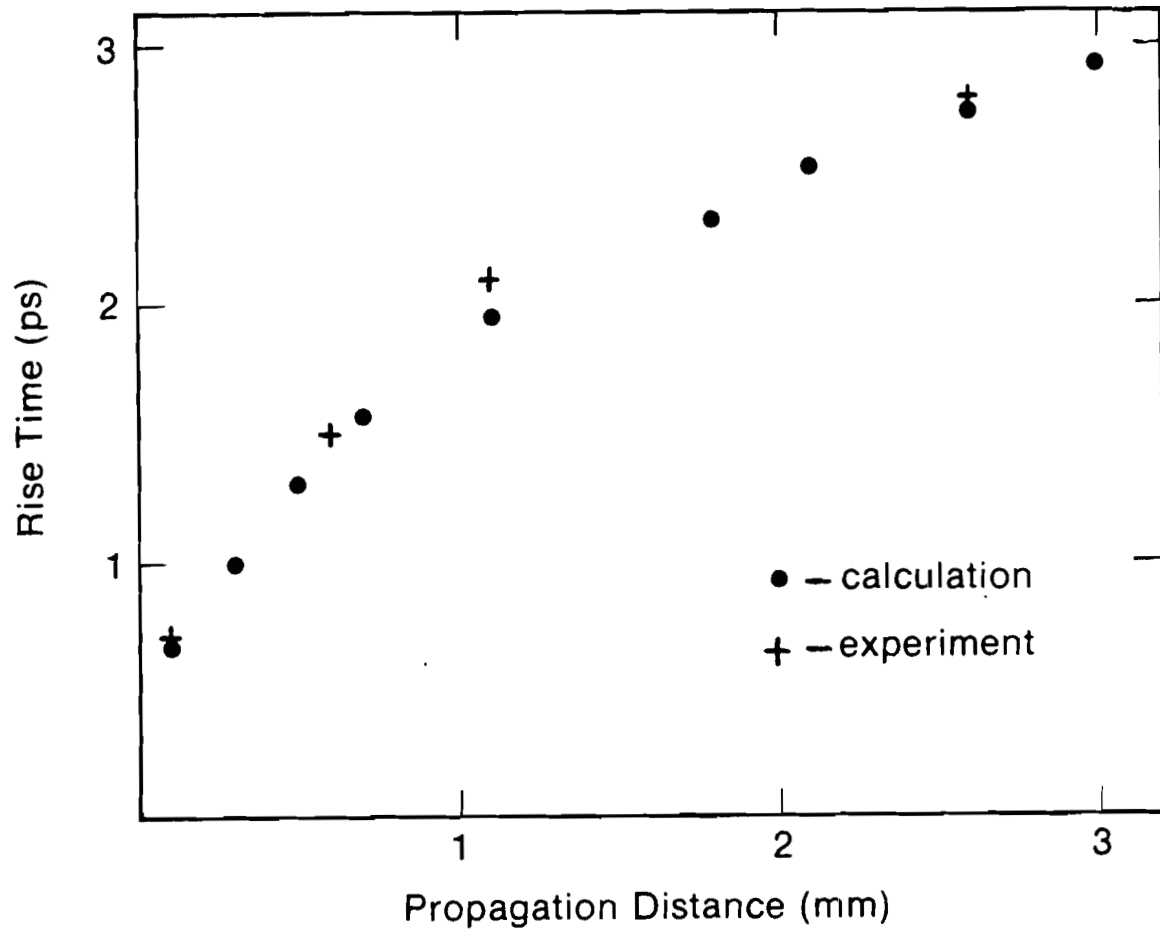
Figure 8B.4 Measured and calculated dispersion versus distance for an example coplanar strip transmission line with indium electrodes at 2.18 K.

8C Spectroscopy in Superfluid Helium

In order to further study the properties of the radiated signal, the experimental geometry of the previous section was changed in order to **maximize** the radiated signal. This was achieved using the simple geometry of Fig. 8C.1.

Superfluid Helium Bath

Sampling Beam

V^+ Excitation Beam →

Lithium Tantalate

1 mm
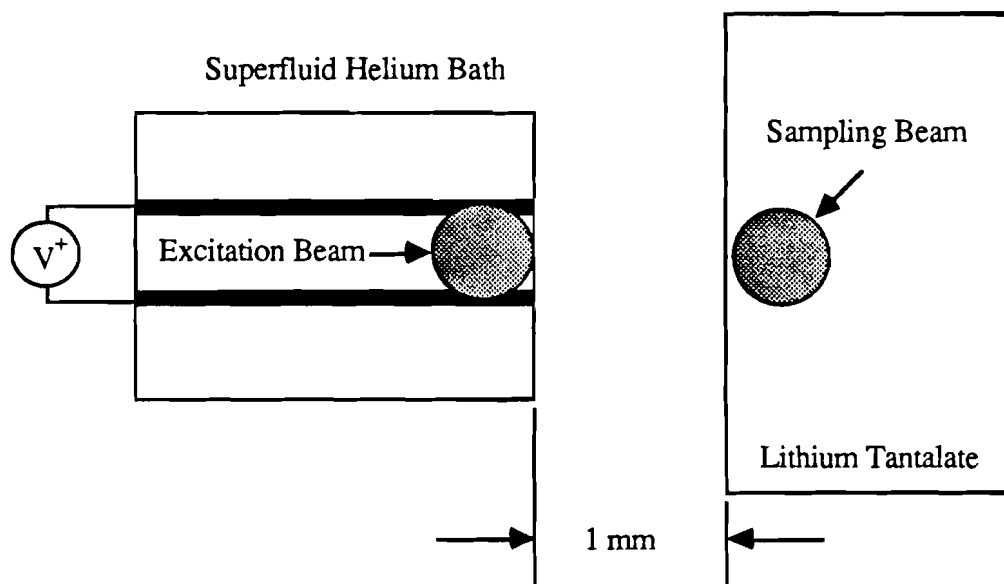
Figure 8C.1 Radiated dipole geometry.

A spacing of 1 mm was used to insure that the detection site would be in the far-field radiation regime. The expected result of this experiment would have been a short pulse, just as was seen by Downey, et al [50]. The measured result, however, was quite different. As shown in Fig. 8C.2, the rise time was more than 10 ps. When the same geometry was measured at room temperature, with gold electrodes, the rise time was on the order of 1 ps.
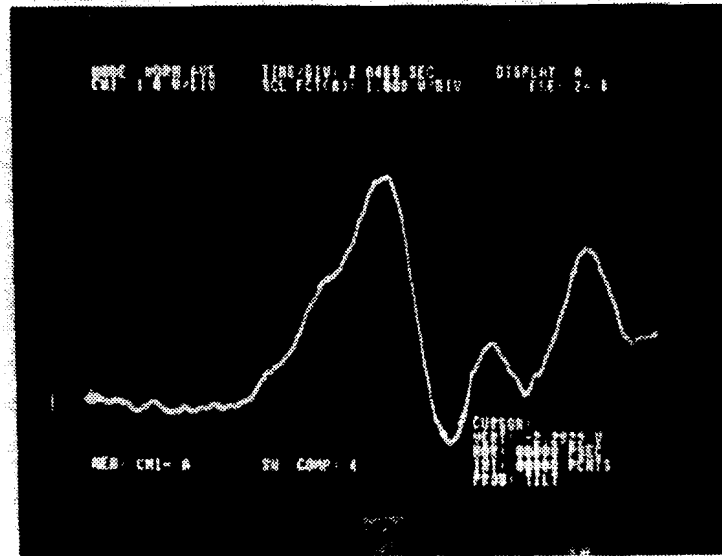
Figure 8C.2 Rise time of radiated signal

Clearly, the only major difference between the two cases was the material through which the radiated signal traveled. One possible explanation for the observed behavior is that the superfluid helium is behaving much like the superconducting indium transmission lines described in Chap. 5. Since the helium is very near the lamda point, it may be absorbing energy from the radiated signal which is above the "energy gap" of the helium. For the lambda point of helium = 2.18 K, the gap frequency is then (Ref. 8):

$$E = h\nu = 3.52 k_B T_c \qquad (8.1)$$

And $\Rightarrow \nu \approx 175$ Ghz. This compares well with the measured rise time of 20 ps.

Equation 8-1 is admittedly, derived for the case of metals, and absorption in the liquid of an electromagnetic wave raises many interesting questions, such as what are

the various lifetimes that would be associated with such a phenomenon, and what is the coupling mechanism?

An easy experiment to measure the response of the cryogen would be to substitute a dielectric such as teflon. The response of the passive dielectric could then be subtracted out to give the response of the superfluid. By performing an FFT on a computer, the frequency response could easily be found from the time-domain response of the system.

8D Infrared Sampling

Another variation of the electro-optic technique became feasible with the development of the short pulse **infrared** laser. The laser system used here is based on a Nd:YAG laser which produces 100 ps FWHM pulses. These pulses are then compressed using a standard fiber/grating pulse compressor to about 1.5 ps. The particular compressor used in this experiment consisted of a fiber some 1.4 km in length. This insured that the compression process produced very little in the way of "wings" on the pulses [51].

One advantage of the infrared wavelength is that other materials, besides lithium tantalate, may now be used. Examples of such birefringent materials are GaAs and

InP. The laser produces a wavelength of 1.06 μm, which is below the band edge for these materials. However, by frequency doubling in a second harmonic generation

(SHG) crystal, such as KTP, a frequency of 0.532 μm is produced which is above the band gap. A schematic of the laser system is shown in Fig. 8D.1

With this laser, it is then simple to construct a sampling geometry in which the GaAs substrate serves as both the photoconductive switch as well as the birefringent

Dichroic Beam Splitter

Compressor
$\approx$ 1.5 ps FWHM

Nd:YAG Laser
(100ps FWHM)

SHG
Crystal

Frequency Doubled
Pulse (Green)

Leftover
IR
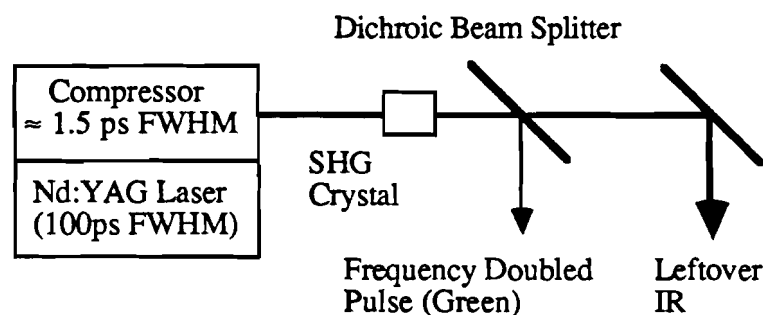
Figure 8D.1 Laser System schematic. Green pulse is used for excitation.
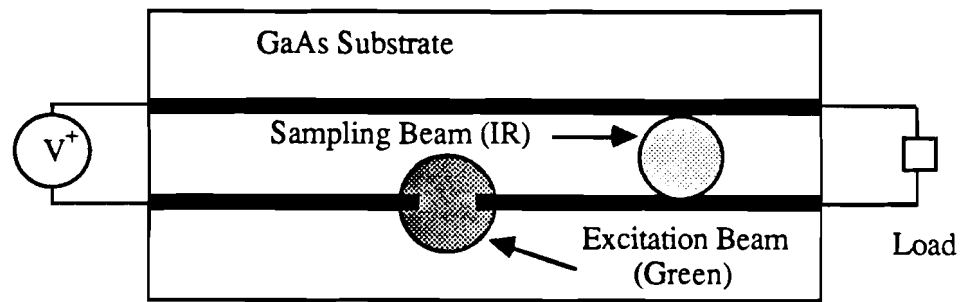
Figure 8D.2 GaAs sampler configuration

sampling crystal. As shown in Fig. 8D.2 the resulting sampler geometry is extremely simple, compared with the hybrid structures presented in Chaps. 5 and 6.

In addition, the high dielectric constant of lithium tantalate ($\varepsilon_r \approx 43$) was

replaced by the much lower value of the semiconductor ($\varepsilon_r \approx 10$). This eliminates the dielectric mismatch between the switch and sampler which was present in the hybrid structure and mitigates the effects of dispersion to some degree. Using the geometry shown, a rise time of 5 ps was obtained. Even faster optical pulse widths (≈ 500 fs FWHM) were obtained using double compression, but the SHG crystals available lacked the bandwidth for efficient doubling.

One reason for the apparent lack of speed in this implementation was the wings on the pulses mentioned above. The energy in the wings was convolved with the electrical signal along with the main part of the pulse, and contributed to the result. Even if the intensity in the wings was only 1% of the peak value, there could be as much as half of the energy in the wings as the main pulse, since the compressed pulse is ≈ 1 ps and original pulse is 100 ps long.

At present others are using this technique for sampling room temperature circuits [52], although no cryogenic application has been attempted.

8E Alternatives to Superconductivity

At the inception of the IBM Josephson computer program, the Josephson junction held the promise of unmatched switching speeds. It was assumed that the drawbacks of liquid helium cooling would be balanced by the increased speed of operation.

By the time the project ended in 1983, GaAs technology had all but caught up to Josephson technology in terms of switching speed, without the cooling requirements.

An example of such a device is the Permeable Base Transistor (PBT), which was characterized on the electro-optic sampling system in a collaboration with the device creators at the MIT Lincoln Laboratory. A description of the device and its characterization is included here to give some insight into the state of the "competition", as well as to show yet another geometry used in electro-optic sampling.

As switching speeds of conventional devices increase, new problems arise in characterizing them. It is now typical for a device to be faster than direct, conventional measurement techniques.

Some insight can still be gained from indirect measurements, however. One such technique is the ring oscillator. With this technique, 10, 20, or more devices are fabricated in a ring configuration and the entire structure is made to oscillate at its maximum frequency. The individual device response is then taken to be the period of oscillation divided by the number of devices in the ring. In general, this results in a sinusoidal output with the large number of devices tending to average out the individual device characteristics. In addition, connections between the devices start affecting the overall response. As the individual device response becomes faster, these

effects become more pronounced.

Another technique commonly employed is gain measurement in the frequency domain. Here a single device is used as an analog amplifier and the gain as a function of frequency is measured. While this measurement is useful in analog applications of transistors, the relationship between frequency response and time-domain response is not exact. Here, too, the difficulties with increasing device speed become more pronounced. Generally, measurements can be made from dc to about 26 GHz using commercial connectors. Beyond this frequency, measurements are made in narrow frequency bands, using a separate apparatus for each band. In addition, each apparatus is optimized for operation in that particular frequency band. Eventually however, the high-frequency response is linearly extrapolated from the highest measured frequencies.

Using electro-optic sampling, several new types of devices such as the two-dimensional electron gas field-effect transistor (TEGFET) and the metal semiconductor field-effect transistor (MESFET) have been characterized previously [53]. Although still tractable by the indirect techniques described above, device risetimes of 16 and 25 ps, respectively, represent switching speeds beyond the capacity of conventional direct measurement.

One new type of device, however, has proved resistant even to indirect attempts at characterization: the PBT. Conceived at MIT Lincoln Laboratory in 1979 [54], the PBT presents unique problems in its manufacture. As shown in Fig. 8E.1, a PBT is arranged similar to a vacuum-tube triode, except that here the "grid" has submicrometer dimensions. By interrupting the GaAs growth process to fabricate the grating, contaminants are introduced which keep yields low. As of this writing, only single devices have been fabricated. With only single discrete devices available, ring
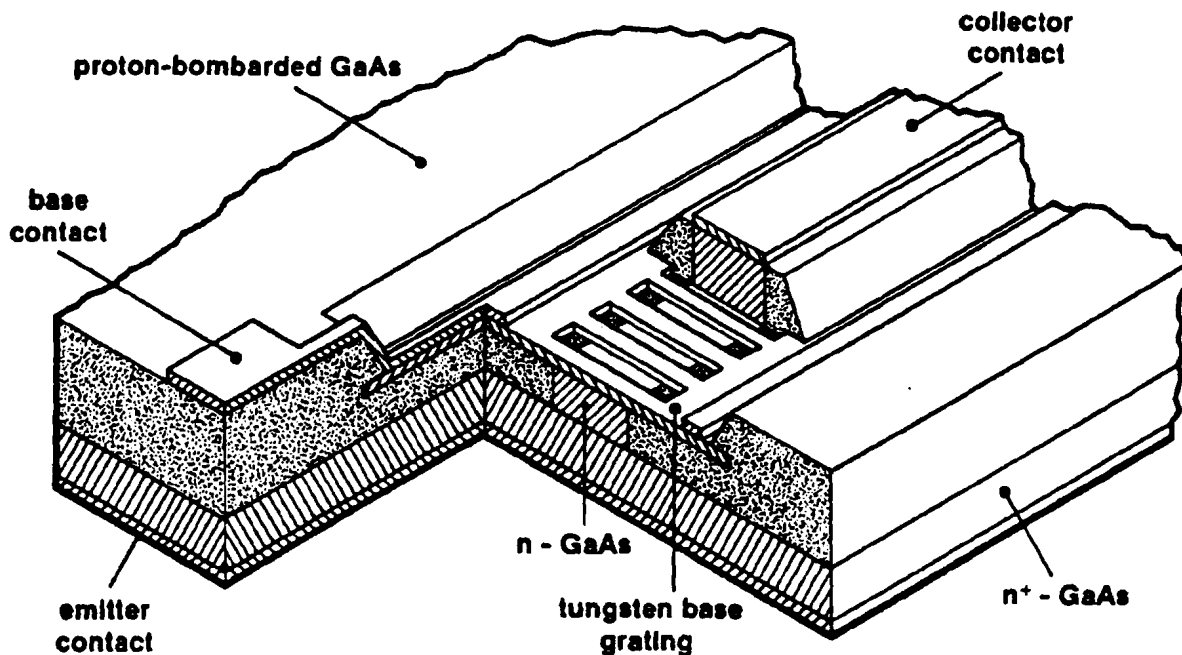
Figure 8E.1 PBT cross section

oscillators cannot be fabricated. In addition, the analog measurements have proven very difficult because of the very high gain of the PBT .The device is now known to oscillate at maximum frequencies above 200 GHz [55]. The speed of this device results from advances in fabrication techniques which allow for extremely small dimensions in both the horizontal and vertical directions. These advances have led to a device which until now remained completely uncharacterized in the time domain.

For electro-optic characterization, the PBT was built into the sampling geometry shown in Fig. 8E.2.

This geometry permits DC biasing as well as high speed operation. The CPM laser-based sampling system measured the rise time as shown in Fig. 8E.3. Electromagnetic radiation from the input connection is thought to cause the negative prepulse. This feature did not scale in amplitude with PBT gain. It was also present in
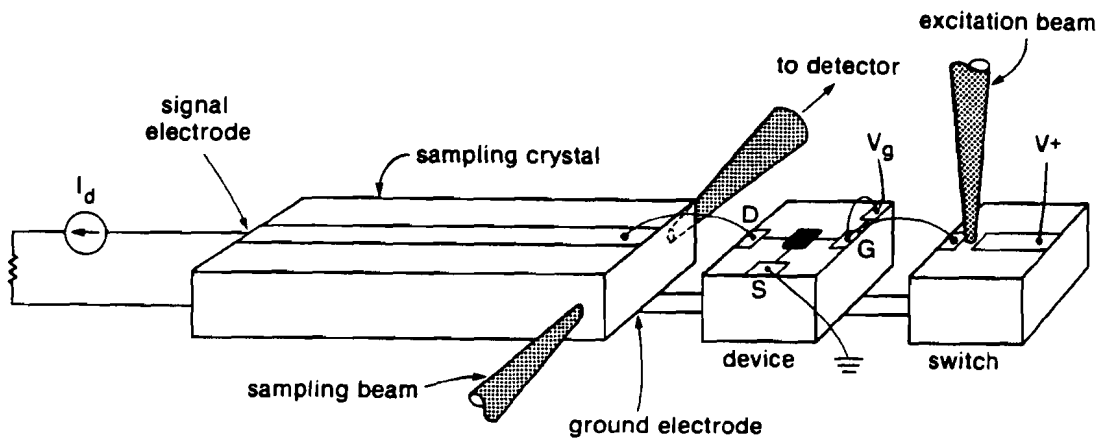
Figure 8E.2. Sampling geometry for PBT characterization. Looping wire bonds for

bias leads prevent loading of high speed signal paths.

4.75 ps/div
Rise time = 5.3 ps
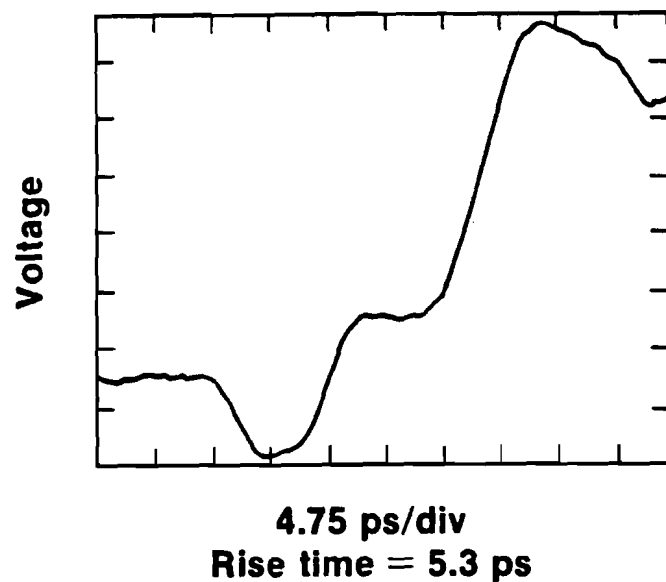
Figure 8E.3. Step response of PBT as measured by the electro-optic sampling system.

Vertical scale is in arbitrary units.

9 Conclusion

At the outset, the intent of this work was to probe the limits of performance of the Josephson tunnel junction. What was most surprising perhaps, was not that the limits were found, but that even at the limits the models still predicted the junction behavior well. Not only was the deviation from the dc behavior predicted, but the chaotic response to the periodic pulses was also predicted by the simulations.

In addition, all the technology necessary to obtain these results was developed by the author. This included the ability to perform electro-optic sampling at cryogenic temperatures, as well as new detection electronics to sense the small signal voltages produced by the junctions.

These new techniques have opened the door to a host of new areas of study, only a few of which have been touched on in the previous chapter. One important area which has not been mentioned is the combination of semiconductor devices (such as the PBT) with superconducting electrodes [56]. While these devices have yet to be demonstrated in any real way, the potential speeds of operation hold much the same promise that Josephson devices did at one time. In addition, with the development of ever higher T_C superconductors, even higher speeds may yet be realized.

10. Appendix

This section presents the program listing for the control program used in the simulations of Chap. 7. The program was written in DEC Control Language (DCL), which is a Fortran-like language with several important differences.

First, DCL allows for the Vax editor to be called under program control. This was used to make changes in the data file which was used as input to the JSPICE program.

Next, the DCL file was used to create an output file which recorded the results of the inspection of the JSPICE output file (also using the editor).

Finally it should be noted that this is a limited language, so that only integer format numbers are allowed. This was overcome by the appropriate scaling of numbers in the JSPICE data file.

```
$!************************************************************************
$!12/86                                                          TAU.COM
$!
$! THIS FILE PASSES THE VARIABLES TAU AND I_PULSE TO THE THE JSPICE
$! PROGRAM AND THEN SEARCHES THE OUTPUT FILE (DD.OUT) USING THE
$! NUMBERS_ONLY ROUTINE, THE FLAG SIGN IS USED TO INDICATE A NEGATIVE
$! VOLTAGE NEXT, IF THE JUNCTION HAS NOT SWITCHED (SIGN NOT EQUAL
$! TO "-"),  THE VALUE OF TAU IS INCREMENTED BY DELTA_TAU AND PLACED
$! INTO THE JSPICE INPUT DATA FILE, DD.DAT USING THE ROUTINE PULSE.COM
$! WHICH IN TURN USES THE FILE PULSE.SPEC AS THE NEW DATA LINE FOR
$! THE PULSE WIDTH. IF THE JUNCTION HAS SWITCHED (VOLTAGE >= 0)
$! THEN THE  VALUE OF DELTA_TAU IS HALVED AND TAU IS RESET TO ITS
$! LAST VALUE, TO "ZERO IN" ON THE CORRECT VALUE. IF THE NEW VALUE
$! OF DELTA_TAU IS LESS THAN THE SPECIFIED LIMIT, THEN THE INNER LOOP
$! (LOOP:) IS DONE. THE VALUE OF I_PULSE IS INCREMENTED, AND
$! THE PROGRAM INCREMENTS TAU (LOOP_PULSE:)
$!************************************************************************


$!******************************
$! CREATE THE OUTPUT DATA FILES
$!******************************


$ OPEN/WRITE OUTPUT TAU.OUT
$ OPEN/WRITE OUTPUT_DATA TAU.DATA
$ CLOSE OUTPUT_DATA

$!*************************************
$! WRITE VALUE OF TRANS INTO OUTPUT FILE
$!*************************************


$ OPEN/READ TIME DD.DAT
$ STEP = 0
$   START:
$   STEP = STEP + 1
$    READ TIME TRANS
$     IF STEP .LT. 15 THEN GOTO START
$         INTERVAL = F$EXTRACT(7,5,TRANS)
$         TIME_INTERVAL = F$EXTRACT(12,6,TRANS)
$    WRITE OUTPUT "**********************************************************
$    WRITE OUTPUT "TIME INTERVAL IS = ",TIME_INTERVAL
$    WRITE OUTPUT "TIME STEP IS = ",INTERVAL
$    WRITE OUTPUT "**********************************************************
$    WRITE OUTPUT ""
$ CLOSE TIME

$!******************************
$! MORE INITIAL CONDITIONS TO SET
$!******************************


$ LIMIT = 100
$ WRITE OUTPUT "LIMIT = ",LIMIT
$ I_PULSE = 2000
$ TAU = 4000
```

```
$!*****************************************************
$! INCREMENT PULSE CURRENT IN MICROAMPERES (U = E-6)
$!*****************************************************

$ LOOP_PULSE:
$ I_PULSE = I_PULSE - 100
$ IF I_PULSE .LT. 2000 THEN I_PULSE = I_PULSE + 400
$ WRITE OUTPUT ""
$ WRITE OUTPUT "*******************"
$ WRITE OUTPUT "I_PULSE = ",I_PULSE
$ WRITE OUTPUT "*F*************F*****"

$!*****************************************************
$! SET INITIAL CONDITIONS, VALUES ARE IN FEMTOSECONDS
$!*****************************************************

$ DELTA_TAU = 1500
$ MAX_TAU = 0
$ FIRST_PASS = 0
$ WRITE OUTPUT "DELTA_TAU = ",DELTA_TAU

$!*****************************************************
$! PROGRAM STARTS AT "LOOP"
$!*****************************************************

$ LOOP:
$ TAU = TAU + DELTA_TAU
$ IF ((TAU .GE. (MAX_TAU-2)) .AND. (FIRST_PASS .EQ. 1)) THEN GOTO UPDA

$!********************************************************
$! UPDATE THE VALUE OF TAU IN THE DATA FILE FOR JSPICE, DD.DAT
$!********************************************************

$ OPEN/WRITE DATA PULSE.SPEC
$ WRITE DATA "IRS 0 1 PULSE(0MA ",I_PULSE,"UA 0PS 0.1PS 0.1PS ",TAU,"FS 99US
$ CLOSE DATA
$ PURGE PULSE.SPEC

$!********************************************************
$! WRITE NEW VALUE IN DD.DAT
$!********************************************************

$        @PULSE.COM
$ PURGE DD.DAT
```

```
$!*********************************************************************
$!        RUN JSPICE
$!*********************************************************************

$         DEF/USER SYS$OUTPUT NL:
$                  JSPICE
                       DD.DAT
                       DD.OUT
$         WRITE OUTPUT ""
$         WRITE OUTPUT "  SPICE RAN, TAU = ",TAU
$         WRITE OUTPUT ""
$         PURGE DD.OUT

$!*********************************************************************,
$!        DELETE ALL TEXT IN JSPICE OUTPUT FILE (DD.OUT) INCLUDING
$!        THE FIRST VOLTAGE VALUE WHICH MAY BE NEGATIVE
$!*********************************************************************,

$ DEF/USER SYS$OUTPUT NL:
$         @NUMBERS_ONLY.COM
$                  OPEN/READ INPUT_FILE DD.OUT
$                  SIGN = "0"

$                  NEXT:
$                   READ/END_OF_FILE=MAIN_LOOP INPUT_FILE VOLTAGE
$                   SIGN = F$EXTRACT(15,1,VOLTAGE)
$                   IF SIGN .NES. "-" THEN GOTO NEXT

$         MAIN_LOOP:
$         CLOSE INPUT_FILE

$!*********************************************************************
$! EXTRACT SIGN FROM VOLTAGE VALUE, NEGATIVE SIGN IMPLIES NO SWITCHINC
$!*********************************************************************

$                  IF SIGN.EQS."-" THEN GOTO LOOP
$         UPDATE:
$                  WRITE OUTPUT "CHECKS NOT CORRECT"
$                  FIRST_PASS = 1
$                  WRITE OUTPUT "PRESENT TAU = ",TAU
$                  MAX_TAU = TAU
$                  TAU = TAU - DELTA_TAU
$                  DELTA_TAU = DELTA_TAU / 2
$                  WRITE OUTPUT "NEW DELTA_TAU = ",DELTA_TAU
$                  WRITE OUTPUT "NEW MAX_TAU = ",MAX_TAU
$                  IF DELTA_TAU .GT. LIMIT THEN GOTO LOOP

$ TAU = TAU - DELTA_TAU
$ WRITE OUTPUT ""
$ WRITE OUTPUT "*********************************** FINAL TAU = ",TAU," F
$ PURGE DD.OUT
```

```
$!**********************************************************************
$! UPDATE VALUES IN TAU.DATA FOR PLOTTING
$!**********************************************************************

$ OPEN/APPEND OUTPUT_DATA TAU.DATA
$        WRITE OUTPUT_DATA I_PULSE,"                ",TAU
$ CLOSE OUTPUT_DATA
$!**********************************************************************
$! CHECK FOR I_PULSE LESS THAN EFFECTIVE CRITCAL CURRENT
$!**********************************************************************

$ IF I_PULSE .GT. 1500 THEN GOTO LOOP_PULSE

$!**********************************************************************
$! WRAP THINGS UP:
$!**********************************************************************

$ END:
$        WRITE OUTPUT ""
$        WRITE OUTPUT ""
$        WRITE OUTPUT "POST MORTEM:"
$        WRITE OUTPUT "FINAL I_PULSE = ",I_PULSE
$        WRITE OUTPUT "FINAL TAU = ",TAU

$ CLOSE OUTPUT
$ EXIT
```

```
$!***************************************************************
$! 12/86                                          NUMBERS_ONLY.COM
$!
$! THIS ROUTINE DELETES ALL OUTPUT FROM A JSPICE OUTPUT FILE EXCEPT
$! THE CALCULATED VALUES
$!***************************************************************

$ ED/EDT DD.OUT
         DEL 1:'X'
         DEL
         DEL
         DEL 'Y':END
$ EXIT
```

```
$!***************************************************************
$! 12/8/86                                              PULSE.COM
$!
$! THIS FILE WILL SUBSTITUTE THE FILE PULSE.SPEC FOR LINE NUMBER 5
$! (INCLUDING BLANK LINES) IN THE FILE DD.DAT
$!***************************************************************

$!**************************
$! SET OUTPUT TO NULL DEVICE
$!**************************

$ DEF/USER SYS$OUTPUT NL:

$        ED/EDT DD.DAT
                INCLUDE PULSE.SPEC =TEMP
                =MAIN
                COPY 1 THRU 4 TO =TEMP
                =MAIN
                DEL 1 THRU 5
                COPY =TEMP TO =MAIN
$ EXIT
```

11 References

[1] W. Anacker, "Josephson Computer Technology: An IBM Research Project, "
IBM J. Res. Develop., Vol. 24, No. 2, 107, (1980).

[2] A. Mukherjee, "High Performance Data Processing Unit In Josephson
Technology, " Elec. Dev. Lett., Vol. 3, No. 2, 29, (1982).

[3] A.E. Siegman, Lasers, University Science Books, Mill Valley, Ca., (1986)

[4] J.A. Valdmanis, G.A. Mourou, and C.W. Gabel, Appl. Phys. Lett., Vol. 41,
No. 3, 211, (1982).

[5] K.E. Meyer, and G.A. Mourou, Appl. Phys. Lett., Vol. 45, No. 5, 492,
(1984).

[6] J.A. Valdmanis,and G.A. Mourou,"Subpicosecond Electrooptic Sampling:
Principles and Applications, " IEEE J. Quantum Electronics, QE-22, 69,
(1986).

[7] W.H. Knox, R.L. Fork, M.C. Downer, R.H. Stolen, C.V. Shank, and J.
Valdmanis, Appl. Phys. Lett., Vol. 46, 1120 (1985).

[8]   All formulae introduced in Chap. 3 are explained in full in:

T. Van Duzer, and C.W. Turner, <u>Principles of Superconductive Devices and Circuits</u>, Elsevier, New York, (1981).

see also : A. Barone, and G. Paternò, <u>Physics and Applications of the Josephson Effect</u>, John Wiley and Sons, New York, (1982).

[9]   C. Cohen-Tannoudji, B. Div, and F. Laloë, <u>Quantum Mechanics Volume II</u>, John Wiley and Sons, New York, (1977).

[10] W.A. Harrison, "Tunneling From an Independent Particle Point of View, " Phys. Rev., Vol. 123, No. 1, 85, (1961).

[11] J. Bardeen, L.N. Cooper, and J.R. Schrieffer, "Theory of Superconductivity, " Phys. Rev., Vol. 108, 1175, (1957).

[12] I. Giaever, "Tunneling Between Superconductors, " in <u>Tunneling Phenomena in Solids</u>, Plenum Press, New York, (1969).

[13] T.R. Gheewala, "Design of 2.5-Micrometer Josephson Current Injection Logic (CIL), " IBM J. Res. Develop., Vol. 24, No. 2, 130, (1980).

[14] S. Shapiro, "Josephson Currents in Superconducting Tunneling: The effect of Microwaves and Other Observations, " J. Appl. Phys., Vol. 38, 1879, (1963).

[15] W.C. Stewart, "Current Voltage Characteristics of Josephson Junctions, " App. Phys. Lett., Vol. 12, No. 8, 277, (1968).

[16] D.E. McCumber, "Effect of AC impedance on DC Voltage-Current Characteristic of Superconductor Weak Links, " J. App. Phys., Vol. 39, No. 7, 3113, (1968).

[17] S.H. Dhong, and T. Van Duzer, "Minimum Width Control-Current Pulse for Josephson Logic Gates, " IEEE Trans. Electron. Dev., Vol 27, No. 10, 1965, (1980).

[18] C.A. Hamilton, and S. Shapiro, "RF-Induced Effects in Josephson Tunnel Junctions," Phys. Rev., **B2**, 4494, (1970).

[19] J. Matisoo, Proc. Symp. Physics of Superconducting Devices, N-1, (1967).

[20] X. Meng, and W. Guo-Zhu, "Surface Observation and Failure Cause in PB and Pb-alloy Josephson Junctions, " Physica, Vol. 107B, 729, (1981).

[21] J.M. Eldridge, and D.W. Dong, "The Growth of Thin PbO Layers on Lead Films, I. Experiment, " Surface Science, Vol. 40, 512, (1973).

[22] A.C. Scott, and W.J. Johnson, "Internal Flux Motion in Large Josephson Junctions, " Appl. Phys. Lett., Vol. 14, 316, (1969).

[23] A. Johnson, and D. Auston, "Microwave Switching by Picosecond Photoconductivity," J. Quan. Elec., Vol. 11, No. 6, 283, (1975).

[24] G. Costabile, and R.D. Parmentier, "Analytic Solution for Fluxon Propagation in Josephson Junctions With Bias and Loss, " LT-14, Vol. 4, 112, (1975).

For a general review see: M. Tinkham, Introduction to Superconductivity, McGraw-Hill Inc., 161,(1975).

[25] J.A. Valdmanis, and R.L. Fork, "Design Consideration for a Femtosecond Pulse Laser Balancing Self Phase Modulation, Group Velocity Dispersion, Saturable Absorption, and Saturable Gain, " IEEE J. Quantum Electronics, Vol. QE-22, No. 1, 112, (1986).

[26] D.R. Dykaar, T.Y. Hsiang, and G.A. Mourou, "Development of a Picosecond Cryo-Sampler," Picosecond Electronics and Opto-Electronics, Springer-Verlag, 249 (1985).

[27] K.E. Meyer, and G.A. Mourou, "Two Dimensional Field Mapping With Subpicosecond Resolution, " Picosecond Electronics and Opto-Electronics, Springer-Verlag, 46 (1985).

[28] M.B. Ketchen, D. Grischkowski, C-C. Chi, I.N. Duling III, N.J. Halas, J-M, Halbout, J.A. Kash, and G.P. Li, Appl. Phys. Lett., 48, 751, (1986).

[29] C.P. Wen, "Coplanar Waveguide: A Surface Strip Transmission Line Suitable for Non-Reciprocal Device Application, " IEEE Trans. on Magn., Vol. MTT-17, 1087, (1969).

[30] C.A. Hamilton, "High-Speed, Low-Crosstalk Chip Holder for Josephson Integrated Circuits, " IEEE Trans. on Inst. and Meas., Vol. IM-31, No. 2, 129, (1982).

[31] J.H. Greiner, C.J. Kircher, S.P. Klepner, S.K. Lahiri, A.J. Warnecke, S. Basavaiah, E.T. Yen, J.M. Baker, P.R. Brosius, H.-C. Huang, M. Murakami, and I. Ames, "Fabrication Process for Josephson Integrated Circuits, " IBM J. Res. Develop., Vol. 24, No. 2, 195, (1980).

[32] A.G. Foyt, F.J. Leonberg, and R.C. Williams, SPIE, Vol. 269, 169, (1981).

[33] D.G. McDonald, R.L. Peterson, C.A. Hamilton, R.E. Harris, and R.L. Kautz, "Picosecond Applications of Josephson Junctions, " IEEE Trans. Electron Devices, Vol. ED-27, 1945, (1980).

[34] R.E. Jewett, "Josephson Junctions in SPICE 2G5, " Provided by the Electronics Research Laboratory and the Department of Electrical Engineering and Computer Sciences, University of California at Berkeley.
see also:
A. Vladimirescu, K. Zhang, A.R. Newton, D.O. Pederson and A. Sangiovanni-Vincentelli, "SPICE Version 2G User's Guide, " Ibid, (1981).

[35] R.G. Schuster, "Deterministic Chaos, An Introduction, " Physik-Verlag GmbH, Weinheim, (1984).

[36] J.P. Crutchfield, J.D. Farmer, N.H. Packard, and R.S. Shaw, "Chaos, " Scientific American, Vol. 255, No. 6, 46, (1986).

See also: C. Heimel, "A Girl's Guide to Chaos, " American Place Theater, New York, (1986).

[37] B.A. Huberman, J.P. Crutchfield and N.H. Packard, Appl. Phys. Lett. Vol. 37, 750 (1980)

[38] Y. Braiman, E. Ben-Jacob, and Y. Imry, in Squid 80, edited by H.D. Hahlbohm and H.Lübbig, De Gruyter, Berlin, 783, (1980).

[39] B.V. Chirikov, Phys. Rev. Vol. 52, 263, (1979).

[40] D.R. Dykaar, T.Y. Hsiang, and G.A. Mourou, "An Application of Picosecond Electro-Optic Sampling to Superconducting Electronics," IEEE Tran. Magn., Vol. MAG-21, 230 (1985).

[41] R.L. Kautz and R. Monaco, "Survey of Chaos in the RF-Biased Josephson Junction, " J. Appl. Phys., Vol. 57, No. 3, 875 (1985).

[42] R. Sobolewski, D.R. Dykaar, T.Y. Hsiang, and G.A. Mourou, "Picosecond Switching in Josephson Tunnel Junctions, " in <u>Picosecond Optics and Optoelectronics</u>, Lake Tahoe, Nev., Springer-Verlag, 1987, to be published.

[43] G. Mourou, "Electron Device Probing in the Femtosecond Time Scale, " Picosecond Optics and Optoelectronics, Lake Tahoe, Nev., Springer-Verlag, 1987, to be published.

[44] R.L. Kautz, "Picosecond Pulses on Superconducting Striplines, " J. Appl. Phys., Vol. 49, No. 1, 308, (1978).

[45] D.C. Mattis, and J. Bardeen, Phys. Rev., Vol. 111, 412, (1958).

[46] S. Ramo, J.R. Whinnery, and T. Van Duzer, <u>Fields and Waves in Communication Electronics</u>, John Wiley and Sons, New York, 288, (1965).

[47] R.E. Matick, <u>Transmission Lines for Digital and Communication Networks</u>, McGraw Hill, New York, Sec. 6.4, (1969).

[48] E. Yamashita, K. Atsuki, and T. Ueda, "An Approximate Dispersion Formula for Microstrip Lines for Computer Aided Design of Microwave Integrated Circuits, " IEEE Trans. Microwave Theory and Tech., Vol. MTT-27, 1036, (1979).

[49] J.F. Whitaker, T.B. Norris, G.A. Mourou, and T.Y. Hsiang, "Pulse Dispersion and Shaping in Microstrip Lines, " IEEE Trans. Microwave Theory and Tech., Vol. MTT-35, 42, (1987).

[50] P.M. Downey, and J.R. Karin, "Hertzian Dipole Measurements with InP Photoconductors, " in Picosecond Electronics and Optoelectronics, (eds) G.A. Mourou, D.M. Bloom, and C.H. Lee (Springer-Verlag, Berlin, Heidelberg, New York, and Tokyo), 201 (1985).

[51] H. Nakatsuka, D. Grischkowsky, and A.C. Balant, "Nonlinear Picosecond-Pulse Propagation Through Optical Fibers With Positive Group-Velocity Dispersion," Phys. Rev. Lett., Vol. 47, 910 (1983).

[52] B.H. Kolner, K.J. Weingarten, M.J.W. Rodwell, and D.M. Bloom, "Picosecond Sampling and Harmonic Mixing in GaAs, " in Picosecond Electronics and Optoelectronics, (eds) G.A. Mourou, D.M. Bloom, and C.H. Lee (Springer-Verlag, Berlin, Heidelberg, New York, and Tokyo), 50 (1985).

[53] K.E. Meyer, D.R. Dykaar, and G.A. Mourou, "Characterization of TEGFETs and MESFETs Using the Electrooptic Sampling Technique, " in Picosecond Electronics and Optoelectronics, (eds) G.A. Mourou, D.M. Bloom, and C.H. Lee (Springer-Verlag, Berlin, Heidelberg, New York, and Tokyo) 54 (1985).

[54] C.O. Bozler, G.D. Alley, R.A. Murphy, D.C. Flanders, and W.T. Lindley: in Proc. 7th Bien. Cornell Conf. on Active Microwave Devices, 33 (1979).

[55] M.A. Hollis, K.B. Nichols, R.A. Murphy, R.P. Gale, S. Rabe, W.J. Piacentini, C.O. Bozler, and P.M. Smith, Technical Digest IEDM, 102 (1985).

[56] M. Tonouchi, H. Sakai, T. Kobayashi, and K.Fujisawa, "A Novel Hot-Electron Transistor Employing Superconducting Base, " IEEE Tran. Magn., to be published.